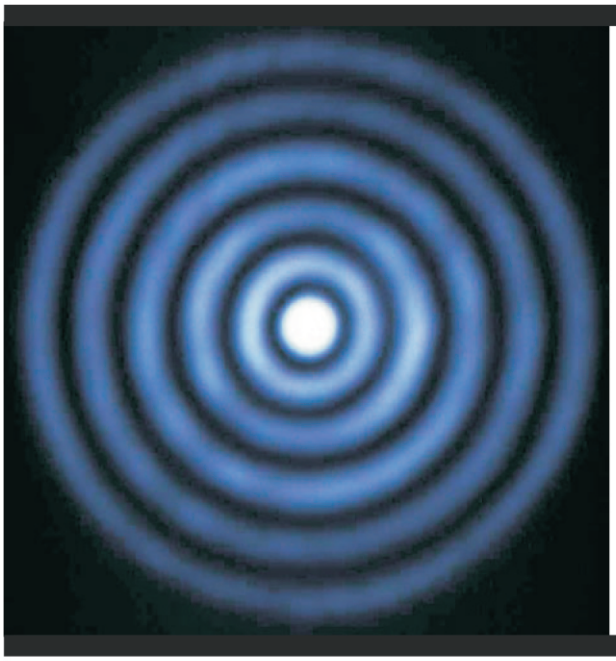

Four Wave Mixing using Intermodal Nonlinearities

Lars Søgaard Rishøj

Ph.D. Thesis

August 2012

DTU Fotonik
Department of Photonics Engineering

DTU Fotonik
Department of Photonics Engineering

Technical University
of Denmark

Four Wave Mixing using Intermodal Nonlinearities

PhD thesis

Lars Rishøj
31 August 2012

Supervisor:
Professor Karsten Rottwitt, DTU Fotonik

Abstract

The nonlinear process of four-wave mixing (FWM) enables coupling of energy between wavelengths. This is useful for both optical amplification and wavelength conversion. A crucial prerequisite for the process is phase matching. This PhD project investigates how higher order modes (HOMs) in fibers can be used as an additional degree of freedom to fulfill this phase matching requirement.

The design of a specialty few moded fiber is discussed. This fiber allows for FWM between a pump in the Ytterbium gain region with a signal at telecommunication wavelengths, hereby generating a new wavelength around 800 nm. Using pulse propagation simulations this process is investigated in details, which includes examining the impact of the overlap integrals and outer diameter (OD) variations along the fiber.

Experimentally, it is demonstrated that using a long period grating (LPG), it is possible to convert 99.8 % of the power from the fundamental mode to a specific HOM in the custom designed fiber. Furthermore, it is demonstrated that stable propagation in the considered fiber is possible, without deterioration from mode coupling.

Finally, modulation instability and multiple FWM signal and idler lines are demonstrated in the 1 μm wavelength range in the developed large mode area fiber. This is enabled by operating in the LP_{07} mode, which has anomalous dispersion despite having a mode area of 618 μm^2 at 1064 nm. In the experiments the maximum employed pump pulse energy was 105 μJ. This was restricted by the available laser since the fiber is capable of pulse energies of 540 μJ before the onset of dielectric breakdown. This represents a factor of 12 increase compared to photonic crystal fibers (PCFs) with similar anomalous dispersion characteristics. Also a peripheral result was obtained as a continuum from 680 to 1600 nm entirely in the LP_{07} mode was demonstrated.

Resumé (In Danish)

I dette Ph.D.-projekt undersøges det, hvorledes forskellige bølgetyper[1] i optiske fibre, kan udnyttes som en ekstra frihedsgrad til opfyldelse af det fasetilpasningskrav, der er en nødvendig forudsætning for firebølgeblanding. Firebølgeblanding er en ulineær proces, som muliggør udveksling af energi mellem forskellige bølgelængder, og i dette arbejde undersøges denne proces alene i optiske fibre. En sådan kobling af energi er nyttig til både forstærkning af optiske signaler og bølgelængdekonvertering.

Den nærværende afhandling beskriver udviklingen af en specifik fiber, som understøtter flere bølgetyper. Specifikt opfylder den pågældende fiber fasetilpasningskravet for firebølge-blanding mellem en pumpe, der har en bølgelængde i Ytterbiums forstærkningsregion, og et signal i telekommunikationsbåndet, når de interagerende bølgelængder befinder sig i de nødvendige bølgetyper. Herved genereres en ny bølge med en bølgelængde omkring 800 nm. Ved hjælp af simuleringer af plusudbredelsen undersøges processen i detaljer, og specielt undersøges betydningen af de forskellige overlapintegraler mellem bølgetyperne, og betydningen af fiberens diametervariationer.

Det er eksperimentelt eftervist, at man, ved hjælp af gitre, kan overføre 99,8 % af lysets effekt fra fiberens fundamentale bølgetype til en bestemt udvalgt højreordens bølgetype. Desuden demonstreres det, hvordan denne højreordens bølgetype kan udbrede sig stabilt i fiberen, så den, med andre ord, undergår en minimal ændring af lysets rummelige fordeling under udbredelsen.

Endelig påvises adskillige firebølgeblandingsprodukter i bølgelængdeområdet omkring pumpen ved 1064 nm. Firebølgeblandingen opstår i den såkaldte LP_{07}-bølgetype, som modsat fundamentalbølgetypen, udviser anormal dispersion ved 1064 nm. I eksperimenterne er den maksimalt anvendte pulsenergi 105 μJ, og det er alene begrænset af den anvendte pumpelaser, idet fiberen kan håndtere pulsenergier op til omkring 540 μJ for den anvendte pulsbredde. Denne effekt er 12 gange større end den en mikrostruktureret fiber, der har lignende dispersions egenskaber, kan tåle. Desuden er der opnået et enkelt, let perifert, resultat, eftersom et kontinuum fra 680 til 1600 nm er genereret udelukkende i LP_{07}-bølgetypen.

[1] Forskellige bølgetyper (Engelsk: modes) kendetegnes ved at hver bølgetype har sin egen unikke rummelige fordeling af lyset i fiberen.

Preface

This thesis is submitted in candidacy for the PhD degree from the Technical University of Denmark (DTU). The project has been carried out at DTU Fotonik - Department of Photonics Engineering from 2009 to 2012, with Professor Karsten Rottwitt as the main supervisor. Throughout the course of the project a total of 14-months were spent as an external stay at Boston University; the visits took place from December 2010 to August 2011, and again from January 2012 to May 2012. During this time Professor Siddharth Ramachandran was an unofficial co-supervisor of the project. Furthermore, a 1-month external stay took place at the University of Southampton where Dr. Shaiful Alam was visited in November 2011.

Acknowledgements

First of all, I would like to thank my supervisor Karsten Rottwitt for encouraging me, his always open door, and the many fruitful discussions. Secondly, I would like to thank Siddharth Ramachandran for his guidance and always being accessible for discussions, both in person and over countless email correspondences. This collaboration started in the beginning of my PhD project, during Siddharth Ramachandran´s sabbatical visit at DTU Fotonik, and continued during my later visits to his group at Boston University. Thirdly, I would like to thank Shaiful Alam for allowing me to come visit him and for the knowledge I was able to obtain during this visit. I would also like to thank the entire group of Ken Crozier at Harvard University for allowing us to use their lab facilities, more specifically their Nd:YAG pump laser.

I would also like to thank the many people who have passed through the office at DTU over the years and contributed to brighten up the days. Especially, I would like to thank Anders Pedersen, Toke Lund-Hansen, Christian Agger, Mikkel Heuck, and Henrik Steffensen.

Also I would like to thank the entire group at Boston University for their kindness and for making me feel welcome. I would like to thank Yuhao Chen for his contribution regarding the fiber design, and Michael Grogan for his aid in relation to making tapers. Furthermore, I would also like to thank Paul Steinvurzel, not so much for his patience, but more his persistency in discussions and willingness to share his impressive knowledge and experience.

Last but certainly not least, I would like to thank Martin Pedersen for his meticulous proofreading, and for posing so many intelligent questions.

Lars Søgaard Rishøj
Kongens Lyngby, August 31, 2012.

List of Publications

The work carried out during this PhD project has resulted in the following accepted publications:

- P. Steinvurzel, L. Rishøj, Y. Chen, L. Yan, J. Demas, M. Grogan, T. Ellenbogen, K. Crozier, K. Rottwitt, and S. Ramachandran, "High Energy Parametric Amplification at 1 μm with Record Large Mode Area Optical Fibers", Photonics West 2012.
- L. Rishøj, P. Steinvurzel, Y. Chen, L. Yan, J. Demas, M. Grogan, T. Ellenbogen, K. Crozier, K. Rottwitt, and S. Ramachandran, "High-Energy Four-Wave Mixing, with Large-Mode-Area Higher-Order Modes in Optical Fibres", ECOC 2012, Tu.3.F.2, Optical Society of America, 2012.
- Y. Chen, L. Yan, L. Rishøj, P. Steinvurzel, S. Ramachandran, "Dynamically Tunable Optical Bottles from an Optical Fiber," Opt. Lett., p. 3327, 2012.
- L. Rishøj, Y. Chen, P. Steinvurzel, K. Rottwitt, and S. Ramachandran, "High-Energy Fiber Lasers at Non-Traditional Colours, via Intermodal Nonlinearities," in CLEO: Science and Innovations, CTu3M.6, Optical Society of America, 2012.
- L. Rishøj and K. Rottwitt, "Excitation and Characterization of Higher Order Modes in Optical Fibers," 3rd Annual Workshop on Photonic Technologies and Applications, Berkeley, California, USA, 2012
- A. Svane, T. Lund-Hansen, L. Rishøj, and K. Rottwitt, "Wavelength Conversion by Cascaded FWM in a Fiber Optical Parametric Oscillator," in National Fiber Optic Engineers Conference, JThA014, Optical Society of America, 2011.
- L. Rishøj and K. Rottwitt, "Influence of Variations of the GVD on Wavelength Conversion at Second Gain Region of a Parametric Process," in OSA Topical Meeting "Nonlinear Photonics", NTuC11, Optical Society of America, 2010.

- T. Lund-Hansen, K. Rottwitt, C. Peucheret. Z. Lali-Dastjerdi, L. Rishøj, A. Svane, L. Andersen, and V. Cristofori, "Pump to Signal Noise Transfer in Parametric Fiber Amplifiers," Photonics 2010, Guwahati, India, 2010.
- K. Rottwitt, A. C. Brunetti, J. Lægsgaard, J. Weirich, L. Rishøj, X. Liu, L. Scolari, M. Pedersen, A. Pedersen, H. Steffensen, and L. Wei, Enhancing the Capacity of Light. Chapter in Beyond Optical Horizons - Today and Tomorrow with Photonics, 75-87 (2009)

Contents

1

Introduction

1.1 Background and Motivation

Over half a century has passed, since Theodore Maiman in 1960 for the first time demonstrated the concept of lasing in a ruby crystal [1]. Shortly after, the first gas laser was demonstrated by Ali Javan [2], and in 1962 the first semiconductor laser followed [3]. Since then the laser has defined and revolutionized numerous scientific fields.

After the development of the optical fiber, the invention of the first fiber laser by Elias Snitzer soon followed [4,5]. One of the most important advantages with fiber lasers is that free space elements are not required. This means that fiber lasers are alignment free, thus they are very robust, and consequently cheaper to maintain. A common method used in fiber lasers is to dope the fiber with rare earth elements, e.g. ytterbium, erbium, and thulium [6]. This has the limitation that it restricts the possible wavelengths of lasing to certain bandwidth regions. A solution could be to subsequently convert the light using the nonlinear process of Raman scattering. However, due to the fundamental nature of the process, it is only possible to shift towards longer wavelengths [7].

In order to develop fiber lasers operating at wavelengths shorter than 1 μm, which for instance, is desirable for several biological applications; one approach is to use parametric processes, such as third harmonic generation (THG) or four-wave mixing (FWM). The challenge with this approach is that momentum conservation is required. In the case where high powers and short wavelengths are the targets, it is beneficial to use an ytterbium doped fiber laser as the pump source, since this provides high power at a shorter wavelength compared to erbium and thulium doped fiber lasers. The requirement for momentum conservation often leads to the need for a fiber with anomalous dispersion at 1 μm. This could be obtained using photonic crystal fibers (PCFs), however this inherently leads to small effective area of the mode, and thus high power restrictions [8]. An alternative approach is to use higher order modes (HOMs). Besides from the advantage of using large area modes, there is furthermore the

opportunity to fulfill the momentum conservation criteria by selecting different modes accordingly, thereby opening up a new degree of freedom. Using HOMs in fibers to create momentum conservation is an analogy to changing the angle of the incident beam through a nonlinear crystal. The approach of using HOMs in few-moded fibers has become relevant over the last few years, due to refined fabrication techniques. This new class of specialty fibers intentionally guides and ensures stable propagation of HOMs, thereby a high degree of control is possible [9, 10]. As opposed to earlier work by Roger Stolen, where traditional multi-mode fibers were used, which guide numerous modes simultaneously in an arbitrary manner [11–13].

The interest in HOM fibers is also present from the optical communication community [14–16]. The ever increasing demand for higher bandwidth in communication systems has in the past lead to the development of wavelength division multiplexing (WDM) systems. Similarly, the bandwidth demand has recently created a push towards utilizing fibers that support several modes, since each mode could for a given wavelength represent an additional communication channel. One of the advantages of having several channels in a single fiber is that amplification of multiple channels is possible with a single amplifier. Interest has also arisen in the community of bio-photonics. This is due to the propagation properties obtained with HOMs, which include divergence resistant beams, self-healing properties, and creation of dark foci [17]. These effects have been demonstrated experimentally during this PhD project and lead to the following publications [18, 19]. However, this topic is considered peripheral, hence the work is not included in this thesis. Besides from the ability to create these phenomena, there is also the added advantage of remote fiber delivery.

1.2 Thesis Content

The overall focus of this PhD project is on utilizing HOMs in a controlled manner to obtain momentum conservation for FWM processes, thus demonstrating this new platform for nonlinear mixing processes. FWM involves two pump waves, which interact with a signal seed and generate a fourth wave called the idler. A schematic of the process is illustrated in Fig. 1.1.

The long term goal this project has been working toward is to develop a tunable all fiber laser around 800 nm. This is realized by using a high powered ytterbium doped fiber laser around 1045 nm along with a tunable signal seed at telecommunication wavelength around 1500 nm. The first milestone in the project was to develop a new fiber design, which ensures intermodal phase matching over tens of nanometers around 800 nm. The outcome of this project could potentially be the first demonstration of an all fiber version of the Ti:sapphire laser, which is still a workhorse in many laboratories for this specific wavelength range. A second milestone during the project has been to develop and build a tunable fiber pump laser. This was carried out in collaboration

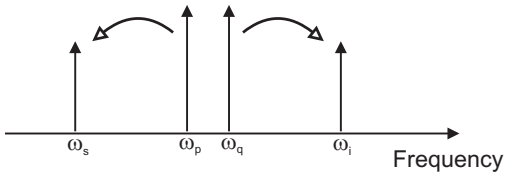

Figure 1.1: A schematic of two pumps at frequencies ω_p and ω_q that couple energy to the signal at ω_s, and idler at ω_i, provided that energy and momentum conservation are fulfilled.

with the Optoelectronic Research Centre at the University of Southampton. The laser was not completed within the timeline of this project, due to unforeseen challenges and delayed delivery times for components. Since the laser was never used in any experiments, a detailed description and characterization of the laser has been omitted from this thesis. However, specifications of the laser are of importance for the fiber design and underlie a considerable part of the simulations, therefore a brief summary of the concept and specifications are mentioned in App. A.

Instead of the custom built fiber pump laser, a Minilite Nd:YAG laser from Continuum was utilized, which lead to several changes in the project. To successfully perform the experiments regarding development of a fiber laser around 800 nm, it is important that the pump source is tunable. Since this is not the case for the Nd:YAG laser it was not feasible to attempt this final experiment within the timeline of this PhD project. However, the final experiment has been treated numerically, and the results are presented and discussed in this thesis.

Due to the change of the pump source the experimental work was focused on more fundamental experiments than the 800 nm experiments, thus acting more as a proof of principle. This involves demonstrating modulation instability (MI) in the 1 μm pump regime using HOMs, and creating FWM gain over tens of nanometers on either side of the pump. The next experimental steps involve slightly more elaborated mode combination schemes. Unfortunately it was not possible to address this within the timeline of the thesis, partly due to an unexpected additional 6 months fabrication time for the customized fiber. However, all HOM FWM experimental work was performed using the customized fiber. The knowledge obtained regarding mode excitation, and in this relation mode stripping, is relevant for future experiments aiming for the ultimate goal of developing the 800 nm tunable fiber laser.

1.3 Thesis Structure

The chapters in this thesis are organized as follows.

Chapter 2 - **Theory** briefly describes the theory utilized in this thesis with the main focus on the assumptions in the derivation of the governing propagation equations. In the first section the general case of FWM involving HOMs is introduced, which includes a discussion of phase matching criteria. In the second section, HOMs are discussed with focus on stability of propagation in fibers. Lastly, the basic concepts of mode coupling theory are summarized and the important equations for long period gratings (LPGs) are presented.

Chapter 3 - **Higher Order Mode Fibers** describes the double cladding fibers, which were designed for the HOM mixing experiments. After the important design criteria of the fiber is mentioned, the final design is presented with a discussion of each of the different parameters. Finally, measurements of the index profile of both the preform and drawn fiber are shown.

Chapter 4 - **Mode Conversion** presents different methods for obtaining mode conversion. In the following, the fabrication process and characterization method of the mode converters used in this project are presented. Then the mode converters fabricated in the custom designed fiber are shown, which includes a description of the mode stripping methods that were needed for this specific fiber. Finally, a discussion of broad bandwidth mode converters is included.

Chapter 5 - **Simulations for Higher Order Mode Four Wave Mixing** presents numerical simulations for two different mode combinations schemes, which both enable wavelength conversion between a pump in the ytterbium gain region and a seed signal at telecommunication wavelengths, to generate new wavelengths around 800 nm. The impact of pulse shape, self phase modulation (SPM) of the pump in the fundamental mode before the mode converter, and the overlap integrals are discussed. In the following section, dielectric breakdown is discussed along with the possibility of energy scalability when using HOMs. Finally, the impact of outer diameter (OD) fluctuations along the fiber is addressed.

Chapter 6 - **Experiments for Higher Order Mode Four Wave Mixing**. In this chapter the experimental setup is briefly explained along with a discussion of different aspects related to the equipment, which are found to have relevance for the experiments. In the remaining part of the chapter the different HOM FWM experiments are presented.

The following two chapters of this thesis are devoted to a summary of the most important conclusions, and an outlook with recommendations for possible continuations of the project.

Numerous acronyms are used in this thesis, therefore a list of acronyms is provided in App. F. The acronyms are defined the first time they are used in each chapter.

2

Theory

In this chapter the theory utilized in this thesis is briefly described with the main focus on the assumptions and the final governing equations. In the first section the general case of four-wave mixing (FWM) involving higher order modes (HOMs) is introduced; this includes a discussion of phase matching criteria. Secondly, HOMs are discussed, which includes a presentation of the modesolver used. The final section is where the basic concepts of mode coupling theory are summarized and important equations are mentioned.

2.1 Theory for Higher Order Modes Four Wave Mixing

2.1.1 Dual Pump Scheme

In this section the governing equations are discussed. These equations describe pulse propagation in a fiber under the influence of the third-order parametric processes; caused by the third-order susceptibility, $\chi^{(3)}$. In the general case FWM involves the interaction between four optical waves at different wavelengths. The energy of the pumps at ω_p and ω_q are then transferred back and fourth to both the signal at ω_s and the idler at ω_i. From energy conservation it is given that $\omega_p + \omega_q = \omega_s + \omega_i$.

The derivation starts from the well known Maxwell equations, given by [7]

$$\nabla \times \mathbf{E} = -\frac{\partial \mathbf{B}}{\partial t} \tag{2.1.1a}$$

$$\nabla \times \mathbf{H} = \mathbf{J} + \frac{\partial \mathbf{D}}{\partial t} \tag{2.1.1b}$$

$$\nabla \cdot \mathbf{D} = \rho_f \tag{2.1.1c}$$

$$\nabla \cdot \mathbf{B} = 0. \tag{2.1.1d}$$

Here $\mathbf{E}$ and $\mathbf{B}$ are the electric and magnetic field vectors, respectively, and $\mathbf{D}$ and $\mathbf{H}$ are the electric displacement field and magnetic flux density, respectively. In silica there are no free charges, therefore the current density vector and charge density are zero, hence $\mathbf{J} = 0$ and $\rho_f = 0$. From Maxwell´s equations it is then possible to derive the wave equation given by

$$\nabla^2\mathbf{E} - \frac{1}{c^2}\frac{\partial^2\mathbf{E}}{\partial t^2} = \mu_0\frac{\partial^2\mathbf{P}_L}{\partial t^2} + \mu_0\frac{\partial^2\mathbf{P}_{NL}}{\partial t^2}, \tag{2.1.2}$$

where $\mathbf{P}_L$ is the linear polarization, and $\mathbf{P}_{NL}$ is the nonlinear polarization. Silica exhibits inversion symmetry, thus the second order susceptibility, $\chi^{(2)}$, is neglectable. Furthermore, it is assumed that the nonlinear contribution only stems from the third-order susceptibility and that the nonlinear response is instantaneous, therefore

$$\mathbf{P}_L = \epsilon_0\chi^{(1)} \cdot \mathbf{E} \tag{2.1.3a}$$

$$\mathbf{P}_{NL} = \epsilon_0\chi^{(3)}\vdots\mathbf{EEE}. \tag{2.1.3b}$$

The field is assumed to consist of a sum of four optical waves. In order to simplify the theory, the scalar case is considered. This means that all waves are polarized in the transverse x-direction, and the polarization is maintained during propagation through the fiber. This assumption is verified since only linearly polarized modes are observed in the experiments and the high pump power ensures short fiber lengths, therefore making it possible for the interacting fields to remain co-polarized through the entire fiber. In mathematical terms the field is expressed as

$$\mathbf{E} = \frac{1}{2}\hat{x}\sum_{n=s,p,q,i} E_n(x,y,z,t)\exp\left[i\left(\beta_n z - \omega_n t\right)\right] + c.c. \tag{2.1.4}$$

Here $\hat{x}$ is the unit vector in the transverse x-direction and z is the axis of propagation, β_n is the propagation constant for a given mode and frequency. The angular frequency is given by ω_n, while c.c. is the complex conjugate.

Next we express $\mathbf{P}_L$ and $\mathbf{P}_{NL}$ on the same form

$$\mathbf{P}_L = \frac{1}{2}\hat{x}\sum_{n=s,p,q,i} P_{L,n}\exp\left[i\left(\beta_n z - \omega_n t\right)\right] + c.c. \tag{2.1.5a}$$

$$\mathbf{P}_{NL} = \frac{1}{2}\hat{x}\sum_{n=s,p,q,i} P_{NL,n}\exp\left[i\left(\beta_n z - \omega_n t\right)\right] + c.c., \tag{2.1.5b}$$

where $P_{L,n}$ and $P_{NL,n}$ are collections of terms that are to be determined below. By inserting Eq. (2.1.4) and Eq. (2.1.5) into Eq. (2.1.2), it is possible to derive four coupled nonlinear equations, one for each wave denoted by p, q, s, and i. Due to the time derivatives, it is more convenient to shift Eq. (2.1.2) into the

Fourier domain. This leads to the following equations, which is on the form of a Helmholtz equation

$$\nabla^2 \tilde{E}_n + \epsilon_n(\omega) k_n^2 \tilde{E}_n = 0, \tag{2.1.6}$$

where $k_n = \omega_n/c$ and the dielectric function is given by $\epsilon_n(\omega) = 1 + \tilde{\chi}^{(1)}_{xx} + \epsilon_{\mathrm{NL}}$, where ϵ_{NL} represents the nonlinear contributions. Furthermore, since the fiber is invariant along propagation, it is assumed that $E_n(x, y, z, t) = F_n(x, y)A_n(z, t)$, where $F_n(x, y)$ is the transverse distribution of the fiber modes, and $A_n(z, t)$ is the longitudinal field envelopes of the pulses. Then by the method of separation of variables it is possible to divide the equation into a transverse problem for the modal distribution, and a set of four coupled equations for the envelopes. The transverse problem is addressed in Sec. 2.2.1.

It is assumed that the nonlinear contributions to the dielectric constants are small, and even though they have a time dependence, it is by use of the slowly varying envelope approximation (SVEA) possible to consider the nonlinear contribution as being constant when performing the Fourier transformations. Using SVEA it is furthermore assumed that the second order derivative terms, such as $\partial^2 \tilde{A}_n/\partial z^2$, can be neglected. The nonlinear terms give rise to a modification of the refractive index and the absorption coefficient. Since the two photon absorption coefficient is very small for silica fibers in the wavelength region of interest, it is neglected in the following [7].

The four equations for the pulse envelopes are then transformed back into the time domain, which gives

$$\begin{aligned}\frac{\partial A_p}{\partial z} &= i \sum_{m\geq 1} \frac{i^m \beta_{m,p}}{m!} \frac{\partial^m A_p}{\partial t^m} - \frac{\alpha_p}{2} A_p \\ &+ \frac{i n_2 \omega_p}{c} \left[\left(f_{pp}|A_p|^2 + 2 \sum_{k=q,s,i} f_{kp}|A_k|^2 \right) A_p + 2 f_{pqsi} A_s A_i A_q^* \exp\left(i\Delta\beta z\right) \right]\end{aligned} \tag{2.1.7a}$$

$$\begin{aligned}\frac{\partial A_q}{\partial z} &= i \sum_{m\geq 1} \frac{i^m \beta_{m,q}}{m!} \frac{\partial^m A_q}{\partial t^m} - \frac{\alpha_q}{2} A_q \\ &+ \frac{i n_2 \omega_q}{c} \left[\left(f_{qq}|A_q|^2 + 2 \sum_{k=p,s,i} f_{kq}|A_k|^2 \right) A_q + 2 f_{pqsi} A_s A_i A_p^* \exp\left(i\Delta\beta z\right) \right]\end{aligned} \tag{2.1.7b}$$

$$\frac{\partial A_s}{\partial z} = i \sum_{m\geq 1} \frac{i^m \beta_{m,s}}{m!} \frac{\partial^m A_s}{\partial t^m} - \frac{\alpha_s}{2} A_s$$
$$+ \frac{i n_2 \omega_s}{c} \left[\left(f_{ss} |A_s|^2 + 2 \sum_{k=p,q,i} f_{ks} |A_k|^2 \right) A_s + 2 f_{pqsi} A_p A_q A_i^* \exp\left(-i \Delta\beta z\right) \right] \tag{2.1.7c}$$

$$\frac{\partial A_i}{\partial z} = i \sum_{m\geq 1} \frac{i^m \beta_{m,i}}{m!} \frac{\partial^m A_i}{\partial t^m} - \frac{\alpha_i}{2} A_i$$
$$+ \frac{i n_2 \omega_i}{c} \left[\left(f_{ii} |A_i|^2 + 2 \sum_{k=p,q,s} f_{ki} |A_k|^2 \right) A_i + 2 f_{pqsi} A_p A_q A_s^* \exp\left(-i \Delta\beta z\right) \right], \tag{2.1.7d}$$

where the asterisk denotes the complex conjugated. The wavelength dependent loss coefficient is defined by $\alpha_n = \alpha(\omega_n)$. Also the nonlinear index, n_2, is assumed to be independent of the wavelength [20]. Instead of using an exact functional expression for the propagation constants, $\beta_n(\omega_n)$, it is described using Taylor expansions around the carrier frequencies in each of the four equations. The Taylor expansion and the coefficients are given by

$$\beta_n(\omega) = \sum_{m=1}^{\infty} \frac{\beta_{m,n}}{m!} (\omega - \omega_n)^m \qquad n = s, p, q, i, \tag{2.1.8}$$

$$\beta_{m,n} = \left(\frac{d^m \beta_n(\omega)}{d\omega^m} \right)_{\omega=\omega_n} \qquad n = s, p, q, i. \tag{2.1.9}$$

This has the advantage of possible decoupling of the dispersion effects. The overlap integrals are given by

$$f_{ijkl} = \frac{\left\langle F_i^* F_j^* F_k F_j \right\rangle}{\left[\left\langle |F_i|^2 \right\rangle \left\langle |F_j|^2 \right\rangle \left\langle |F_k|^2 \right\rangle \left\langle |F_l|^2 \right\rangle \right]^{\frac{1}{2}}}, \tag{2.1.10}$$

where F_n is the spatial distribution of the fiber modes, the angled brackets is shortened notation for integration over the transverse cross section. Also by definition, $f_{ij} = f_{iijj}$, where $i, j, k, l = p, q, s, i$. This overlap integral has proven to be a great description for the fundamental mode, however it has also been shown experimentally to be an excellent approximation for self phase modulation (SPM) in HOMs [21]. The phase mismatch is given by

$$\Delta\beta = \beta_s + \beta_i - \beta_p - \beta_q. \tag{2.1.11}$$

The concept of phase matching is discussed in details in Sec. 2.1.3.

In this derivation stimulated Brillouin scattering (SBS) is ignored, which is a reasonable assumption for pulse widths smaller than a few ns [22]. Furthermore, since intra pulse Raman amplification is also neglected, this means that the equations are only valid for pulse widths wider than 1 ps [7]. The terms for stimulated Raman scattering (SRS) between the four wavelengths are included when the frequency detuning between the field components are within the Raman gain bandwidth. In the general case, let us assume that $\lambda_a > \lambda_b$, hence the terms become

$$\frac{\partial A_a}{\partial z} = ... + \frac{n_2 \omega_a f_{aabb}}{c} f_R \mathrm{Im}\left[\tilde{\mathrm{h}}_{\mathrm{R}}\left(\Omega_{\mathrm{ab}}\right)\right] \tag{2.1.12}$$

$$\frac{\partial A_b}{\partial z} = ... - \frac{n_2 \omega_b f_{aabb}}{c} f_R \mathrm{Im}\left[\tilde{\mathrm{h}}_{\mathrm{R}}\left(\Omega_{\mathrm{ab}}\right)\right]. \tag{2.1.13}$$

Here, f_R is the fractional Raman contribution, $\mathrm{Im}\left[\tilde{\mathrm{h}}_{\mathrm{R}}\right]$ is the imaginary part of the Fourier transform of the Raman response function, and Ω_{ab} is the frequency difference, thus in this case $\Omega_{ab} = \omega_b - \omega_a$.

In Eq. (2.1.7) the terms in all four equations are organized in the same order. The first sum accounts for all dispersion terms: here the first term of the sum is related to the group velocity, the second term of the sum is the dispersion parameter, and so on. The second terms in the equations are responsible for losses during propagation. The third terms are known as self phase modulation (SPM) and the fourth terms are the sums of the cross phase modulation (XPM) terms. The last term governs the energy exchange between the pumps and the signal and idler, where $\Delta\beta$ is given by Eq. (2.1.11). The exchange of power depends both on phase matching conditions and the temporal overlap between the pulses.

In relation to the numerical implementation, if the frequency spacing between the four carrier frequencies is small compared to the frequency windows defined around each carrier frequency, then it is possible to reduce the computational time by using a different approach; typically the frequency spacing must be less than a few THz [7]. Instead of solving the four coupled equations, an initial amplitude of the following form is inserted into the nonlinear Schrödinger equation

$$A(0,t) = \sum_{n=p,q,s,i} A_n(0,t) \exp\left[-i(\omega_n - \omega_r)t\right], \tag{2.1.14}$$

where ω_r is the reference frequency.

2.1.2 Degenerate Pump Scheme

In FWM a special case exists where the pump is wavelength degenerate, meaning that the energy conservation is given by $2\omega_p = \omega_s + \omega_i$. The derivation method is similar to that in Sec. 2.1.1, however in this case, the electric field

is only given by a sum of three waves

$$\mathbf{E} = \frac{1}{2}\hat{x} \sum_{n=s,p,i} E_n(x,y,z,t) \exp\left[i\left(\beta_n z - \omega_n t\right)\right] + c.c. \tag{2.1.15}$$

The three coupled equations become

$$\frac{\partial A_p}{\partial z} = i \sum_{m\geq 1} \frac{i^m \beta_{m,p}}{m!} \frac{\partial^m A_p}{\partial t^m} - \frac{\alpha_p}{2} A_p + \frac{i n_2 \omega_p}{c} \left[\left(f_{pp}|A_p|^2 + 2 \sum_{k=s,i} f_{kp}|A_k|^2 \right) A_p + 2 f_{ppsi} A_s A_i A_p^* \exp\left(i\Delta\beta z\right) \right] \tag{2.1.16a}$$

$$\frac{\partial A_s}{\partial z} = i \sum_{m\geq 1} \frac{i^m \beta_{m,s}}{m!} \frac{\partial^m A_s}{\partial t^m} - \frac{\alpha_s}{2} A_s + \frac{i n_2 \omega_s}{c} \left[\left(f_{ss}|A_s|^2 + 2 \sum_{k=p,i} f_{ks}|A_k|^2 \right) A_s + f_{ppsi} A_p^2 A_i^* \exp\left(-i\Delta\beta z\right) \right] \tag{2.1.16b}$$

$$\frac{\partial A_i}{\partial z} = i \sum_{m\geq 1} \frac{i^m \beta_{m,i}}{m!} \frac{\partial^m A_i}{\partial t^m} - \frac{\alpha_i}{2} A_i + \frac{i n_2 \omega_i}{c} \left[\left(f_{ii}|A_i|^2 + 2 \sum_{k=p,s} f_{ki}|A_k|^2 \right) A_i + f_{ppsi} A_p^2 A_s^* \exp\left(-i\Delta\beta z\right) \right], \tag{2.1.16c}$$

Once again, the Raman terms shown in Eq. (2.1.13) are added when appropriate. The linear phase mismatch is given by

$$\Delta\beta = \beta_s + \beta_i - 2\beta_p. \tag{2.1.17}$$

The concept of phase matching is discussed in Sec. 2.1.4. The definitions for the overlap integrals and the dispersion coefficients are the same as in Sec. 2.1.1.

2.1.3 Phase Matching Condition - Dual Pump

The phase matching condition is analyzed by obtaining an analytical solution of Eq. (2.1.7). A solution can be found using elliptic functions [23], although this is

not utilized here. Instead the equations are solved by assuming that the pump is much stronger than the signal and idler, and furthermore considering the pump as being undepleted. Fiber losses are neglected and the fields are assumed to be under quasi continuous wave (CW) conditions, such that all terms involving derivatives with respect to t are ignored [24, 25]. Thus Eq. (2.1.7) is reduced to

$$\frac{\partial A_p}{\partial z} = \frac{in_2\omega_p}{c}\left[\left(f_{pp}|A_p|^2 + 2f_{qp}|A_q|^2\right)A_p\right] \tag{2.1.18a}$$

$$\frac{\partial A_q}{\partial z} = \frac{in_2\omega_q}{c}\left[\left(f_{qq}|A_q|^2 + 2f_{qp}|A_p|^2\right)A_q\right] \tag{2.1.18b}$$

$$\frac{\partial A_s}{\partial z} = \frac{in_2\omega_s}{c}\left[2\left(f_{ps}|A_p|^2 + f_{qs}|A_q|^2\right)A_s + 2f_{pqsi}A_pA_qA_i^*\exp\left(-i\Delta\beta z\right)\right] \tag{2.1.18c}$$

$$\frac{\partial A_i}{\partial z} = \frac{in_2\omega_i}{c}\left[2\left(f_{ps}|A_p|^2 + f_{qs}|A_q|^2\right)A_i + 2f_{pqsi}A_pA_qA_s^*\exp\left(-i\Delta\beta z\right)\right]. \tag{2.1.18d}$$

The solution for the first two equations, Eqs. (2.1.18a) and (2.1.18b), are inserted into Eqs. (2.1.18c) and (2.1.18d). Using a variable transformation the problem is reduced to a set of two coupled equations. By solving these equations, expressions for the power of the signal and idler are obtained:

$$P_s(z) = P_s(0)\left[1 + \frac{4\delta_s\delta_i f_{pqsi}^2 P_pP_q}{g^2}\sinh^2\left(gz\right)\right] \tag{2.1.19}$$

$$P_i(z) = P_s(0)\frac{4\delta_i^2 f_{pqsi}^2 P_pP_q}{g^2}\sinh^2\left(gz\right), \tag{2.1.20}$$

where the power is given by $P_n = |A_n|^2$. Furthermore, the following notations are introduced

$$\delta_n = \frac{\omega_n n_2}{c} \qquad n = p, q, s, i \tag{2.1.21}$$

$$g^2 = \underbrace{4\delta_s\delta_i f_{pqsi}^2 P_pP_q}_{Q} - \left(\frac{\kappa}{2}\right)^2 \tag{2.1.22}$$

The effective phase mismatch parameter, κ, is defined as

$$\kappa = \Delta\beta + \underbrace{P_p\left(2\delta_s f_{sp} + 2\delta_i f_{ip} - 2\delta_q f_{qp} - \delta_p f_{pp}\right) + P_q\left(2\delta_s f_{sq} + 2\delta_i f_{iq} - 2\delta_p f_{qp} - \delta_q f_{qq}\right)}_{M}, \tag{2.1.23}$$

where $\Delta\beta$ refers to the linear phase mismatch, seen in Eq. (2.1.11), and the second term is called the nonlinear phase mismatch, due to its origin from the SPM and XPM terms.

According to Eq. (2.1.19) the gain is maximum when $\kappa = 0$, or $\Delta\beta = -M$. Notice that perfect phase matching is not required in order to receive gain, since it is sufficient that $g > 0$. It is found that $g = 0$ when

$$\Delta\beta = \pm 2\sqrt{Q} - M. \tag{2.1.24}$$

2.1.4 Phase Matching Condition - Degenerate Pump

In the case where the pump is degenerate, it is possible to obtain similar expressions as those obtained in Sec. 2.1.3. In this case the signal and idler powers are given by

$$P_s(z) = P_s(0)\left[1 + \delta_s\delta_i\left(\frac{f_{ppsi}P_p}{g}\right)^2 \sinh^2(gz)\right] \tag{2.1.25}$$

$$P_i(z) = P_s(0)\left(\frac{\delta_i f_{ppsi}P_p}{g}\right)^2 \sinh^2(gz)\,. \tag{2.1.26}$$

Furthermore, the following notations are introduced

$$\delta_n = \frac{\omega_n n_2}{c} \qquad n = p, s, i \tag{2.1.27}$$

$$g^2 = \underbrace{\delta_s\delta_i f_{ppsi}^2 P_p^2}_{Q} - \left(\frac{\kappa}{2}\right)^2 \tag{2.1.28}$$

The effective phase mismatch parameter, κ, is defined as

$$\kappa = \Delta\beta + \underbrace{2P_p\left(\delta_s f_{ps} + \delta_i f_{pi} - \delta_p f_{pp}\right)}_{M}. \tag{2.1.29}$$

The gain region is still defined within the boundaries given in Eq. (2.1.24).

2.1.5 Linear Phase Mismatch Approximation

In the situation where all the interacting fields are in the same mode, it is possible to describe the linear phase mismatch, $\Delta\beta$, given in Eqs. (2.1.11) and (2.1.17), as a Taylor expansion around the center frequency of the pumps, $\omega_c = (\omega_p + \omega_q)/2$, or in the degenerate case $\omega_c = \omega_p$. This yields

$$\Delta\beta = 2\sum_{m=1}^{\infty} \frac{\beta_{2m,n}}{(2m)!}\Omega^{2m}, \tag{2.1.30}$$

where $\Omega = \omega_c - \omega_s = \omega_i - \omega_c$ and

$$\beta_{2m,n} = \left(\frac{d^{2m}\beta_n(\omega)}{d\omega^{2m}}\right)_{\omega=\omega_c}. \tag{2.1.31}$$

Here $\beta_n(\omega)$ is the propagation constant of the relevant mode.

2.2 Higher Order Modes

In order to facilitate the process of FWM the important criteria of phase matching must be fulfilled. This is given by Eqs. (2.1.11) and (2.1.17), for the general and degenerate case, respectively. Traditionally, this is achieved using only the fundamental mode. In this case, M from Eqs. (2.1.23) and (2.1.29) is positive since all the $\delta_n f_{ij}$ products are roughly of the same size. To have gain around the pump the linear phase mismatch, $\Delta\beta$, must be negative, which from Eq. (2.1.31) leads to a requirement for anomalous dispersion. For FWM using pumps in the telecommunication band the commonly used medium is a highly nonlinear dispersion shifted fiber, since this ensures efficient FWM over a broad wavelength range [26–28]. For FWM using pumps around 1 μm the common approach is to use photonic crystal fibers (PCFs), since strong confinement of the fundamental mode leads to anomalous waveguide dispersion. Thus even when adding the material dispersion the overall dispersion is still anomalous [8, 29, 30]. The small effective area limits the possible power levels, which are possible in the fiber before dielectric breakdown occur. This is partly the motivation for using HOMs, since in this situation the desirable anomalous dispersion is obtained without sacrificing the mode area. Furthermore, it is possible to fulfill the phase matching condition by selecting the interacting waves in different modes. Thus by utilizing this intermodal approach a new degree of freedom is obtained. Besides from choosing between different modes, it is of course still possible to tailor the dispersion properties of the individual modes [31–33].

The fibers used in this project are double clad fibers, where the outer cladding region is either down doped or an air cladding structure. The fibers have a single moded core, therefore it is possible to launch all the light in the fundamental mode, and then by using a long period grating (LPG) the light is converted to a desired HOM. More details regarding the fibers are found in Chap. 3. The grating fabrication method used results in UV-induced symmetric gratings, hence since the fundamental mode is symmetric it is only possible to convert to symmetric modes, such as the LP_{0X} modes. More details on gratings are found in Chap. 4. The LP_{0X} modes are an abbreviation for linear polarized modes, which are degenerate linearly polarized pairs of the HE_{1X} vector modes. Whereas, the LP_{1X} modes are pairs from four degenerate vector modes [34–36]. The intensity distribution of the LP_{0X} modes consist of a peak at the center surrounded by concentric rings, three examples of LP_{0X} modes calculated for a simple step index fiber are shown in Fig. 2.1.

In the case of a single step index multimoded fiber the radial component is described by Bessel functions. The LP_{0X} modes are, in other words, bounded Bessel beams, therefore the LP_{0X} modes also possess similar properties. It is mathematically proven that Bessel beams are divergence free and hold self-healing abilities, in the sense that the mode pattern is regenerated behind opaque obstacles at a lower power [37, 38]. It has been shown experimentally that higher order of LP_{0X} modes are divergence resistant over several Rayleigh

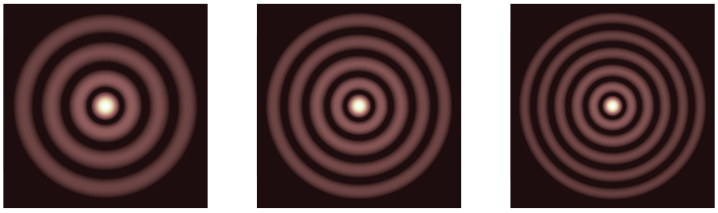

(a) LP_{04}. (b) LP_{05}. (c) LP_{06}.

Figure 2.1: Example of intensity distribution of LP_{0X} modes.

lengths, and that they are self-healing [17,18,39]. These optical properties could prove useful for some applications of fiber lasers, for instance within the fields of biology, imaging, and optical trapping [40, 41]. However, if the fundamental mode is desirable at the output of the device, it is of course possible to convert back to the fundamental mode using LPGs, as these are reciprocal devices.

A crucial aspect in utilizing HOMs is their ability to propagate stably over lengths of fiber. There are two sources of instability related to fiber propagation, namely mode distortion and mode coupling. Mode distortion could be caused by fabrication errors leading to non-ideal index profile, or it could be introduced via perturbations of the fiber, such as bending. In fact, a bent fiber may be perceived as a non ideal index profile, since the introduced path length difference effectively is equivalent to a tilted index profile, this is illustrated in Fig. 2.2 [9, 42].

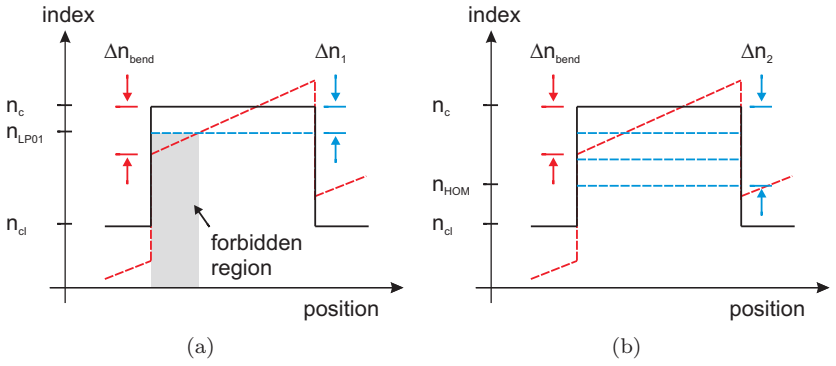

Figure 2.2: The black lines are the index profile for the straight fiber, and the red lines are the effective index profile for the bent fiber. (a) The blue line is the effective index for the fundamental mode, notice that in some region this is lower than the effective index profile. (b) Each blue dashed line represents a higher order mode with increasingly lower effective indices. Notice that for higher order modes the effective index of the mode is lower than the effective index profile.

In Fig. 2.2(a) it is illustrated what occurs as the fundamental mode prop-

agate through a bent fiber. It is seen that part of the tilted equivalent index profile is lower than the effective index of the mode, $\Delta n_1 < \Delta n_{bend}$. As a consequence, a forbidden or evanescent region is created where it is not possible for the mode to exist. Therefore, the mode is distorted as it squeezes into the remaining part of the core. It has been experimentally confirmed that the decrease in the effective area increases the nonlinearity in the fiber [43]. Fig. 2.2(b) shows that for higher order of modes, the tilted equivalent index profile remains larger than the effective index of the mode, $\Delta n_2 > \Delta n_{bend}$, therefore a forbidden region is not introduced. Using this argument, it is seen that HOMs are less sensitive to fiber bends than the fundamental mode. The consequence of bends is increased loss, and if the bends are non-adiabatic the introduced distortion of the mode could also lead to mode coupling. Experimentally, it is demonstrated that the LP_{03} mode is more sensitive to bends than the LP_{07} mode [9].

The second cause of instability is related to mode coupling, since the LP_{0X} modes are all symmetric and random perturbations are most likely asymmetric and occur over long length scales. This means that the critical mode coupling occurs between the LP_{0X} mode and the LP_{1X} mode with the nearest effective index [10]. The parameter $n_{LP_{0X}} - n_{LP_{1X}}$ is in the following referred to as the critical mode spacing. For all modes the critical mode spacing decreases as the effective area increases. Once the critical mode spacing is below a certain threshold, it is assumed that mode coupling has become a serious problem. For large mode area (LMA) fibers this is assumed to be for an effective area of approximately 800 μm^2 for the fundamental mode [10]. It is possible to extend this limit by ensuring the fibers remain straight. Larger effective areas have also been achieved using microstructured fibers that selectively leak out HOMs [44]. This approach does not reduce mode coupling, it merely mitigates it by ensuring high loss in the HOMs. It is shown that, for a given size of the effective area, the critical mode spacing is an order of magnitude larger for the HOMs in a double clad fiber compared to the fundamental mode in a LMA fiber [10]. Furthermore, the critical mode spacing is seen to increase with increasing mode order [10]. This proves that mode coupling is less of a problem for HOM. This has been experimentally proven in an erbium doped fiber amplifier (EDFA) using a LP_{014} mode with an effective area of 6000 μm^2 [45]. The claim that ever increasing mode order leads to less mode coupling is expected to breakdown at some point, since the density of states of modes become so large that the stability figure of merit of $n_{LP_{0X}} - n_{LP_{1X}}$ is no longer valid [10].

Finally, it is noted that besides from being attractive for ensuring phase matching for FWM processes, HOMs are also relevant for ultra high power rare earth doped fiber lasers. This is due to the stable propagation that is achievable using large effective areas HOM [45]. With an appropriate fiber design, it is possible to propagate ultra high power levels without limitations due to dielectric breakdown and undesirable nonlinearities.

2.2.1 Modesolver

The modes are found by solving the transverse problem seen in Eq. (2.1.6), where the nonlinear contribution of the dielectric function is neglected. The fiber designs utilized in this thesis are axially symmetric, thus the transverse problem is transformed into polar coordinates using a general solution of the form [35]

$$E(\rho, \theta, z) = F(\rho) \exp(im\theta) \exp(i(\beta z - \omega t)z), \tag{2.2.1}$$

where ρ and θ are the polar coordinates, and m is the angular eigenvalue. By inserting the general solution the transverse problem becomes

$$\frac{d^2F}{d\rho^2} + \frac{1}{\rho}\frac{dF}{d\rho} + \left(n(\rho)^2 k_0^2 - \beta^2 - \frac{m^2}{\rho^2}\right) F = 0. \tag{2.2.2}$$

The modes of interest are mainly the $\mathrm{LP}_{0\mathrm{X}}$ modes, therefore a simple scalar modesolver was developed using the finite difference method. Strictly speaking, the scalar approximation is only valid for small index steps or if the wavelength is short compared to the length scales of the waveguide structure [46]. This means that the strength of the electric field or its derivative must be sufficiently low at the high index step [47]. The scalar modesolver was used for most of the mode simulations, since the inaccuracy was estimated to be counter balanced by the reduced computational time. The final design was verified using COMSOL, which is a commercial available finite element method (FEM) simulation tool.

In the finite difference approach all the derivatives are approximated, and the equation Eq. (2.2.1) is discretized and rewritten into an eigenvalue problem of the form

$$\mathbf{M}\mathbf{E}_\mathbf{r} = \beta^2 \mathbf{E}_\mathbf{r}, \tag{2.2.3}$$

where $\mathbf{M}$ is the quadratic discretization matrix of the finite-difference problem, and $\mathbf{E}_\mathbf{r}$ is a vector containing the electric field. The discretization matrix and the boundary conditions are provided in App. B.

For the discretization of the index profile, an interpolation is used at the discontinuities of the index profile, since this improves the accuracy of the simulation. The refractive index of silica is defined using the Sellmeier equation [48]. It is assumed that all index steps in the fiber design are independent of wavelength, meaning that the refractive indices of the doped regions are given by a constant offset relative to silica.

2.3 Long Period Grating Theory

In order to obtain controlled coupling between desired modes, gratings are utilized. Gratings are essentially periodic perturbations along the fiber, with a period that matches the beat length between two modes. The gratings of interest

in this project are transmission gratings where the modes are co-propagating, also referred to as long period gratings (LPGs). Typical grating periods are on the order of hundreds of microns. The name arises because the grating period is long compared to Bragg gratings, since these are reflection gratings.

The index perturbation along the fiber must occur over only part of the cross section area, in order for the grating to break the orthogonality between the modes and enable mode coupling. In the following, it is assumed that the perturbation is induced in the core of the double cladding fiber. The definitions for the values of the index perturbation used in this section are illustrated in Fig. 2.3.

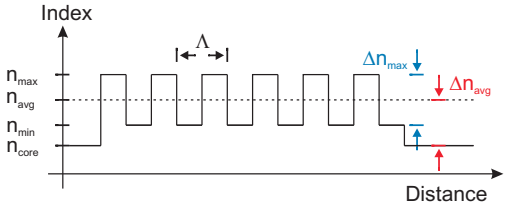

Figure 2.3: The perturbation of the index in the core along the fiber axis. The pitch is defined by Λ, whereas the maximum peak to peak amplitude is given by $\Delta n_{\max} = n_{\max} - n_{\min}$ and the average index of the perturbation is given by $\Delta n_{\text{avg}} = (n_{\max} + n_{\min})/2$.

The governing equations are derived from traditional mode coupling theory [49]. In the process it is assumed that the index perturbation is uniform over the perturbation cross section of the fiber. Also, coupling is only considered between a core and a cladding mode. This means that coupling between cladding modes are neglected, which is a good assumption since the cladding modes have less field in the core i.e. the perturbation area. The longitudinal coupling coefficient is also neglected; this is reasonable since the transverse field components are larger than the longitudinal field components. Finally, only nearly phase matched terms are considered, meaning that fast oscillating terms are neglected, also known as the synchronous approximation [50]. This leads to the following set of first order differential equations

$$\frac{dA}{dz} = -i\sigma_A A(z) - i\kappa^* B(z) \exp(i\delta z) \tag{2.3.1a}$$

$$\frac{dB}{dz} = -i\sigma_B B(z) - i\kappa A(z) \exp(-i\delta z)\,. \tag{2.3.1b}$$

Here $A(z)$ and $B(z)$ are the envelope of the two co-propagating modes. The coefficients are given by the following overlap integrals

$$\kappa \propto \int \Delta n_{\max} E_A E_B \mathrm{d}A_{\text{per}} \tag{2.3.2a}$$

$$\sigma_x \propto \int \Delta n_{\text{avg}} E_x E_x \mathrm{d}A_{\text{per}} \qquad x = A, B, \tag{2.3.2b}$$

where κ is referred to as the AC coupling coefficient, and σ_n are the DC coupling coefficients. Furthermore, integration is performed over $\mathrm{d}A_{\mathrm{per}}$, which is the grating perturbation cross section area. It is straightforward to show that full conversion is achieved when $\kappa L = \pi/2$ [51]. Otherwise, the grating is referred to as being either under- or overcoupled. Notice that if the perturbation area and one of the modes are symmetric, then it is not possible to couple to an asymmetric mode, since this would yield $\kappa = 0$.

The LPG phase matching parameter, δ, is given by

$$\delta = \beta_A - \beta_B - \frac{2\pi}{\Lambda}. \tag{2.3.3}$$

Here, β_n is the propagation constant of the mode. In the case where the DC coupling coefficients are zero, $\sigma_n = 0$, the maximum coupling occurs for the wavelength where $\delta = 0$. If mode A is the fundamental mode and mode B is a cladding mode, this would result in $\sigma_A \gg \sigma_B$. In this case, non-zero DC coupling coefficients lead to a shift towards longer wavelengths in the maximum coupling wavelength of the gratings [52]. The wavelength shift is typically only a few nanometers, so the condition of $\delta = 0$ is an acceptable initial guess during, for instance a fabrication process. A common way of representing the phase matching condition is to rewrite Eq. (2.3.3) into

$$\Lambda = \frac{\lambda}{\Delta n}, \tag{2.3.4}$$

where Δn is the difference between the effective indices of the modes. The bandwidth of the LPG is related to the slope of the phase matching condition provided in Eq. (2.3.4). By differentiation, one yields

$$\frac{d\Lambda}{d\lambda_{\mathrm{res}}} = \frac{\Delta n_g}{\Delta n^2}, \tag{2.3.5}$$

where Δn_g is the difference between the group indices of the two modes. The grating bandwidth is inversely proportional to the group index difference, Δn_g, between the two modes [53,54]. For a more general expression, Eq. (2.3.3) could be Taylor expanded around the grating resonance wavelength, thereby illustrating that higher order dispersion terms also impact the grating bandwidth, i.e. dispersion difference, dispersion slope difference, etc. [51].

Imagine that mode A is LP_{01} and mode B is some higher order mode $\mathrm{LP}_{0\mathrm{X}}$ in a fiber where the index only decreases as the radius is increased, in other words there is no trenches in the radial index profile. At some short wavelength, both modes are guided in the core, and the ray picture predicts that higher order modes travel at steeper bounce angles, thus $n_{g,B} > n_{g,A}$. As the wavelength increases, the higher order mode gradually transitions into the lower index cladding and the group index of the mode approaches that of the cladding, hence $n_{g,B} < n_{g,A}$. This means that at some wavelength in between it

is valid that $\Delta n_g = 0$, which is known as the turn around point (TAP) [54, 55]. Broad bandwidth LPGs are for instance relevant for conversion of spectrally broad pulses, such as femtosecond pulses. Experimental results for TAP LPGs are discussed further in Sec. 4.7.

2.4 Summary

The most fundamental theory used during this PhD thesis was presented. This includes the general FWM theory, where focus is on outlining the assumptions taken in the derivation of the governing equations. General analytical expressions were also derived for the gain region of the FWM process. These results are used numerous times throughout the thesis. HOMs were discussed next, with a focus on explaining how stable propagation is ensured. Also, the scalar modesolver used in this project was introduced. In the final section, LPG theory was discussed and the basic equations were presented. These gratings are an important aspect of this project since they enable mode conversion in the fiber.

3

Higher Order Mode Fibers

In this project two fibers were used with the intend to perform higher order mode (HOM) mixing experiments. Fundamentally, these are both double cladding fibers. One is an air cladding fiber fabricated at OFS-Denmark, whereas the second fiber is a custom designed fiber, which is fabricated by Nufern. The airclad fiber was chosen, since it was readily available and it was possible to perform basic HOM four-wave mixing (FWM) experiments with this fiber, while waiting for delivery of the custom designed fiber. However, it turned out that it was not possible to propagate HOMs in this fiber for more than a few centimeters. A full description of the airclad fiber, along with experiments and discussion of results are presented in App. C.

This chapter presents the design and characterization of the custom designed fiber and is organized as follows. Firstly, the fiber design criteria are discussed and the different design parameters are described. Then each of these parameters are discussed and determined. Next, the preform is shown. Lastly, the index profiles are presented, which are measured on the actual fibers.

3.1 Custom Fiber Design Criteria

The basic idea behind the fiber design is to have a double cladding fiber, where the core only guides the fundamental mode, and the HOMs are guided by the inner cladding region. It is desirable for the index step between the core and inner cladding to be low, since this allows for the core radius to be large, while still remaining single moded. This is beneficial for numerous reasons, firstly the large effective area of the fundamental mode decreases the impact of self phase modulation (SPM), which could become problematic in the fiber before the long period grating (LPG), where the modes are still propagating in the fundamental mode, especially for high power applications. Secondly, the large effective area of the fundamental mode decreases the peak intensity of the mode, thus increasing the dielectric breakdown limit of the fiber. Finally,

coupling into the fiber from free space is simplified by having a larger core.

An important fiber design aspect is to ensure the possibility for writing LPGs. In this project, UV-induced gratings are utilized, which are described in detail in Chap. 4. For these specific types of gratings a photosensitive core is the key, which is obtained by germanium doping the core. In order to increase the photo sensitivity, the concentration of germanium in the core is high. However, to ensure that the index step is kept low, the core is co-doped with fluorine, which is known to decrease the index. The efficiency of the LPG coupling is related to the overlap integral between the two modes under consideration, see Eq. (2.3.2). It is important that the overlap integrals between the fundamental mode and the modes of interest are non-zero. In order to obtain control of the overlap integrals the core is segmented. The inner part of the core is the photosensitive germanium and fluorine region, whereas the outer part of the core is doped with phosphorus.

The inner cladding consists of pure silica. The radius of the inner cladding is the main parameter for adjusting the FWM phase matching conditions, since this is the boundary that confines the HOMs. The outer cladding is fluorine doped silica, a large index step is required in order to guide higher order HOMs. The outer diameter of the fiber should be close to 125 μm for it to be compatible with standard fiber components and equipment. A sketch that summaries these general design criteria is seen in Fig. 3.1.

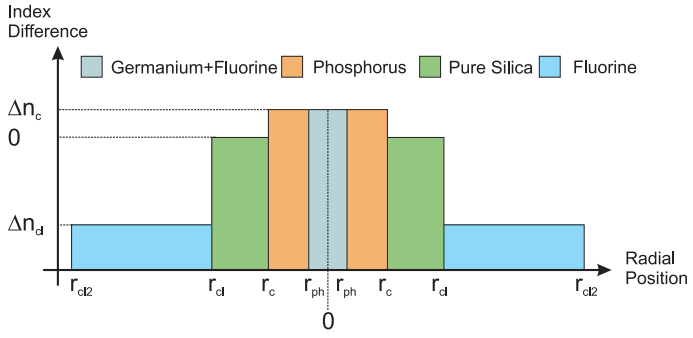

Figure 3.1: Schematics of custom fiber design.

3.2 Final Fiber Design

To maximize the effective area of the fundamental mode, the index step was set to $\Delta n_c = 0.0012$, which is the lower boundary for the index step defined by the manufacture, Nufern. In order to ensure that the core is single moded the core radius was set to $r_c = 7.5$ μm. Calculations examining the impact of SPM when the pump is in the fundamental mode, are shown in Sec. 5.3.2 together with the pulse propagation simulations. The down doped outer cladding region is

realized by collapsing a fluorine doped silica tube onto the central preform. The tube with the lowest index was chosen, since this ensures guidance of the highest number of modes. This had a relative index difference of $\Delta n_{cl} = -0.017$.

3.2.1 Four Wave Mixing Phase Matching Curves

At the point in the project where the fiber was being designed, it was expected that a different pump source was to be used. This had a wavelength tunable range between 1020 and 1040 nm. Therefore, the fiber was designed with the center wavelength of 1030 nm in mind. The pump source was changed to have a tunable range between 1035 and 1055 nm before the fiber preform was drawn. The change in pump wavelength was accounted for by scaling the final fiber draw diameter, as Maxwell´s equations are dimension scalable; this is described further in Sec. 3.3.

In order to determine the outer cladding radius, r_{cl}, the phase matching curves (PMCs) for the FWM process are considered, given by Eq. (2.1.11). The photosensitive core radius, r_{ph}, is determined later, since this value is not crucial yet since the index is the same in both regions of the segmented core. The desired wavelength conversion scenario is pumping in the ytterbium gain band, and having phase matching with a seed in the telecommunication band. It was found that this was obtained by selecting the idler and one of the pumps in a given mode LP_{0m}, while the second pump and the signal are in the mode LP_{0m+1} [56]. The example in Fig. 3.2 shows the linear phase mismatch, $\Delta\beta$, when the idler and pump1 are in LP_{04}, while pump2 and the signal are in LP_{05}. For all examples in this section the pump power is set to 10 kW for each pump. Gain occurs for wavelengths where the linear phase mismatch falls between the horizontal black dashed lines, given by Eq. (2.1.24). The largest small signal gain is obtained at the intersection with the dashed red line. These analytical approximations were discussed further in Sec. 2.1.3. This analytical approach is used in the fiber design section, since it is illustrative and an excellent first order approximation. The full nonlinear simulations are presented in Chap. 5 using the measured index profile for the custom designed fiber. Furthermore, a discussion of the importance of the overlap integral between the selected modes is presented

Fig. 3.2 illustrates how it is possible to obtain almost identical phase matching curves for different separations of the pump wavelengths. This is because the sum of $\beta_{04}(\omega_{p1}) + \beta_{05}(\omega_{p2})$ and the average of the two pump frequencies both remain almost constant. For the remainder of this project, the focus is on the solution where the two pump wavelengths are coinciding. The advantage is that only one pump laser source is needed, since the pump power is divided between the two modes of interest. For other applications where high power is crucial and pump power is the limitation, it is beneficial to have two different pump lasers, and hereby obtaining twice the total pump power. If two pumps are used, Raman amplification between the pumps must be considered since pump power is transferred from the shorter wavelength pump to

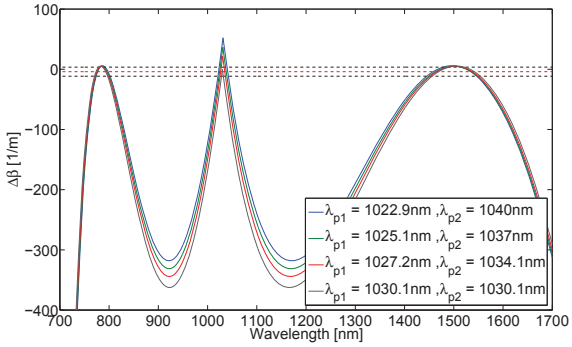

Figure 3.2: Linear phase matching curves. Idler and pump1 are in the LP_{04} mode, pump2 and signal are in the LP_{05} mode. For this fiber design the outer cladding radius was $r_{cl} = 23.8\ \mu$m, whereas the other remaining parameters were as discussed above. The dashed lines are based on the analytical approximation for the phase mismatch. The black dashed lines indicate the boundary of the gain region, whereas the intersection with the red dashed line is the wavelength for maximum small signal gain.

the longer wavelength pump. In this case, it is possible to maximize the total pump power conversion by starting with an initial offset in power between the pumps.

The sensitivity of the PMCs for a change in pump wavelength is illustrated in Fig. 3.3. Both pumps are at the same wavelength, which is indicated by the legend. The parameters for the fiber design are the same as in Fig. 3.2. It is noticed that a change of less than 1 nm significantly changes the PMCs.

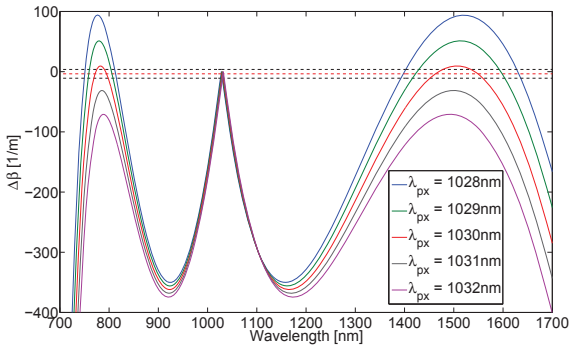

Figure 3.3: Linear phase mismatch for different pump wavelengths, the outer cladding radius is $r_{cl} = 23.8\ \mu$m.

The sensitivity toward changes of the fiber dimensions is investigated in

Fig. 3.4(a). Here it is shown how changes in r_{cl} of 0.5 μm steps radically impact the PMCs. It is however possible to compensate this by changing the pump wavelength accordingly. This is shown in Fig. 3.4(b), where similar PMCs are obtained for the three different fiber designs shown in Fig. 3.4(a). This illustrates the importance of having a wavelength tunable pump source, since this allows for tuning of the PMCs, which is necessary due to discrepancies between the fiber design and the actual fiber, or to compensate for potential difference between simulations and the actual fabricated fiber. For the specific design, it is shown that a change in r_{cl} of 0.5 μm requires a change in the pump wavelength of 5 nm. A discussion of the impact of outer diameter (OD) fluctuations along the fiber is provided in Sec. 5.4. Finally, it is mentioned

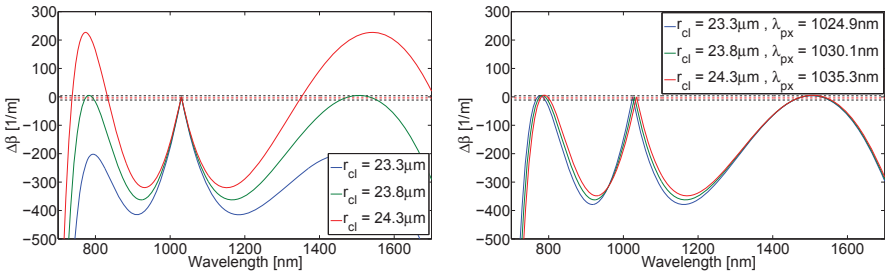

Figure 3.4: (a) PMCs for three different fiber designs, where the only parameter changed is r_{cl}. The pump wavelength is $\lambda_p = 1030.1$ nm. (b) For the three fiber designs it is shown that similar PMCs are obtained by selecting the pump wavelength accordingly.

that for the specific fiber design other interesting HOM FWM processes are possible, for instance the case where all interacting fields are in the same modes, and where the pump is degenerate. Fig. 3.5(a) shows the PMCs when all fields are in the LP_{07} mode for different pump wavelengths. For all the pump wavelengths shown, the dispersion is anomalous. This results in modulation instability around the pump, which is a well known FWM process when all fields are in the fundamental mode. In Fig. 3.5(b) all fields are in the LP_{06} mode. In this case, the pump exhibits normal dispersion, therefore resulting in a broad wavelength conversion between wavelengths where the first two terms in Eq. (2.1.30) balance out each other.

The final design was sent to the fiber manufacture, Nufern, before the pump source was changed, hence based on the above consideration it was decided that $r_{cl} = 23.8$ μm. In this section the most interesting PMCs were presented, however there are of course several other possible combinations, since for the designed fiber modes as high as LP_{010} are guided at 1050 nm.

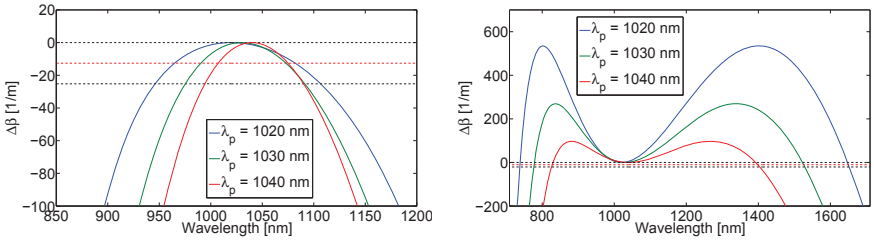

(a) (b)

Figure 3.5: (a) PMC for the degenerate case, where idler, pump, and signal are in the LP_{07} mode. (b) PMC where all fields are in the LP_{06} mode.

3.2.2 Photosensitive Core

The final question regarding the fiber design is where to divide the segmented core. The aim is to maximize the LPG coupling coefficient for the modes of interest, see Eq. (2.3.2). In order to illustrate this the normalized fields for the fundamental mode and the three modes of interest are shown in Fig. 3.6(a). In Fig. 3.6(b) the normalized overlap integral between the fundamental mode and different HOM are shown as a function of radius, this is used to determine the radius of the photosensitive region. In mathematical terms the overlap integral, which is proportional to the coupling coefficient, is given by

$$O\left(r_{ph}\right) = \frac{1}{N}\int_0^{2\pi}\int_0^{r_{ph}} E_{LP_{01}}\left(r\right) E_{LP_{0X}}\left(r\right) r dr d\theta, \tag{3.2.1}$$

where r_{ph} is the photosensitive core radius and N is the normalization. Since the field of the fundamental mode is always positive, the peak of the overlap integral occurs at the radii where the HOMs exhibit phase changes. In order to have an acceptable overlap integral to LP_{04}, LP_{05}, and LP_{06}, the photosensitive core radius is fixed at $r_{ph} = 3.5$ μm.

3.2.3 Summary of Custom Design

The final values of the design parameters, defined in Fig. 3.1, are provided in Table 3.1. The relative index is given with respect to the refractive index of pure silica. A region is defined from the radius of the former region to the radius of the current region, e.g. the inner cladding region is defined from 7.5 to 23.8 μm.

3.3 Preform

Using the design specifications summarized previously, the preform was manufactured by Nufern. A measurement of the relative index profile of the preform

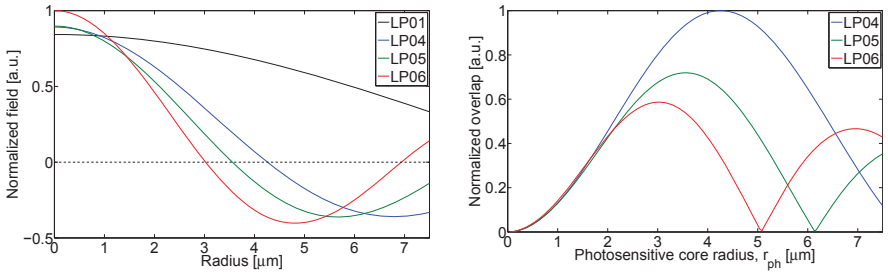

(a) (b)

Figure 3.6: (a) Fields in the custom designed fiber for modes of interest are plotted. The radius of the core is $r_c = 7.5$ μm. (b) Overlap integral between the fundamental mode and the HOM indicated by the legend as a function of the radius of the photosensitive region.

Region	Photosensitive	Core	Inner cladding	Outer cladding
Radius [μm]	$r_{ph} = 3.5$	$r_c = 7.5$	$r_{cl} = 23.8$	$r_{cl2} = 62.5$
Relative index	$\Delta n_c = 0.0012$	$\Delta n_c = 0.0012$	0	$\Delta n_{cl} = -0.017$

Table 3.1: Summary of fiber design parameters.

performed by Nufern is seen in Fig. 3.7. The blue line is the actual measurement. It is believed that the rounding occurring between the inner and outer cladding is an artifact in the measurement, hence for all simulations the approximated red dashed line was used. The index step at the core is found at

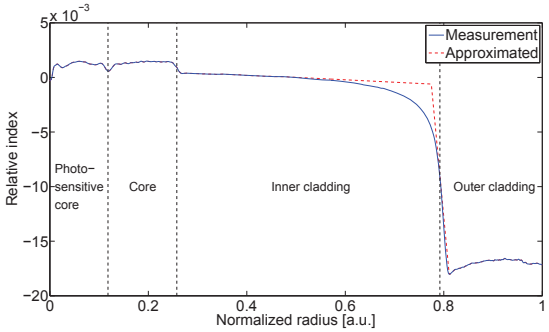

Figure 3.7: Relative index profile for the preform showing the core and inner cladding.

$\Delta n_c = 0.0011$, and the ratio between the radii were found at $r_{cl}/r_c = 3.07$, whereas the ratio of the design was 3.17. Thus the preform was found to satisfy the specifications. The FWM PMCs were considered in order to determine

the final fiber draw diameters. Five different diameters were chosen to ensure that, together with the tunable laser source, it is possible to get the desirable PMC. At this point in the project the pump source was changed to have a wavelength tunable range from 1035 to 1055 nm. The draw diameters were chosen to compensate for the change of pump wavelength. Since the index profile was impacted by the draw process, these simulations are not included in this thesis. Instead, simulations are presented in the following section, using the measured index profile for the drawn fibers.

3.4 Fiber Drawing Diameters

The preform was drawn into five different fiber diameters; these have an outer diameter (OD) of 110, 115, 120, 125, and 130 μm. The microscope image of the 130 μm OD fiber is seen in Fig. 3.8. The core, inner cladding, and outer

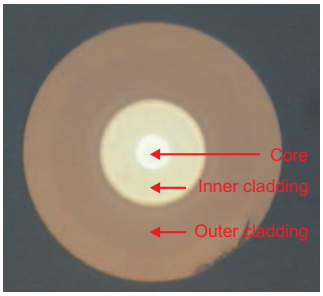

Figure 3.8: End facet view of the 130 μm OD fiber.

cladding regions are clearly seen on the image.

The index profile relative to silica of the fibers with the smallest and largest OD were measured. The results are seen in Fig. 3.9(a). The radius is normalized to the specified outer radius. It is noticed that the index profile is more rounded between the inner and outer cladding for the 90° measurements. This was observed for all measurements after the fiber had been rotated after the initial measurement, hence it is attributed to an artifact from the profile measurement system, IFA-100 Fiber analyzer. Notice that the 110 and 130 μm ODs are near-perfect scaling of each other. It is noticed that the index of the core is no longer flat as was the case for the preform in Fig. 3.7. As a consequence of this the core is not single moded, which is discussed further in Sec. 4.6. Fig. 3.9(b) shows the relative index profile for the fiber with an OD of 130 μm after different exposure times to 244 nm UV-light. This was performed to ensure that the germanium doping is only in the specified photosensitive region of the core. As seen from the figure, this turned out to be accurate.

The desirable PMCs in Sec. 3.2.1 were demonstrated for the case where the idler and half of the pump power are in the LP_{04} mode, while the other half

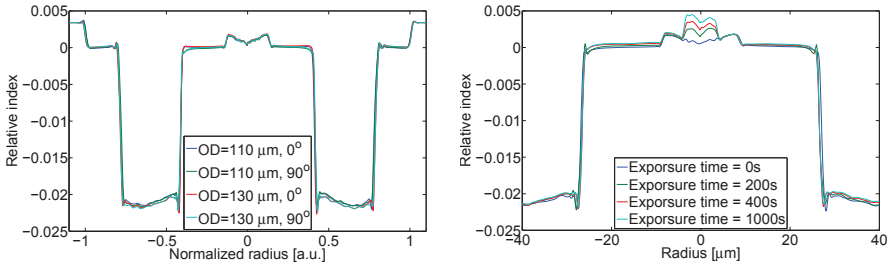

(a) (b)

Figure 3.9: (a) Relative index profile for the 110 and 130 μm OD fibers measured along perpendicular lines across the fiber. (b) The 130 μm OD fiber after different exposure times of 244 nm UV-light.

of the pump power and signal are in the LP_{05} mode; from now on referred to as the 4455 mode combination. Similar PMCs are possible for different $xxyy$ mode combinations (where $y = x+1$) by scaling the fiber design or choosing the pump wavelength accordingly. For the five different drawn fibers, a summary of their desirable PMCs are seen in Table 3.2, where the pump wavelength is in the range between 1000 to 1100 nm. The columns in the table are the fiber OD, the mode combination, the pump wavelength, λ_p, which leads to the desirable PMCs, and the center signal wavelength of the gain region, λ_s. It is

Fiber OD [μm]	Mode combination	λ_p [nm]	λ_s [nm]
110	3344	1064.6	1600
110	4455	1016.2	1495
115	3344	1074.9	1600
115	4455	1026.8	1492
120	3344	1084.5	1592
120	4455	1036.7	1492
125	3344	1093.5	1585
125	4455	1045.9	1492
130	4455	1054.2	1494
130	5566	1005.7	1497

Table 3.2: Summary of desirable PMCs for the five fiber ODs.

seen from the table that in order to obtain similar desirable PMCs, every 5 μm change in fiber OD corresponds to about 10 nm change in pump wavelength. The pump laser has a 20 nm tunable range, hence if a given fiber does not provide the desirable PMCs, it is possible to choose an adjacent fiber OD and possibly obtain the desirable PMCs. In other words, the five different ODs

are equivalent to having a single OD and a pump source with a tunable range of 50 nm. This ensures that even with inaccuracy related to measuring the index profile, and general uncertainty between simulations and experiments; it is likely to find a mode combination, fiber OD, and a pump wavelength that provide the desirable PMC.

Content related to LPG PMCs for the fiber, single mode behavior of the core, and propagation stability for the custom designed fiber are presented in Chap. 5.

3.5 Summary

The design criteria for the custom designed fiber were presented. Subsequently, all the parameters were determined for this specific double cladding fiber with a segmented core. A summary of the design is provided in Sec. 3.2.3. The manufactured preform was presented, which was in excellent agreement with the design criteria. Finally, the measured refractive index profile of the fiber was shown, and it was discovered that the core changed slightly in the drawing process. Based on simulations of the measured index profile, a table summarizing useful phase matched FWM processes was provided for the five different fiber ODs.

4

Mode Conversion

This chapter concerns mode conversion. After a brief description of different mode conversion methods, the following sections are devoted to the fabrication process and characterization method used for the mode converters utilized in this project. After this the mode converters fabricated in the custom designed fiber are shown. This includes a description of the mode stripping methods that were developed for this specific fiber. Finally, a discussion on broad bandwidth mode converters is included, the so called turn around point (TAP) gratings.

4.1 Excitation of Modes

In order to enable devices operating with higher order mode (HOM) it is critical to possess the ability to excite a specific mode in the HOM fiber. Preferably this should occur with low insertion loss and furthermore with high mode extinction, meaning that only the desirable mode should be excited with high modal purity without coupling to any other modes.

Mode converters are generally categorized in two classes: transverse and longitudinal converters. The former group includes holographic plates, phase plates, and spatial light modulators. As the names imply these all induce a phase change over the transverse cross section the mode. The disadvantage with these methods is that they are all free space elements. Since the intended applications for this project occur in fibers, it introduces unnecessary complications and higher insertion loss compared to in-fiber longitudinal converters, such as long period gratings (LPGs).

LPGs enable resonant coupling between two co-propagating modes, provided that the period of the grating matches the beat length between the two modes. Typically the period is around 100-300 μm. For theory on LPGs see Sec. 2.3. The mode coupling with LPGs is achieved with insertion loss of less than 0.1 dB, and with mode extinction of more than 20 dB [57]. Grating fabrication is a fairly mature technology since over the past decades it has been

driven by numerous applications e.g. band-rejection filters, gain flattening filters, sensors, broadband polarizers, and variable optical attenuators [58–61].

Several different methods for obtaining LPGs have been demonstrated, including microbend gratings where mechanical bends of the fiber are introduced. For such gratings the different path lengths introduce an effective index change asymmetrically though the grating [62,63]. Alternatively, a CO_2-laser has been used to introduce density variations or to remove part of the fiber along the grating [64–66]. Another approach uses high powered infrared (IR) femtosecond lasers to induce damages in the silica bonds, which leads to increases in the refractive index. This is obtained either via multi photon absorption, type I process, or using direct ionization of the molecules, type II process [67, 68]. Using these processes damage gratings have been demonstrated [69]. Finally, a photorefractive effect occurring when germanium doped silica is exposed to ultraviolet (UV) light, typically at 193 or 248 nm, can be exploited. This effect was first observed by Hill et. al [70]. Later, it was discovered that the photorefractive effect was enhanced if the fiber was previously loaded with hydrogen [71]. There are still some controversy regarding the details of the exact process, however it is widely accepted that H_2 molecules react with Si-O-Ge sites in the lattice, resulting in the formation of Si-OH bonds, which leads to an increase in the refractive index. Previously, coupling from LP_{01} to the LP_{02} mode using UV-induced LPGs has been demonstrated [72].

4.2 Fabrication Technique

A sketch of the setup for fabrication of the UV induced LPGs is seen in Fig. 4.1. The UV source is from Coherent and is called Innova FreD (Frequency-

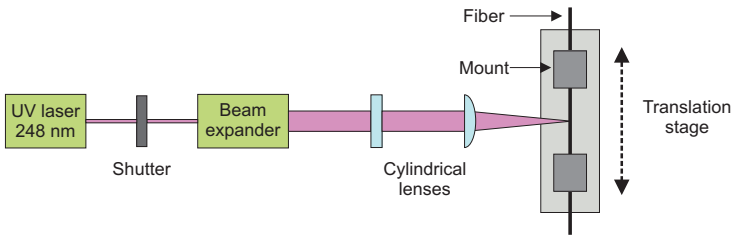

Figure 4.1: Sketch of the LPG fabrication setup.

Doubled). This is a continuous wave (CW) laser at a wavelength of 244 nm. A shutter is located after the output of the laser, followed by a beam expander. Hereafter two cylindrical lenses focus the beam. The fiber is mounted on an Aerotech translation stage, which has a resolution of a few nanometers. The operation principles are to move the fiber while alternatively opening and closing the shutter, hereby writing the grating point-by-point with no need for phase masks. Using a knife-egde measurement it was found that the full width

half maximum (FWHM) of the beam along the axis of translation was 8 μm, thus providing the lower limit of the LPG periodicity. Since the period of the gratings is on the order of 100-300 μm, this yields a nearly rectangular index profile as illustrated in Fig. 2.3.

The fabrication procedure is as follows. First the fiber is placed in a pressure chamber and loaded with hydrogen, hereby increasing the sensitivity of the UV photosensitive process. The coating is removed using a solution of 95 % sulfuric acid and 5 % nitric acid heated to 300 °C. The fiber is placed in the mounts under 200 g of tension to ensure that the fiber is straight. The position of the fiber relative to the beam is adjusted by observing the diffraction pattern from the fiber, which is visible because of generated fluorescence. After the grating is written, which typically takes a few minutes depending on the specific modes, the grating is put in an oven for annealing. The purpose of the annealing is to stabilize the optical properties of the grating. In this process, any unreacted hydrogen is removed and so are some of the UV created sites, which would prove thermally unstable over longer periods of times at lower temperatures [58, 73]. If a strong LPG is desirable, the exposure time is chosen so that the grating is slightly over-coupled. Thereby it is possible to maximize the depth of the grating by heating it, since this decreases the coupling strength of the grating.

4.3 Characterization Techniques

The setup for characterizing the gratings is seen in Fig. 4.2. A broad spectrum

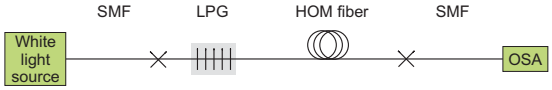

Figure 4.2: LPG conversion characterization setup.

source is coupled into a single-mode fiber (SMF). For simplicity, it is assumed that the fundamental mode in the SMF and the HOM fiber are the same, i.e. the fundamental mode of the SMF is orthogonal to all HOMs of the HOM fiber. This means that mode coupling at the splice points are avoided. After the first splice the LPG converts the light from the fundamental mode to the desirable HOM. When the HOM fiber is spliced to another SMF pigtail, all HOMs are lost and the optical spectrum analyzer (OSA) measures the power of the remaining fundamental mode. By normalizing the measured spectrum with the spectrum of the broad band source, the response of the LPG is obtained. In order to examine whether the grating is under or over-coupled, it is possible to heat the grating and observe whether the strength of the grating increases or decreases.

4.3.1 Modal Interference

If the fundamental mode of the SMF is not orthogonal to the HOMs in the HOM fiber, mode coupling occur at the splice points. Numerous modes are excited in the HOM fiber and they are then partly converted back to the fundamental mode at the second splice point. This leads to multi path interference (MPI) fringes in the measured spectrum. The different mode-paths are illustrated in Fig. 4.3, where in this example the desirable mode is LP_{05}. The strength of the different modes are indicated by the thickness of the arrows.

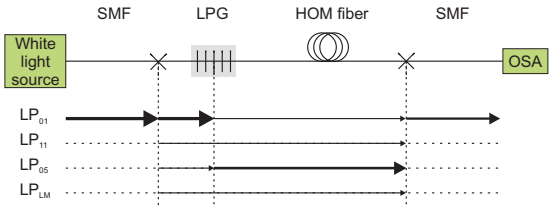

Figure 4.3: The diagram beneath the setup indicates the different mode coupling points in the setup. The thickness of the arrows illustrates the power of the specific modes, at a given point in the setup. Furthermore, distributed mode coupling is also possible in the HOM fiber.

In the case where only two modes are considered, the fluctuation in output power is given by

$$P_{AC} \propto 2\eta^2 \left|E_0\right|^2 \cos\left(\frac{2\pi}{\lambda}\Delta n_{\text{eff}}(\lambda)L\right), \tag{4.3.1}$$

where the power of the modes are $\left|E_0\right|^2$ and $\eta^2\left|E_0\right|^2$, respectively. Thus η^2 is the power fraction of one mode with respect to the other mode. Also, Δn_{eff} is the difference in the effective index between the two modes and L is the length of the interferometric part of the fiber. The fringe spacing is given by [51]

$$\Delta\lambda = \frac{\lambda^2}{\Delta n_g(\lambda)L}, \tag{4.3.2}$$

where Δn_g is the difference in group index between the two modes. This expression is a convenient way to examine which modes are causing the interference or at which points in the setup the interferometer has arisen.

If two modes are present, the depth of the fringes in the spectrum is related to the power division between these two modes. It is straightforward to show that the power fraction of the modes is given by [51]

$$\eta^2 = \left(\frac{10^{\text{ptp}/20}-1}{10^{\text{ptp}/20}+1}\right)^2, \tag{4.3.3}$$

where ptp is the peak-to-peak amplitude in dB of the interference spectrum.

4.4 Characterization of Gratings in Custom Designed Fiber

As mentioned in Sec. 3.4 the custom designed fiber from Nufern was drawn into five different diameters. The fiber used for the final HOM four-wave mixing (FWM) experiments has an outer diameter (OD) of 130 μm, hence in the following, the characterization of only this specific fiber is presented.

In order to experimentally determine the LPG phase matching curves (PMCs), several gratings were written and characterized using the setup shown in Fig. 4.2. The modes of the gratings were verified by imaging them using a camera. Two of these grating spectra, along with the mode images are provided as examples in App. D. A splice recipe was developed between the custom designed fiber and HI 1060 pigtails from Corning, which ensured minimal mode coupling. Examples of four LPG spectra obtained using this splice recipe are seen in Fig. 4.4(a). The exposure time is the same for all four gratings, however the resonances at shorter wavelengths are weaker, which is due to changes in the overlap integral between the modes. In Fig. 4.4(b) all grating resonances are

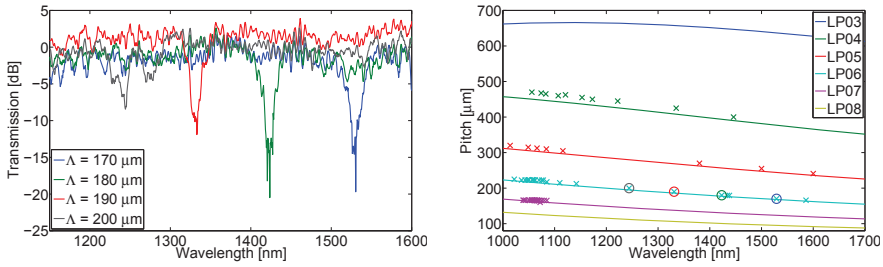

(a) (b)

Figure 4.4: (a) Example of four LPG transmission spectra of the LP_{06} mode, the grating length was $L = 1$ cm, the exposure time was $t_e = 200$ s, and the pitch is indicated by the legend. (b) All the grating resonances are summarized in this plot, the solid lines are the simulated PMCs obtained using the scalar modesolver, and the circles denote the four grating examples.

summarized for the modes of interest for the HOM FWM experiments. The four resonances marked with circles are the four spectra shown in Fig. 4.4(a). The agreement between experiments and simulations is acceptable, and it provides an initial guess of the grating pitch, although grating writing iterations are necessary to get the exact grating recipe. The disagreements between simulations and experiments are generally a constant offset. For LP_{03} the offset is approximately 20 μm. It gradually gets better for increasing mode order, and for LP_{07} it is approximately 4 μm. The disagreement is partly caused by the simulations not accounting for the DC-shift, which leads to a shift of the resonance toward longer wavelengths; this was described further in Sec. 2.3.

For the HOM FWM experiments the written gratings are for the LP_{06} and

LP_{07} modes at the wavelength of 1064 nm. It is seen that, in spite of using the same grating pitch and exposure time, the resonance wavelength varied over tens of nanometers. This is illustrated in Fig. 4.5. It is assumed that the lack

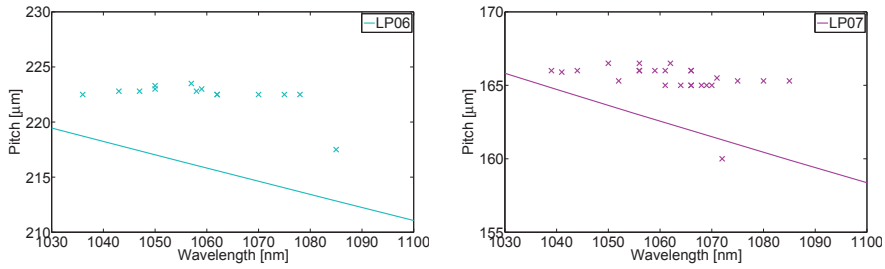

(a) (b)

Figure 4.5: Close-ups of Fig. 4.4(b). (a) For LP_{06}. (b) For LP_{07}.

of reproducibility is caused by fiber OD variations along the fiber. For these modes a change in resonance of 10 nm corresponds to a change in OD of 0.35 %. This leads to a lower yield in fabrication of grating devices. Using the same grating writing setup, numerous gratings have been written in the commercially available HI 980 fiber from Corning, and issues related to reproducibility have not been noticed. Therefore, it is assumed that the variation is not contributed to the fabrication process of the LPGs. The impact OD variations along the fiber has on the FWM process is discussed in Sec. 5.4.

4.5 Grating Devices

For the HOM FWM experiments presented in Chap. 6, three gratings are used. The transmission spectra are presented in Fig. 4.6. During the heating process the grating resonances move toward longer wavelengths, therefore only the two gratings with resonances below 1064 nm were heated. The LP_{07} grating (blue) was over-coupled, hence the heating increased the strength of the grating. On the other hand, the LP_{06} grating (red) was already under-coupled, nevertheless the heating increased the strength at 1064 nm, due to the shift in resonance wavelength. The fringes in the spectra are a clear indication that MPI is occurring, however the optimized splices to HI 1060 pigtails have helped to mitigate this issue. From the spectra the peak-to-peak MPI is found to be between 1 and 1.5 dB. This corresponds to between 0.3 and 0.7 % of the power in another mode, according to Eq. (4.3.3).

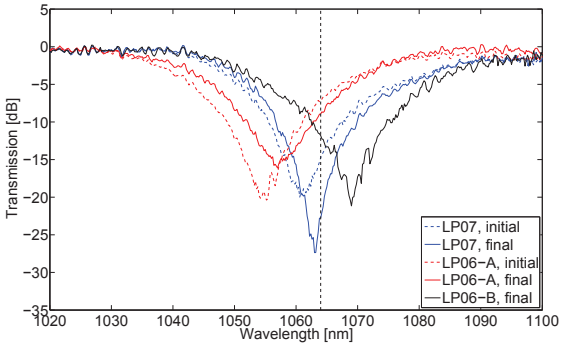

Figure 4.6: Transmission spectrum for the three grating devices. Initial are dashed, and final are solid lines. This refers to before or after heat treatment of the gratings. The transmission at 1064 nm is 22.8 dB for the LP_{07} grating. And 9 dB and 11.8 dB for the LP_{06} A and B gratings, respectively.

4.6 Mode Strip Design

In the HOM FWM experiments light is coupled from free space into the fiber with an OD of 130 μm. As discussed in Sec. 1.2, a 1064 nm Nd:YAG pump source is used. It has a M^2 in two orthogonal directions of approximately 2.55 and 4.39, which was later improved experimentally by spacial filtering in k-space. It proved difficult to excite only the fundamental mode in the fiber when coupling in from free space. Due to several modes being excited it was not possible to simply power optimize the coupling. Even by simultaneously monitoring the mode of the output beam of the fiber, an acceptable result was still not obtained. The solution was to implement a HOM stripper by tapering and etching the fiber. The first step was to taper down the fiber to ensure that the core is single moded, which is illustrated in Fig. 4.7. In Fig. 4.7(a) it is

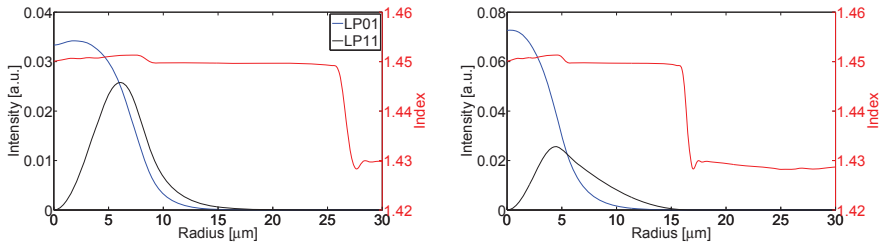

Figure 4.7: The plots show the simulated LP_{01} and LP_{11} modes along with the index profile at 1064 nm. (a) The original fiber with an OD of 130 μm. (b) The same fiber tapered down to an OD of 80 μm.

shown that the core supports both the LP_{01} and LP_{11} mode. In Fig. 4.7(b) it is seen that the tapered fiber is forcing the LP_{11} mode to transition to the inner cladding. The fact that the index profile has peaks at the interface between the core and inner cladding results in an unfortunate excellent support of the LP_{11} mode. It also leads to the dip in the center of the fundamental mode.

The next step is to etch down the fiber beyond the interface between the inner and outer cladding region, hereby enabling striping out all HOM by submerging the fiber in index matching oil. The simulations regarding this step are seen in Fig. 4.8. In Fig. 4.8(a) the fiber is etched down to an OD

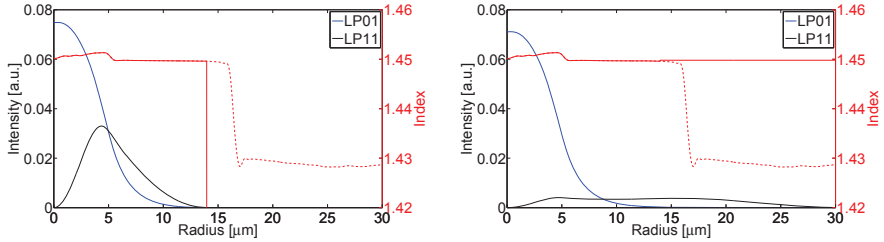

Figure 4.8: The plots show the simulated LP_{01} and LP_{11} modes, along with the index profile at 1064 nm. (a) The fiber tapered down to 80 μm is etched down to an OD of 28 μm. The dashed red line indicates the tapered fiber before etch. The surrounding medium is air, thus the refractive index is 1. (b) The tapered and etched fiber is submerged in index matching oil with an index of 1.4498 at 1050 nm.

of 28 μm. In Fig. 4.8(b) it is seen how the LP_{11} becomes unguided when the tapered etched fiber is submerged in index matching oil, illustrating that it is only possible to propagate the fundamental mode through the mode stripper.

4.6.1 Mode Strip Implementation

After the fiber was tapered, the etching was performed using 49 % hydrofluoric (HF) acid. The diameter of the fiber after etching was verified using a microscope. The mode strips were tested by coupling into the fiber from a free space tunable external cavity laser (ECL). Fig. 4.9(a) is an image of the fundamental mode of the fiber after 14 m of propagation. The outer cladding was etched away and the fiber was submerged in index matching oil to remove inner cladding guided modes, but no initial tapering was performed. It is seen that the mode has a dip at the center, as the simulations predicted in Fig. 4.7(a). Furthermore, even though the coupling was optimized for LP_{01}, a trace of LP_{11} is noticeable with the zero intensity mirror axis along 45 degree. This symmetry axis of the LP_{11} was observed to rotate as the fiber was moved around, clearly indicating the presence of the two modes. In Fig. 4.9(b) the wavelength of the ECL is set at the resonance wavelength of the LP_{06}-B grating. The transmission spectrum is shown in Fig. 4.6, however no index

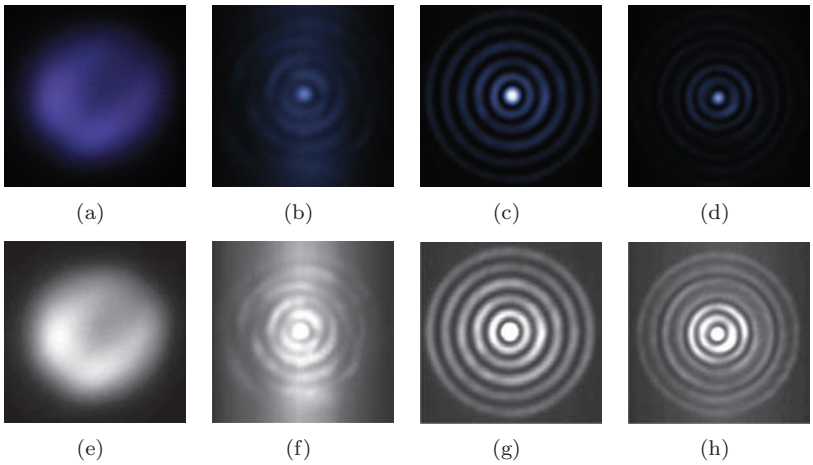

Figure 4.9: (a) Fundamental mode in the 130 μm OD fiber. (b) At resonance wavelength in the LP_{06}-B grating, before adding oil to the tapered etched region. (c) At resonance wavelength in the LP_{06}-B grating, after adding oil to the tapered etched region. (d) At resonance wavelength in the LP_{07} grating, after adding oil to the tapered etched region. (e)-(h) The same images as in the top row, except the contrast is adjusted to enhance certain details (especially useful in the printed version).

matching oil is applied to the tapered etched region, which is located before the grating. Even though a weak trace of LP_{06} is observed the distorted mode image clearly indicate multimode interference. The image in Fig. 4.9(c) is taken using the same setup, with the only difference being added index matching oil. The difference between the two images clearly illustrates that the mode strip is operating according to the simulated expectations. In Fig. 4.9(d) the LP_{07} grating is used and oil has been added; a similar improvement when adding the oil was observed as for the LP_{06}-B grating. In both cases the length of fiber after the LPG was approximately 14 m, and as the fiber was moved around, the images remained practically unchanged, which indicate stable mode propagation. According to simulations, stable propagation should be possible since $n_{\mathrm{LP06}} - n_{\mathrm{LP16}} = 6.8 \cdot 10^{-4}$ and $n_{\mathrm{LP07}} - n_{\mathrm{LP17}} = 8.8 \cdot 10^{-4}$, both are larger than the stable propagation proxy of $1.5 \cdot 10^{-4}$ discussed in [10]. Only in bends of less than a few centimeters were mode coupling observed. The overall coupling loss, both the in-coupling loss and the loss through the mode strip, was measured to be 2.6 dB. The loss was also measured at 1550 nm to ensure propagation of the signal seed through the mode strip; at this wavelength the loss was measured to be 8.2 dB. This is high, although since it is merely used to seed the FWM process, it is not as crucial.

The LP_{06} mode image from Fig. 4.9(c) is plotted using a different colormap in Fig. 4.10(a). The corresponding cuts across the mode cross section are shown in Fig. 4.10(b). It is seen that, even though the mode is very clean, there is some

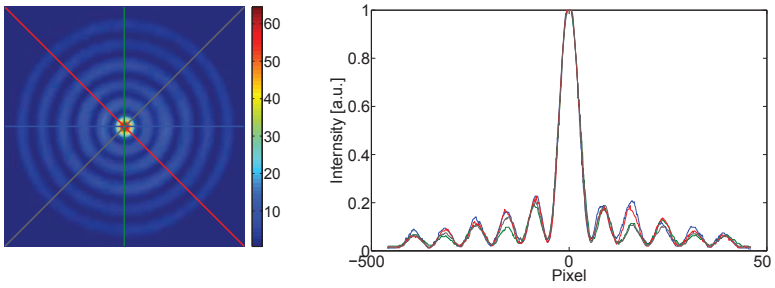

(a) (b)

Figure 4.10: (a) Mode image of the LP_{06} mode, the four colored lines correspond to the different cuts shown on the right plot. (b) Four line cuts along different directions of the mode.

slight asymmetry especially in the second ring. The LP_{07} mode image from Fig. 4.9(d) is plotted using a different colormap in Fig. 4.11(a), the corresponding cuts across the mode cross section are shown in Fig. 4.11(b). As for the

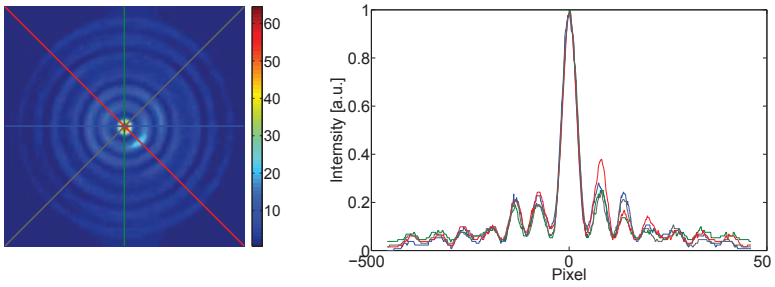

(a) (b)

Figure 4.11: (a) Mode image of the LP_{07} mode, the colored lines correspond to the different cuts shown on the right plot. (b) Four line cuts along different directions of the mode.

LP_{06} case, the mode is fairly clean. However, the LP_{07} mode appears slightly more asymmetric indicating the presence of other modes. The outer rings are very close to the noise floor of the camera. Unfortunately, the limitation is the dynamic range of the camera, since the peak is very close to saturation. The cause of the asymmetries could be due to the cleave or alignment of the imaging system. However, it can not be ruled out that the taper and etched region is non-adiabatic, and thus leading to slight mode coupling.

Even though the end results were satisfactory, the mode strip was an unexpected complication of the device fabrication process. In the design of the fiber it was ensured that the effective area of the fundamental mode was as

large as possible, thus avoiding dielectric breakdown and minimizing self phase modulation (SPM) before the grating. A more conservative core design with a lower numerical aperture (NA) would have been advantageous, since this could have prevented the multimoded core caused by minor fabrication errors.

4.7 Turn Around Point Long Period Gratings

The main feature of TAP LPGs is the broader bandwidth that is obtained. A theoretical description of TAP gratings is provided in Sec. 2.3. For the experimental work presented in this thesis, it is not required to obtain ultra broad LPGs. The largest bandwidth required is approximately 20 nm for the pump wavelength grating to cover the entire tunable range of the pump source. For this purpose, chirped LPGs will be utilized. These are fabricated by varying the pitch along the grating and thereby increasing the bandwidth [52]. Even though ultra broad gratings are beyond the experimental scope of this PhD project, the work carried out related to TAP gratings is included in this thesis for future reference. The increased bandwidth of gratings become relevant for instance for femtosecond pulse wavelength conversion, since this requires grating bandwidths for the seed signal on the order of tens of nanometers. In the experimental work and the simulations presented below, the focus is on creating TAP LPGs at 800 nm for the LP_{014} mode. The fiber used is a Corning HI 780. These specific design goals were chosen because they are relevant to a different project. However the principles could be applied to any wavelength, mode, and fiber.

The HI 780 fiber is a single step index fiber, thus the HOMs are guided in the cladding by the outer silica-air interface. This means that in a coated fiber all cladding guided modes experience high loss. The basic idea is to control the wavelength of the TAP by etching the outer diameter of the fiber. This influences the LPG phase matching conditions, seen in Eq. (2.3.4), since the fundamental mode is core guided and not affected by the etching, whereas the cladding modes are. In Fig. 4.12(a), it is seen how the wavelength of the TAP grating for numerous different modes change as a function of outer fiber diameter. The TAP is shifted to shorter wavelengths for a given mode as the outer fiber diameter is reduced. Specifically, in order to achieve a TAP for the LP_{014} mode at 800 nm it is required that the outer fiber diameter is etched down to approximately 80 μm.
Analytically it is derived that the 10 dB bandwidth of a TAP grating is given by [74]

$$B_{10\mathrm{dB}} = 0.5\Lambda_{\mathrm{res}}\sqrt{\frac{\pi}{2L\left|\frac{\partial^2\Lambda}{\partial\lambda^2}(\lambda_{\mathrm{res}})\right|}}, \tag{4.7.1}$$

where Λ_{res} is the pitch at the resonance wavelength, L is the length of the grating, and λ_{res} is the resonance wavelength. Alternatively, it has been shown

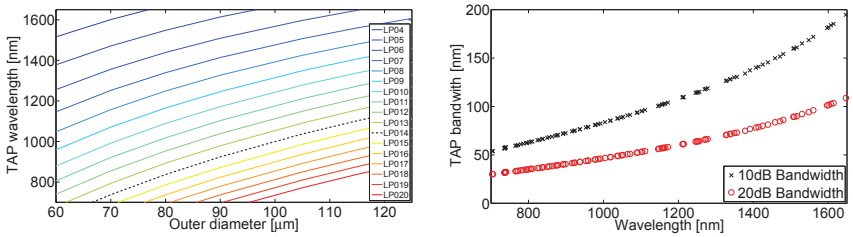

(a) (b)

Figure 4.12: (a) Wavelength of the TAP grating as a function of outer fiber diameter. The mode order is indicated by the legend. (b) TAP grating bandwidth as a function of the grating resonance wavelength.

that the 20 dB bandwidth is approximated by [54]

$$B_{20\mathrm{dB}} = \frac{0.63\lambda_{\mathrm{res}}}{\sqrt{L\Delta Dc}}, \tag{4.7.2}$$

where c is the speed of light in vacuum, ΔD is the difference in group velocity dispersion between the two modes, and the remaining parameters are defined as above. In Fig. 4.12(b) the TAP bandwidths are plotted as a function of the grating resonance wavelength. The ensemble of data points are from fiber diameters ranging from 60 to 125 μm in 5 μm steps, and for all LP_{0X} modes between LP_{02} and LP_{025}. The fact that all data points are placed along the same line indicates that the bandwidth for a certain wavelength is fixed regardless of the mode order.

The etch was performed using 49 % HF acid. The etch rate was found to be 3.48 μm/min. This etch rate was used to determine the outer diameter of the fiber, hereby avoiding measuring the OD using a microscope since this requires extra handling of the fragile etched fiber. The experimental measured spectra at selected fiber diameters along with simulated LPG phase matching curves are shown in Fig. 4.13. It is seen how the two LP_{014} resonances move together as the fiber is etched from an OD of 79 to 78.5 μm, and at an OD of 78.25 μm, the two have merged to form the TAP grating. It is noticed that this is in excellent agreement with the numerically predicted results shown in the top plot. The 10 and 20 dB bandwidths are found at 80 and 50 nm, respectively. This is slightly more than the analytical prediction in Fig. 4.12(b). It is noticed in all spectra that there is a dip for wavelengths less than 860 nm. This is because the pigtails are Corning HI 980, see Fig. 4.2. As normalization for these measurements the two HI 980 pigtails were spliced together, therefore once the grating is spliced in a loss of 3 dB occur at the first splice point for wavelengths below the cutoff wavelength for the HI 980 fiber, which is 860 nm. This is because the HI 980 fiber is multi moded below cutoff, and all HOMs modes are not guided in the single moded HI 780 fiber. Furthermore, it is seen that for the spectrum for the fiber OD of 78.25 μm (black line) there is a loss

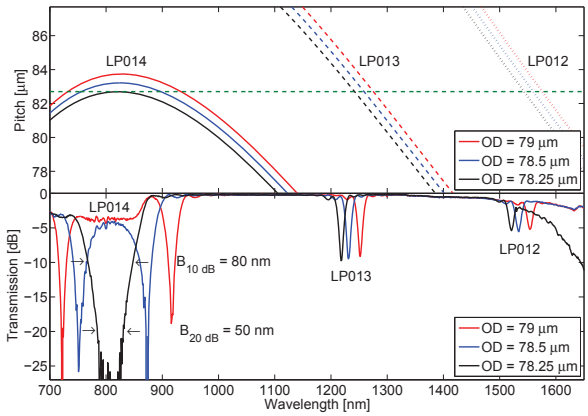

Figure 4.13: The top plot shows the LPG phase matching curves, according to Eq. (2.3.4), the green dashed line indicates the pitch of the grating. The different line styles correspond to different modes given by the text on the figure. The color is related to different fiber ODs as indicated by the legend. The bottom plot shows the measured LPG spectra.

at wavelengths longer than 1500 nm. This is attributed to an introduced bend loss in the setup.

Even though the bandwidths of these gratings are wide enough to convert pulses down to 20 fs, the only consideration has been to obtain a single wavelength where the group index matches between the modes. The group index for the etched gratings are shown in Fig. 4.14 It is seen that the group index

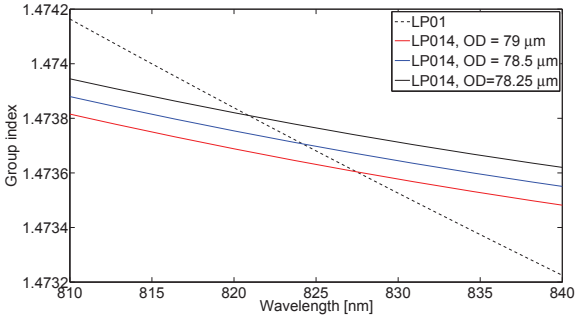

Figure 4.14: Group index as a function of wavelength. For the fundamental mode and the LP_{014} mode for different OD.

for the fundamental mode is not affected by changes in OD, since this is a core guided mode. Furthermore, the group index for the fundamental mode and the HOM are only matched at a specific wavelength and the slope of the

curves are quite different. However, it is possible to obtain greater group index matching by custom designing the fiber. In the following this is illustrated by operating close to a wavelength where a ring of intensity of the LP_{0X} mode is transitioning from the core to the cladding region, since the mode is highly dispersive in this range. The fiber designed to illustrate group index matching is a double cladding fiber, with a core radius of $r_c = 18.9$ μm, numerical aperture of NA = 0.10, and the outer guiding region is a silica-air interface at a radius of $r_{cl} = 62.5$ μm. The group index and the LPG phase matching curves are seen in Fig. 4.15. The top plot shows the group index as a function

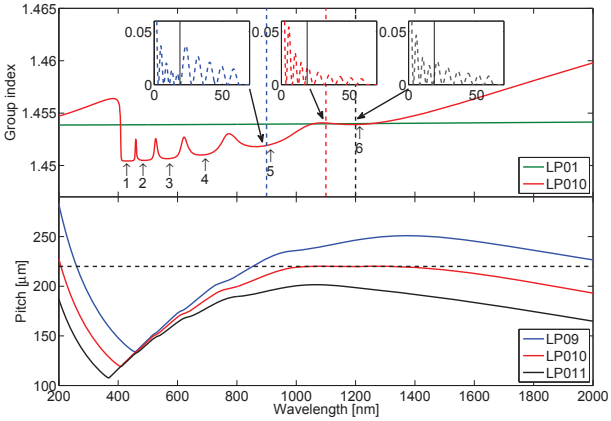

Figure 4.15: The top plot shows the group index for the LP_{01} and LP_{010} modes. The insets show the radial intensity at selected wavelengths indicated by the vertical dashed lines. The number represents the number of rings in the cladding. The bottom plot displays the LPG phase matching curves for a selected number of modes. The black dotted line illustrates the optimal grating pitch in order to obtain a broad bandwidth grating.

of wavelength. At shorter wavelengths the LP_{010} mode is core guided, then around 410 nm the first ring transitions to the cladding and the group index decreases. At 480 nm the second ring has transitioned to the cladding and so on, each transition leads to a small peak in the group index. The number of rings in the cladding are indicated on the plot using the arrows and numbers. The plot insets show the radial intensity profile at the wavelengths indicated by the vertical dashed lines of the same color, namely 900 nm, 1000 nm, and 1200 nm. These wavelengths are selected as they show the transition of the 6th and last ring to the cladding. It is seen that the group index for the LP_{01} and LP_{010} modes are matched and crosses three times over a narrow wavelength range. As shown in the bottom plot, this leads to a triple TAP grating, which results in a grating bandwidth approaching 300 nm.

The large multimoded core of this specific design makes this solution impractical, since it is cumbersome to launch only the fundamental mode in

the fiber. In order to obtain group index matching a design involving several cladding regions is required. This has however not been investigated in this thesis.

4.8 Summary

In this PhD project LPGs are used for in fiber mode conversion. The utilized fabrication setup, which writes the gratings point-by-point, was demonstrated. Furthermore, the method used to characterize the gratings was discussed. Next, it was shown that the simulated grating PMCs agreed well with the experimentally measured gratings resonances, at least to the extend where it provided an excellent initial guess of the grating pitch. However, for the LP_{06} and LP_{07} modes the same grating pitch and exposure time resulted in LPG resonance wavelengths over approximately 40 nm. It was assumed to be caused by fiber OD variations along the fiber. The three final grating devices were presented and by implementing tapered etched regions, which act as mode strips, it was ensured that only light in the fundamental mode reached the gratings. In the LPG power conversion as high as 99.8 % to the desired HOM was obtained. Furthermore, stable propagation over a length of at least 14 m was demonstrated. Lastly, the concept of TAP gratings was examined both theoretically and experimentally. This broadband mode conversion is, for instance, relevant for femtosecond pulses.

5

Simulations for Higher Order Mode Four Wave Mixing

This chapter presents numerical simulations for two different mode combination schemes, which both enable wavelength conversion between a pump in the Ytterbium gain band to wavelengths around 800 nm. These two schemes are illustrated in Fig. 5.1. For the monomode case the pump is wavelength degen-

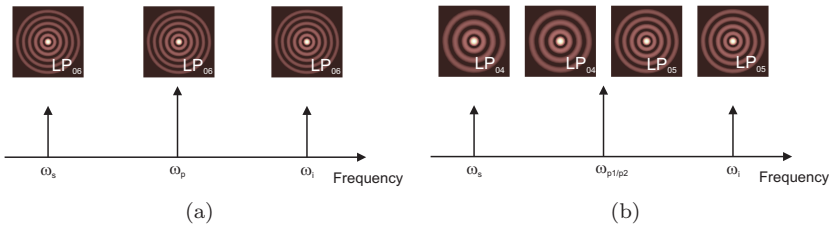

Figure 5.1: (a) Monomode case. The pump is wavelength degenerate and all fields are in the LP_{06} mode. (b) Intermodal case. The pump is wavelength degenerate. The idler and half of the pump power are in the LP_{04} mode, whereas the signal and other half of the pump power is in the LP_{05} mode.

erate and all fields are in the same mode, and in the intermodal case the pump is wavelength degenerate, but the power is divided between two modes [56]. All simulations are carried out using the custom designed fiber from Nufern with an outer diameter (OD) of 125 μm, described in Chap. 3. The pump source used for these simulations is the master oscillator power amplifier (MOPA) described in App. A. The following three sections are devoted to describing the impact of pulse shape, self phase modulation (SPM) of the pump in the fundamental mode before the grating, and the overlap integrals. The next section discusses

dielectric breakdown, along with the possibility of energy scalability when using higher order modes (HOMs). Finally, the impact of outer diameter (OD) fluctuations along the fiber is addressed.

5.1 Monomode Case

In the monomode case, all interacting fields are in the same mode and the pump wavelength is degenerate, thus the governing equations are given by Eq. (2.1.16). The phase matching condition simplifies to an infinite sum of terms that are proportional to the even order dispersion parameters at the pump wavelength, see Eq. (2.1.30). For the considered fiber, the fourth order dispersion parameter at the pump wavelength is negative for all modes, $\beta_{4,n}(\omega_p) < 0$. This means that if the group velocity dispersion (GVD) parameter is positive, $\beta_{2,n}(\omega_p) > 0$, it is possible to obtain phase matching further from the pump wavelength. The GVD for the different modes are seen in Fig. 5.2(a). The four-wave mixing (FWM) phase matching curves (PMCs) are presented in Fig. 5.2(b). All the fields are in the same mode given by the legend and the pump wavelength was chosen at $\lambda_p = 1045$ nm. It is shown that a mode order equal to or less than LP_{06} must be chosen to ensure wavelength conversion below 800 nm. This is ensured, since the two first terms in the linear phase mismatch, see Eq. (2.1.30), yield the required negative value to compensate for the nonlinear phase mismatch, which is indicated by the dashed black horizontal lines that were discussed in Sec. 2.1.4. On the other hand, if a mode larger than LP_{06} is chosen, the first two terms are negative and gain is only obtained around the pump, leading to the characteristic modulation instability (MI). Here the aim is to achieve wavelength conversion to approximately 800 nm, hence below the focus is on the LP_{06} mode.

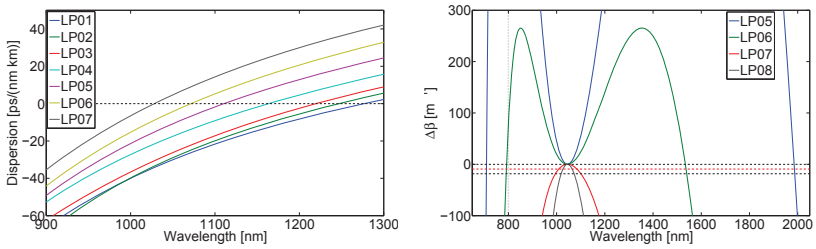

(a) (b)

Figure 5.2: (a) GVD for the lowest order LP_{0X} modes. (b) The FWM PMCs for different set of modes, the degenerate pump wavelength is set at $\lambda_p = 1045$ nm. The vertical dotted black line indicates the target wavelength of 800 nm.

The strength of the different terms in the governing equations, such as the term responsible for FWM, depend on mode overlap integrals, see Eq. (2.1.16).

For the custom designed fiber the HOMs are guided in the inner cladding region. The index step between the inner and outer boundary is $\Delta n \approx 0.02$. Therefore, the modes are highly confined to this region, and the field distribution changes only slightly for different wavelengths. In Fig. 5.3(a) the radial intensity distribution is shown on a logarithmic scale for the LP_{06} mode at five different wavelengths. It is seen that the change in the mode distribution is minor for the five different wavelengths. In Fig. 5.3(b) the effective area for different modes are shown as a function of wavelength. The fundamental

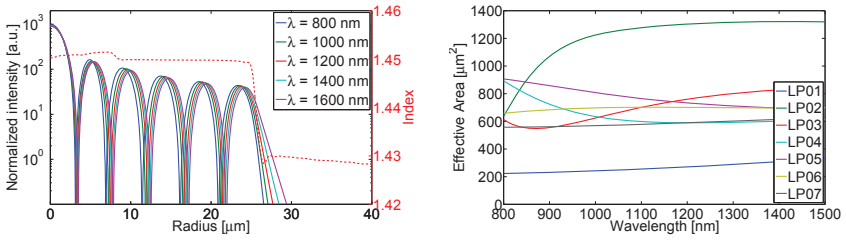

(a) (b)

Figure 5.3: (a) The radial intensity for the LP_{06} mode at five different wavelengths. The red dashed line is the index profile of the fiber at 1050 nm. (b) Effective area for different modes as a function of wavelength.

mode is core guided so the effective area is lower than the other modes. Due to the weak confinement, the effective area changes as a function of wavelength, similar to the fundamental mode of most single-mode fibers (SMFs) or highly nonlinear dispersion shifted fibers (HNLFs). For the specific fiber, the change is about 50 % over the wavelength range. The LP_{02} and LP_{03} modes experience large changes in effective area over this wavelength range, since for these HOMs rings of intensity undergo transitions from the core to the inner cladding. However, the effective area of all higher order modes remain fairly constant around 600-800 μm^2 over the entire wavelength range. From this, it is concluded that the overlap integrals for the FWM process is comparable in magnitude to the overlap integrals of the SPM and cross phase modulation (XPM) terms in the monomode case. In Sec. 5.3.3 it is shown that this ratio is crucial in order to ensure an efficient FWM process.

Previously mentioned, the interesting monomode case is when all interacting fields are in LP_{06}. In Fig. 5.4 the PMCs are shown along with the simulated small signal gain for three different pump wavelengths. The pump power is $P_p = 20$ kW and the fiber length is $L = 1$ m. It is seen that an octave spanning wavelength conversion is achieved for a pump wavelength of 1035 nm. The gain bandwidth is in all three cases only a few nanometers wide. Therefore, to obtain tunability at 800 nm it is required that both the pump and signal sources are wavelength tunable. The phase matching between the signal and idler wavelengths changes significantly by altering the pump wavelength. A discussion of the impact from fiber OD variations on the gain spectrum is

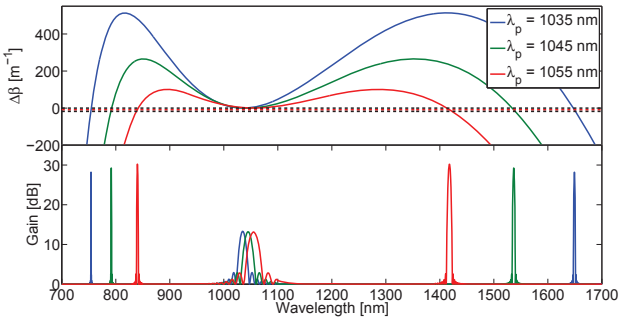

Figure 5.4: On top are the PMCs, the dashed lines indicate the analytical approximation for the maximum gain and gain boundaries. Below are the corresponding gain spectra.

included in Sec. 5.4. Finally, the agreement between the analytical prediction and the simulation is excellent. There are several similarities between this monomode case and FWM at telecommunication wavelengths in dispersion shifted fibers, or in the 1 μm regime where photonic crystal fibers (PCFs) are used to obtain the desirable zero dispersion wavelength (ZDW). The important difference is that in the monomode case pumping occurs around 1 μm in a large effective area mode. Therefore, mode area and power levels are not being sacrificed in order to obtain phase matching, as is the case for PCFs. Thus larger power levels are possible using HOMs. On the other hand higher power levels are also required to have a strong nonlinearity. Dielectric breakdown and energy scalability using HOMs are discussed further in Sec. 5.5.

As pump depletion sets in the wavelength of maximum gain changes from the small signal case presented in Fig. 5.4. Full conversion of all initial pump photons is only achieved with a specific signal wavelength, which is found numerically. The simulations are carried out in the continuous wave (CW) scheme, thus Eq. (2.1.16) are solved when all dispersion terms are neglected. In Fig. 5.5(a) the pump power is seen as a function of fiber length for a range of different signal wavelengths equally spaced between 1434 and 1438 nm. The pump photon efficiency is defined as the fraction of the initial pump photons that are converted to the signal and idler. The optimal conversion length and maximum pump photon conversion as a function of signal wavelength are shown in Fig. 5.5(b). For these simulations, the pump wavelength was $\lambda_p = 1045$ nm, the initial pump power was 20 kW, and all modes were in LP_{06}. The figure shows how both the pump conversion and length for maximum conversion are altered for even a minor change in the signal wavelength. Maximum conversion is obtained at a signal wavelength of $\lambda_s = 1534.67$ nm, and at a length of 3.8 m. The process is sensitive to the choice of signal wavelength. However, the signal is at telecommunication wavelengths, and thus sources with sub-nanometer

accuracy are available.

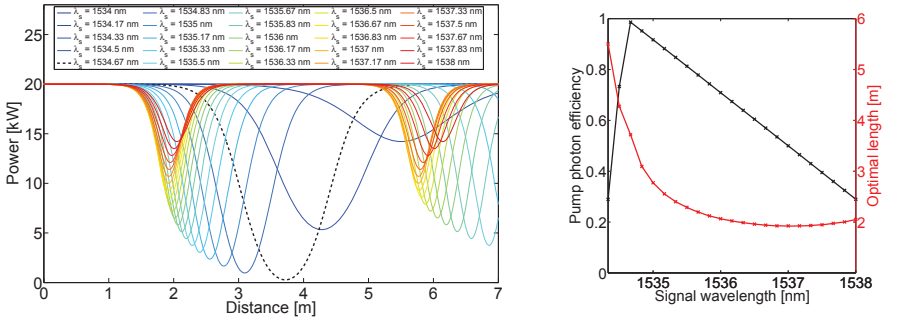

(a) (b)

Figure 5.5: (a) Pump conversion as a function of fiber length for different signal wavelengths. (b) The optimal length and maximum pump photon conversion as a function of signal wavelength.

For the pulse propagation simulations, Eq. (2.1.16), are solved numerically using a developed split step Fourier method [7, 75]. The pulse evolution in the time domain as a function of propagation distance is shown in Fig. 5.6 for the monomode case. The time axis on all figures is a retarded time frame, which moves with the group velocity of the idler pulse. The modes and initial pump

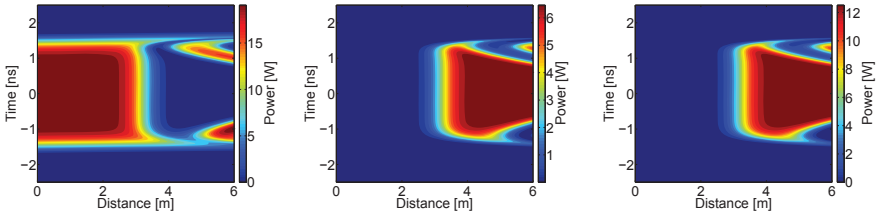

(a) (b) (c)

Figure 5.6: Pulse propagation as a function of distance in a retarded time frame. (a) Pump at 1534.6 nm. (b) Signal at 1534.6 nm. (c) Idler at 792.2 nm.

powers are chosen as above. The CW seed signal wavelength is $\lambda_s = 1534.6$ nm, and the pump pulse shape is a super Gaussian of 10th order with a Gaussian width of 3 ns. This pulse shape was chosen since a flat top pulse increases the conversion efficiency. The impact of the pulse shape is discussed further in Sec. 5.3.1. In any experimental setup the pump pulse is propagating some distance in the fundamental mode before the long period grating (LPG) is reached and the mode is converted to a HOM. During the distance where the field is in the fundamental mode, the effective area is small relative to the HOMs, thus the pump pulse is spectrally broadened due to SPM. Even though

the effective area of the fundamental mode is small, dielectric breakdown in the fiber is not an issue; this is discussed further in Sec. 5.5. In the design of the fiber it was ensured that the area of the fundamental mode was maximized. For this fiber the effective area is 247 μm^2, which leads to an nonlinear length of 7.9 cm [7]. In the simulations, the SPM induced broadening is accounted for by initially propagating the pump field a length of 20 cm in the fundamental mode. This length was chosen since it allows for practical handling of the device during an experiment. The impact of this initial SPM length is discussed further in Sec. 5.3.2. From Fig. 5.6 it is noticed that dispersion is not causing significant broadening of the pulses. It merely leads to slight asymmetries of the pulses, i.e. dispersion effect only plays a minor role on pulse shaping. This is expected since the pulse width is broad, thus in this quasi-CW regime, the dispersion length is thousands of kilometers. Furthermore, the optimal conversion length is only a few meters, hence temporal walk off between the pulses is almost neglectable. The walk off is largest between the signal and idler, and in this case a 3 ns walk off requires a propagation length of 98 m.

To evaluate the maximum conversion distance the pulse energies are plotted as a function of distance in Fig. 5.7. The optimal conversion of the pump energy

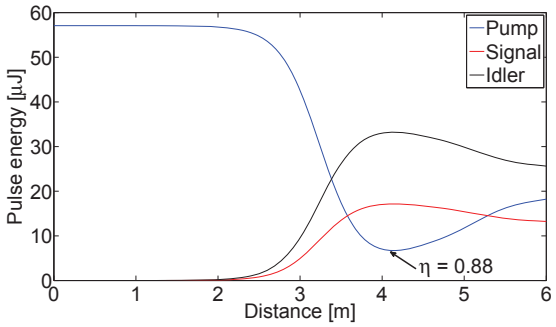

Figure 5.7: Pulse energy as a function of propagation distance.

occurs at a distance of 4.15 m. The pump photon efficiency, η, is at this length found at $\eta = 0.88$. The remaining pump energy is located at the rising and falling edges of the pulse. This is discussed further in Sec. 5.3.1.

5.2 Intermodal Case

The numerical simulations are presented for the intermodal case in this section. The idler and half of the pump energy are in the LP_{04} mode, while the other half of the pump energy and the signal are in the LP_{05} mode. The fiber is the custom designed fiber with an OD of 125 μm, i.e. the same as in the previous section. The PMCs along with the corresponding small signal gain spectrum are seen in

Fig. 5.8. Here, the pump wavelength is $\lambda_p = 1045.9$ nm, the initial pump power of each pump is 10 kW and the propagation length is 1 m. The figure shows that the analytical approximation, indicated by the horizontal dashed lines in the top plot, is in excellent agreement with the simulated gain spectra shown in the bottom plot. As for the monomode case an octave spanning wavelength

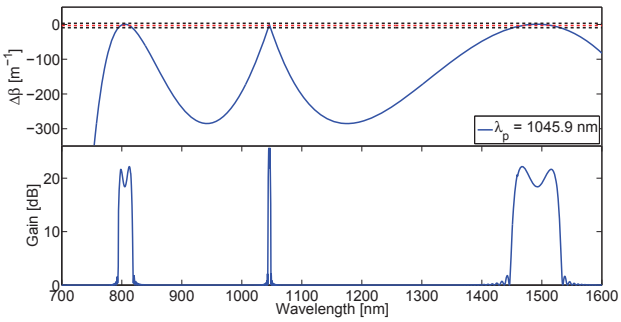

Figure 5.8: The top plot show the PMC. The dashed lines indicate the analytical approximation for the maximum gain and gain boundaries. The plot below is the corresponding small signal gain spectrum.

conversion is achieved. However, in the intermodal case the gain bandwidth for the signal is approximately 80 nm from 1450 to 1530 nm, and for the idler the wavelength range is from 795 to 820 nm. Therefore, this scheme enables seeding of the FWM process with a widely available tunable laser at telecommunication wavelengths, and thereby obtaining a tunable laser at approximately 800 nm.

The pump power is shown as a function of fiber length for a range of different signal wavelengths equally spaced between 1440 and 1540 nm in Fig. 5.9(a). The optimal conversion length and maximum pump photon conversion as a function of signal wavelength are shown in Fig. 5.9(b). These simulations are carried out in the CW scheme, thus Eq. (2.1.7) are solved when all dispersion terms are neglected. For these simulations, the same parameters were used for modes, pump wavelength, and pump powers as stated above. The maximum conversion is obtained at a length of 3.7 m, for a signal wavelength of $\lambda_s = 1492$ nm. As seen in the figure, near full conversion is feasible for the intermodal case. This depends on the relative overlap integrals between the different modes, i.e. the overlap integral for the SPM, XPM, and FWM terms. A sufficient magnitude for the overlap integral for the FWM term is obtained by choosing the modes in pairs. This is likely to yield a larger overlap integral as opposed to choosing four entirely different modes. There are however exceptions if operating in regimes where the modes are highly dispersive, for instance due to avoided mode crossings [76]. The impact of the ratio of the overlap integrals is discussed further in Sec. 5.3.3.

The pulse propagation simulations Eq. (2.1.7) are solved numerically using

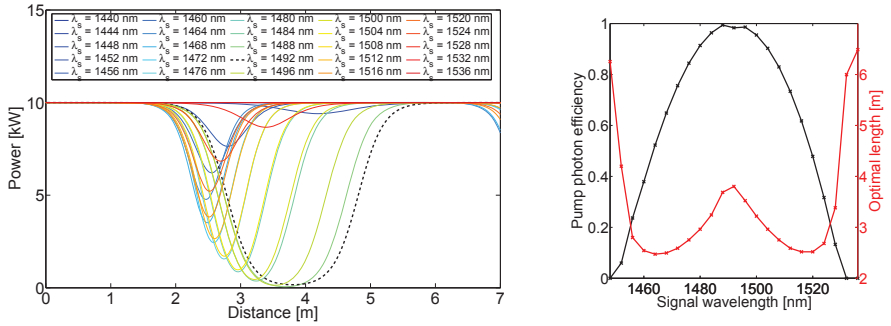

(a) (b)

Figure 5.9: (a) Pump conversion as a function of fiber length for different signal wavelengths. (b) The optimal length and maximum pump photon conversion as a function of signal wavelength.

the split step Fourier method [7, 75]. The pulse evolution in the time domain, as a function of propagation distance, is seen in Fig. 5.10 for the intermodal case. The time axis on all figures is a retarded time frame that moves with the group velocity of the idler pulse. The modes and initial pump powers are

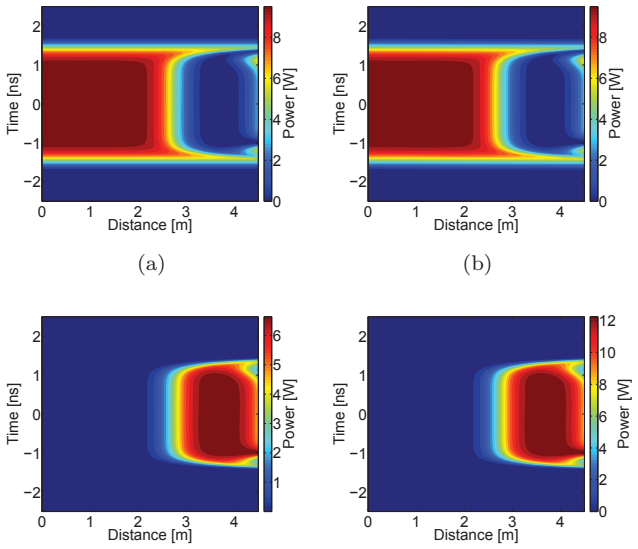

(a) (b)

(c) (d)

Figure 5.10: Pulse propagation as a function of distance in a retarded time frame. (a) Pump in LP_{04} mode at 1045.9 nm. (b) Pump in LP_{05} mode at 1045.9 nm. (c) Signal at 1488 nm. (d) Idler at 806.3 nm.

chosen as above. The signal wavelength is $\lambda_s = 1488$ nm, and the pulse shape is a super Gaussian of 10th order with a Gaussian width of 3 ns. The length of propagation in the fundamental mode is 20 cm. From Fig. 5.10 it is again seen that dispersion effect and temporal walk off only play a minor role on pulse shaping, although dispersion effects cause the slight asymmetries of the pulses. The walk off is largest between the pump in the LP_{04} mode and the idler. In this case a 3 ns walk off requires a propagation length of 121 m.

To evaluate the maximum conversion distance the pulse energies are plotted as a function of distance in Fig. 5.11. At the maximum conversion distance of 3.78 m the pump photon conversion efficiency is $\eta = 0.89$. All the results for the intermodal case are similar to the monomode case. An important observation is that full conversion is still achievable even though different modes are used.

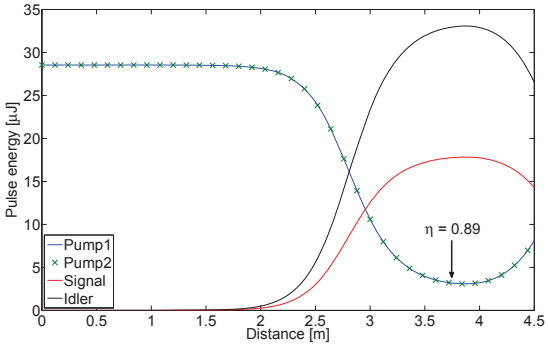

Figure 5.11: Pulse energy as a function of propagation distance.

5.3 Impact on the Four Wave Mixing Process

In this section it is investigated how the pulse shape, SPM in the initial length before the grating, and the overlap integrals impact the FWM process.

5.3.1 Impact of Pulse Shape

As seen in Figs. 5.5 and 5.9, almost full conversion was possible when all waves were CW. In the pulsed simulations, the maximum pump photon conversion efficiency was limited to approximately 0.87-0.88. This is related to the pulseshape of the pump pulses. Consider a regime where temporal walkoff and dispersion effects are almost negligible, the full conversion length is inversely related to the pump power, hence the peak is converted before the leading and trailing edges. This is illustrated in Fig. 5.12(a) using the simulation shown in Fig. 5.10 as an example, where the pulseshape is a super Gaussian of 10^{th}

order. This means the pump pulse is given by

$$P_p(t) = P_0 \exp(t/t_0)^{\mathrm{SGO}}, \tag{5.3.1}$$

where P_0 is the initial peak pump power, t_0 is the pulse width, and SGO is the super Gaussian mode order. The figure shows the pump pulse at the initial length, and at the length of maximum conversion. The generated idler pulse is also shown at the maximum conversion length. The pump photon efficiency is

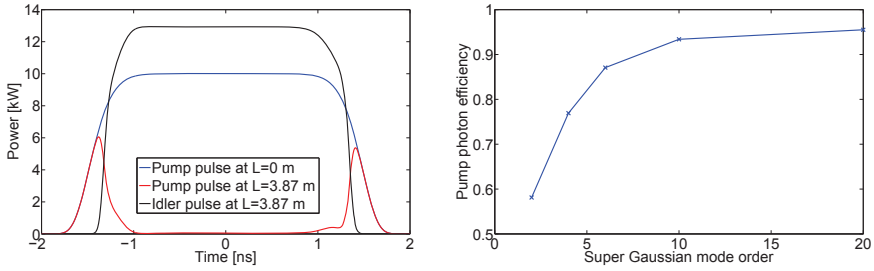

(a) (b)

Figure 5.12: (a) Example of 10^{th} order super Gaussian pump pulse. The initial pump pulse and the pump pulse at optimal conversion are plotted, along with the generated idler pulse. (b) Pump photon efficiency as a function of super Gaussian mode order.

defined as the fraction of converted pump photons. In Fig. 5.12(b) the pump photon efficiency is plotted as a function of super Gaussian mode order. The efficiency increases as the pump pulse tends towards a square pulse. In all simulations presented in this chapter an initial super Gaussian pump pulse of 10^{th} order was used. This choice is based on two considerations. First, as seen from Fig. 5.12 the pump efficiency is not increased significantly for Gaussian orders higher than 10^{th} order. Second, it is experimentally realistic to obtain this pulse shape with an 8 GSa/s arbitrary waveform generator (AWG), which is used for the pump laser. The laser was described further in App. A.

5.3.2 Impact of SPM of Pump in the Fundamental Mode

In any experiment, a certain length of fiber before the grating is required since it allows for practical handling of the device during an experiment. As mentioned in Sec. 5.1, an initial length of 20 cm was included in the pulse simulations to account for the initial SPM in the fundamental mode, before the light reaches the LPG and is converted to a HOM; this length is referred to as the initial SPM length. The impact of this is investigated further by performing pulse propagation simulations in the intermodal case using different initial SPM lengths. All the remaining simulation parameters are the same as

those used in Sec. 5.2. In Fig. 5.13 the pump photon efficiency is plotted as a function of initial SPM length. As expected, the pump photon conversion efficiency decreases as the initial SPM length is increased. This is the reason

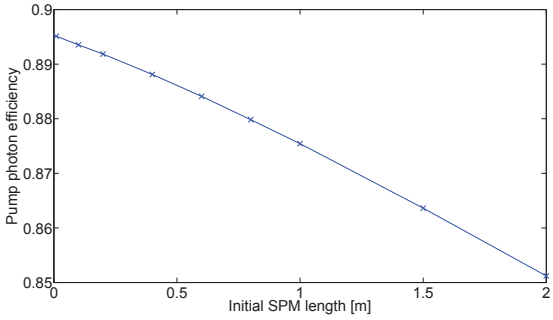

Figure 5.13: Pump photon efficiency as a function of initial SPM length, where the pump field is propagating in the fundamental mode.

why one of the design criteria for the fiber was to maximize the effective area of the fundamental mode, since this reduces SPM and thereby minimizes the decrease of the pump photon conversion efficiency.

5.3.3 Impact of Overlap Integrals

The magnitude of the overlap integrals for the FWM terms, in Eqs. (2.1.7) and (2.1.16) determines the strength of the FWM process, and therefore the coupling length. However, the FWM process is also affected by the other overlap integrals, such as the SPM and XPM terms. This is here illustrated using CW simulations. To limit the parameter space it is assumed that all SPM and XPM overlap integrals are equal to each other. These overlap integrals are then altered relatively to the overlap integral of the FWM term, so the adjustable simulation parameter becomes the ratio $f_{\mathrm{FWM}}/f_{\mathrm{SPM,XPM}}$, where $f_{\mathrm{SPM,XPM}}$ is the value of all the SPM and XPM overlap integrals. It is investigated how this ratio influences the pump photon conversion efficiency. This is carried out for both the monomode and intermodal case. The linear phase mismatch, $\Delta\beta$, from Secs. 5.1 and 5.2 were used. For each simulation the signal wavelength of maximum pump photon conversion efficiency was determined. The change in signal wavelength is tens of nanometers, and is caused by the change in the nonlinear phase mismatch introduced by SPM and XPM. The results of these simulations are presented in Fig. 5.14. In Fig. 5.14(a) it is seen how the pump photon conversion efficiencies decrease once the ratio of the overlap integrals is below a certain threshold. Even though this threshold differs, the tendency is the same for both the monomode and intermodal case. The reason behind this is when the SPM and XPM terms dominate, rapid phase modulation occur.

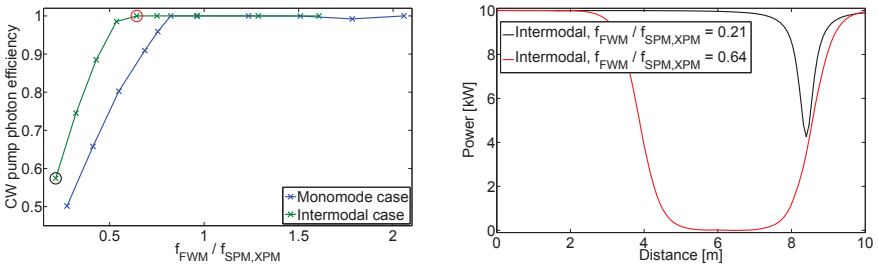

(a) (b)

Figure 5.14: (a) Pump photon conversion efficiency as a function of overlap integral ratio for both the monomode and intermodal case. The black and red circles are two illustrative examples that are shown in Fig. 5.14(b) (b) Pump power as a function of propagation distance of the intermodal case for two different overlap integral ratios.

This impacts the FWM process, since it depends on the relative phase relation between the four waves. The energy conversion between the interacting waves changes so rapidly that the effect averages to zero, rather than leading to an energy transfer between the fields. The absolute value of the FWM overlap integral determines the required conversion length. However, the pump photon efficiency only depends on the ratio between the overlap integrals; this is due to scalability of the governing equations, shown in Eqs. (2.1.7) and (2.1.16). In Fig. 5.14(b) two examples are shown for the intermodal case, which are marked with the corresponding colored circles in Fig. 5.14(a). For a ratio of 0.64 almost full conversion is achieved, whereas for a ratio of 0.21 only slightly more than half of the initial pump power is converted. The entire simulation ensemble showed that the length over which maximum conversion occurs increase along with increasing conversion efficiency; this is indicated by the two examples shown in Fig. 5.14(b). Also it was seen that the length for maximum pump conversion varied depending on the ratio.

These simulations are carried out to illustrate the impact of the overlap integrals on the FWM process. The simulations were simplified to decrease the parameter space since all the overlap integrals are likely to differ in reality. For each fiber design and selected mode combination, full numerical simulations must be carried out to ensure full pump conversion. From all the fiber designs and simulations carried out during this PhD project, a general rule of thumb was to ensure that all the overlap integrals are of the same order, $f_{\mathrm{FWM}} \approx f_{\mathrm{SPM}} \approx f_{\mathrm{XPM}}$. For the monomode case this is mostly automatically fulfilled since, as shown in Fig. 5.3(b), the field distribution is almost independent of the wavelength due to the strong HOM confinement. For the intermodal case this becomes slightly more complicated since the FWM overlap integral is almost inherently smaller than the overlap integral for the SPM terms, therefore the ratio between the overlap integrals is rarely larger than one. However, ratios

close to one were obtained by picking the modes in pairs, as was done for the intermodal cases, i.e. two fields in LP_{04} and two fields in LP_{05}. To verify this the overlap integral ratios, $f_{\mathrm{FWM}}/f_{\mathrm{SPM,XPM}}$, for the monomode and intermodal cases from Secs. 5.1 and 5.2 are shown in Tables 5.1 and 5.2, respectively. Here $f_{ab} = f_{aabb}$, where a and b are either p, q, s and i, which indicate the pumps, signal and idler, respectively. As expected, the overlap integral ratios for the

SPM			XPM		
r_{pp}	r_{ss}	r_{ii}	r_{ps}	r_{pi}	r_{si}
0.95	0.96	0.90	0.99	0.95	1.03

Table 5.1: Overlap integral ratios, $r_{ab} = f_{ppsi}/f_{ab}$, for the monomode case.

SPM				XPM					
r_{pp}	r_{qq}	r_{ss}	r_{ii}	r_{pq}	r_{ps}	r_{pi}	r_{qs}	r_{qi}	r_{si}
0.65	0.84	0.73	0.96	0.92	0.80	0.86	0.81	1.09	0.98

Table 5.2: Overlap integral ratios, $r_{ab} = f_{pqsi}/f_{ab}$, for the intermodal case.

monomode case are all close to one. The overlap integrals for the intermodal case are also in general acceptably close to one.

5.4 Fiber Fluctuations

One of the limitations for FWM processes is longitudinal variations of the index profile along the fiber [77–80]. During this PhD project the impact of group velocity dispersion (GVD) fluctuations have been investigated experimentally and numerically in HNLFs [81]. The cause of these variations is typically contributed to OD fluctuations and changes in the index profile along the fiber [82, 83]. In the following simulations, the origin of the variation is not crucial since both effects simplify to a change in the linear phase mismatch along the fiber. To minimize the parameter space it is assumed that the variation is only caused by OD fluctuations.

The length scale of these variations is believed to be on the order of a few meters to tens of meters, depending on the draw speed during fabrication of the fiber [82,83]. If the fiber length is significantly longer than this length scale, then the impact is often modeled using a stochastic approach [77,81]. According to the simulations presented in Secs. 5.1 and 5.2, the FWM conversion length is only a few meters, hence in this case, the variations are modeled as a linear change in OD along the fiber. It was verified numerically that a linear change in OD with excellent agreement corresponds to a linear change in the linear phase mismatch, $\Delta\beta$, along the fiber; this is not shown here.

To estimate the magnitude of the OD variations in the custom designed fiber, the LPG characterization presented in Sec. 4.4 is considered. It was observed that, for a given grating pitch, the resonance wavelengths appeared over a wavelength range of approximately 40 nm for both the LP_{06} and LP_{07} modes. Assuming that the fabrication process is entirely reproduceable, it is found that this corresponds to an OD variation of ± 0.7 %. The pieces of fiber for the gratings are taken from a spool over hundreds of meters, therefore it is expected that the variations are significantly smaller over the few meters required for the FWM experiment. It is noted that, by applying mature production processes used for transmission fibers, to the fabrication of HNLFs, it is possible to obtain OD variations as low as ± 0.03 % over 3 km of fiber [84]. Recently, HNLF designs have also been presented where the ZDW is robust, in spite of OD fluctuations along the fiber [85].

The sensitivity of the PMCs is illustrated in Fig. 5.15 for both the monomode and intermodal cases. The PMCs for three different ODs are plotted as a function of wavelengths; the dashed lines indicate the analytical approximation of the gain region. The three different ODs are the ideal 125 μm, along with ± 0.5 % of this OD. The PMCs and thereby the gain regions experience sig-

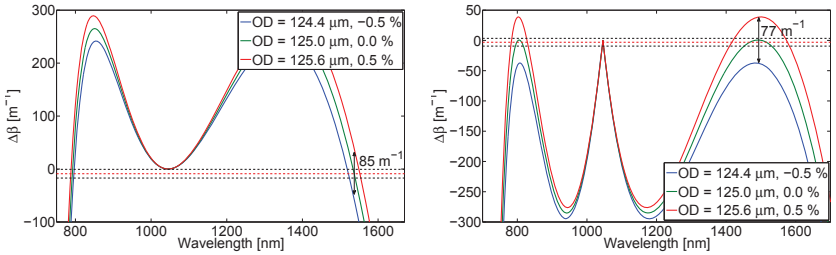

Figure 5.15: (a) PMCs for different fiber ODs for the monomode case. (b) PMCs for different fiber ODs for the intermodal case.

nificant changes for these OD variations. As shown on the figure, the linear phase mismatch, $\Delta\beta$, is changed by 85 and 77 m^{-1} in the gain regions, for the monomode and intermodal case respectively. This indicates that the intermodal case is only slightly less impacted by the OD variations. The fact that the gain region is wider for the intermodal case does not make it more robust against OD variations. This would only be the case if the OD variations lead to horizontal translations of the PMCs, since in this case the value of the linear phase mismatch would remain almost the same for a given wavelength in the gain region. These arguments are based on simplified approximations, however the full numerical simulations are presented below.

In the simulations, small signal gain spectra are calculated based on CW simulations, therefore all dispersion terms are neglected. However, as seen in Sec. 5.3.1, the dispersion effects only have minor impact on pulse shaping, which

means the conclusions are directly applicable to the pulsed case as well. As previously mentioned, the OD of the fiber is assumed to change linearly along the fiber, which is equivalent to a linear change in the linear phase mismatch along the fiber. The conventions are established in Fig. 5.16. The OD of the

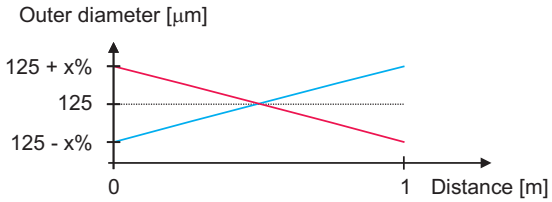

Figure 5.16: Change in the OD along a 1 m length of fiber. Two different types of linear change are depicted.

fiber is either changed from -x % to x % (blue line), which is referred to as x %, or the opposite direction from x % to -x % (red line), which is referred to as -x %. At the mid-point of the fiber segment, the OD of the fiber takes on the ideal value of 125 μm. The overlap integrals, from Eqs. (2.1.7) and (2.1.16), are assumed constant i.e. independent of the OD, and are calculated from the fields of the ideal fiber OD.

In Fig. 5.17 the monomode case is presented, since the gain spectrum is symmetric only a close up of the signal gain region is displayed. For a variation of ±0.5 %, the gain spectra are significantly reduced. In Fig. 5.18 the inter-

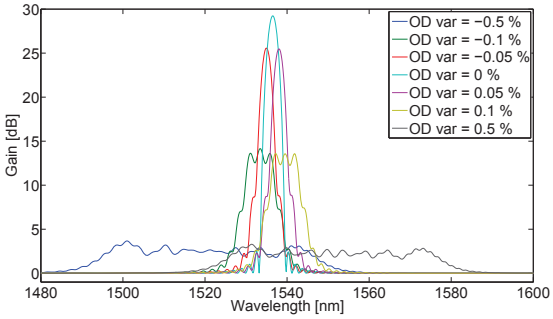

Figure 5.17: Small signal gain spectra for different OD variations for the monomode case.

modal case is presented. Again, a variation of ±0.5 % leads to a significant reduction in the gain spectra. By comparing the monomode and intermodal case it was discovered that, as predicted, the OD variation has almost the same effect on the gain spectra. However, for the intermodal case the reduction in gain is approximately 5 dB less than for the monomode case for OD variations

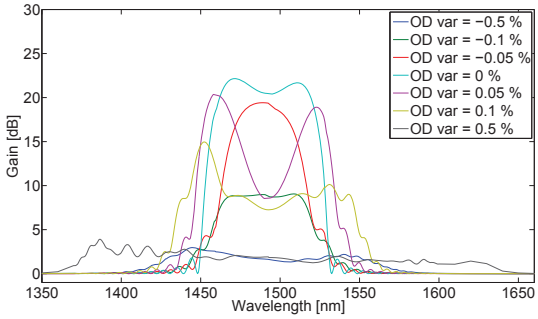

Figure 5.18: Small signal gain spectra for different OD variations for the intermodal case.

of ±0.05 % and ±0.1 %. It is possible that higher gain is achieved in the intermodal case by choosing an appropriate pump wavelength, although this has not been examined further.

It is concluded that, if the OD variations are as critical as the LPG fabrication indicated, this could pose a serious threat to the success of the FWM experiments, which the fiber was designed for. However, since only few meters with relative constant OD is required, it is expected that this may exist on the spool of the fabricated fiber. This may translate to a low yield since every single device may not perform as expected.

5.5 Dielectric Breakdown

The ultimate limitation of power levels is dielectric breakdown. This occurs when the electric field is strong enough to break the molecular bonds in the material. The advantage of using HOM is that stable propagation is possible in much larger effective area modes compared to large mode area (LMA) fibers that only guide the fundamental mode. This was discussed in Sec. 2.2. To carry out a comparison, modulation instability (MI) around the pump in the 1 μm regime is considered. In this situation, the requirement for phase matching translates to a need for slight anomalous dispersion, i.e. the ZDW must occur in this particular wavelength range.

For the custom designed fiber with an OD of 125 μm, anomalous dispersion is ensured by pumping in the LP_{07} mode since this mode has a zero dispersion wavelength of $\lambda_{ZDW} = 1028.1$ nm, as shown in Fig. 5.2(a). The effective area of the LP_{07} mode is $A_{eff} = 573\ \mu m^2$, as demonstrated in Fig. 5.3(b). For PCFs this ZDW is realized by obtaining anomalous waveguide dispersion to compensate for the normal material dispersion. Inherently, this requires small diameter cores, which in turn limits the allowed power levels before the onset of dielectric breakdown. For this comparison, a PCF design found in

the literature is considered [86]. This fiber has a zero dispersion wavelength of $\lambda_{\mathrm{ZDW}} = 1038$ nm, and an effective area of $A_{\mathrm{eff}} = 11.5\ \mu\mathrm{m}^2$. The effective area is calculated using finite element method (FEM) simulations in COMSOL based on the structure presented in [86].

Even though the ratio between the effective areas is approximately 50, this does not mean a 50-times increase in power is possible. Since, when different modes are compared, it is not just a matter of the ratio between the effective areas. Instead the dielectric breakdown intensity threshold depends on peak intensity [10, 87]. Even though the effective area is large for HOMs, the local intensity is also high. This is illustrated in Fig. 5.19, where the fundamental mode for the PCF is plotted along with the modes of interest for the custom designed fiber. In Fig. 5.19 all the modes are normalized to have a total power

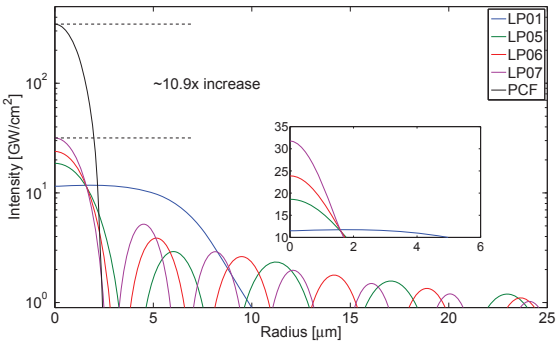

Figure 5.19: Intensity as a function of radial distance. The LP_{0x} modes are for the custom designed fiber, whereas the line labeled "PCF" is for the fundamental mode of the PCF from the paper [86].

of 20 kW. The peak intensity generally increases with mode order. For this specific example, the peak power of the fundamental mode in the PCF is 10.9 times higher than the LP_{07} mode. Consequently, the possible increase in power before dielectric breakdown occurs in the respective fibers is equal to this ratio. The fundamental mode of the custom designed fiber is also shown. It is seen that the peak intensity for this mode is lower than for the HOMs, even though it is core guided. This means that dielectric breakdown is not an issue in the initial length before the mode is converted at the grating. This was ensured through the design criteria of maximizing the effective area of the fundamental mode.

Based on empirical evidence it has been found that the intensity breakdown limit is approximately given by [10, 87]

$$I_{\text{Breakdown}} \approx \frac{300 \text{ GW/cm}^2}{\sqrt{\tau(\text{ns})}}, \tag{5.5.1}$$

where τ is the pulse width in nanoseconds. This means that for a pulse width of 3 ns, which is relevant for this PhD project, the LP_{07} mode is in the considered fiber able to carry 109 kW of integrated power before dielectric breakdown occurs. It is noted that this is based on empirical data and results may vary since the intensity threshold may depend on other things, such as doping concentrations.

5.5.1 Energy Scalability

Another attractive feature of FWM using HOMs is power/energy scalability [56, 88]. This entails changing the fiber design and the selected mode order combinations, in such a way that similar phase matching curves (PMCs) are obtained, while simultaneously enabling higher power handling capabilities before dielectric breakdown occur. It was previously discussed in Sec. 3.4 that by scaling the fiber design, different mode order combinations of $xxyy$ obtained similar PMCs. This notation refers to that the idler and pump1 is in LP_{0x}, while pump2 and signal is in LP_{0y}, and $y = x + 1$. Below, a slightly different approach is used. Instead of scaling the entire fiber, only the inner cladding radius, r_2, is altered, while the core radius remains the same. This is preferred since the core then remains single moded regardless of the design alteration. The PMCs for the five different designs are seen in Fig. 5.20(a). Even though the signal wavelengths vary the general trend of the curves are the same. For the 3344, 4455, 5566, 6677, and 7788 mode combinations, the inner radius is 18.1, 22.9, 27.8, 32.6, and 37.4 μm, respectively.

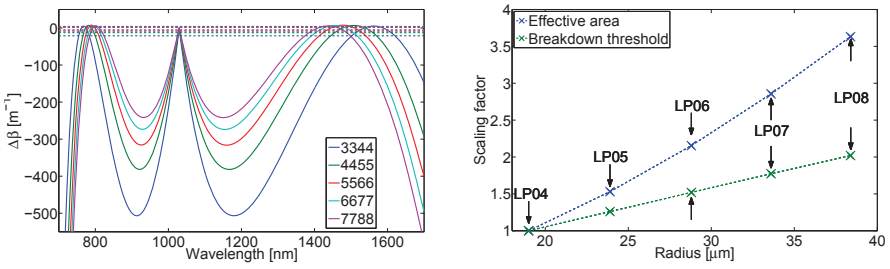

(a) (b)

Figure 5.20: (a) Five different fiber designs, which yield similar kind of PMCs. (b) Effective area and breakdown threshold relative to the 3344 mode combination for the five different designs.

Regarding power/energy scalability a trade off occurs. On one hand, increasing the mode order combination means that the inner radius is increased, thus the effective mode area increases, and this increases the allowed power levels. On the other hand, the increase in mode combination also increases the mode order, which leads to higher peak intensities, and thus lowers the allowed power levels. For a given mode combination, $xxyy$, the limiting mode is the higher of the two, i.e. the LP_{0y} mode, since this has the highest peak intensity. In Fig. 5.20(b) the effective area of the LP_{0y} modes are plotted normalized to the effective area of the LP_{04} mode from the 3344 mode combination. The effective area is seen to increase with mode order combination, or r_2, as stated in the first part of the trade-off. Also, the breakdown thresholds for the five different fiber designs are plotted using the same mode as normalization. Even though the breakdown threshold is not increasing as quickly as the effective area, it still increases with increasing mode order combination.

It is concluded that using HOMs power/energy scalability is possible. Since by increasing the fiber dimensions and choosing the modes accordingly, it is possible to obtain similar PMCs for modes with lower peak intensities [56, 88]. Also, it was demonstrated in [56], that this new HOM FWM platform enables conversion of pulse energies exceeding mJ levels, hereby realizing high-power lasers at wavelengths where efficient gain dopants are unavailable.

5.6 Summary

Two different phase matching schemes were demonstrated using the custom designed fiber with a fiber diameter of 125 nm. In both schemes, phase matching was obtained between a pump at approximately 1045 nm and a signal at telecommunication wavelengths, thereby generating an idler at approximately 800 nm. For the monomode case, all interacting fields were in the LP_{06} mode, and the gain region was a few nanometers on the idler side. For the intermodal scheme, the idler and half of the pump power were in the LP_{04} mode, while the other half of the pump power and the signal were in the LP_{05} mode. In this scheme the width of the idler gain region is approximately 25 nm. In the pulse propagation simulations, it was for both schemes demonstrated that, using a 10^{th} order super Gaussian pump pulse, approximately 88 % of the pump was converted after a few meters of propagation. In the following section the impact of the pulse shape was investigated, it was found that a super Gaussian pulse of 10^{th} order provided a satisfactory pump conversion. The impact of SPM occurring before the grating on the conversion efficiency was also investigated. It was found that a length of 20 cm was acceptable. Next, the impact of the ratio between the overlap integrals was examined. Here it was found as a general rule of thumb that the ratio $f_{\text{FWM}}/f_{\text{SPM/XPM}}$ should be as close to one as possible. In the following section, the impact of fiber OD variations was investigated. It was found that OD variations indicated by the grating fabrication of ± 0.7 % would have a significant impact on the gain spectrum of both phase matching

schemes. Finally, it was demonstrated that it is possible to generate MI in the 1 μm regime, at 12 times higher power levels when using HOM compared to PCFs with similar anomalous dispersion characteristic. Furthermore, it was shown that using HOMs power/energy scalability is possible.

6

Experiments for Higher Order Mode Four Wave Mixing

In this chapter the experimental work involving four-wave mixing (FWM) using higher order modes (HOMs) is presented. The first section briefly explains the experimental setup. This is followed by a discussion of different aspects related to the equipment, which is found to have relevance for experiments. The third section presents the experiments where the pump is in the LP_{06} mode. The last section presents experiments where the pump is in the LP_{07} mode.

6.1 Experimental Setup

The setup used for the HOM FWM experiments is displayed in Fig. 6.1. The

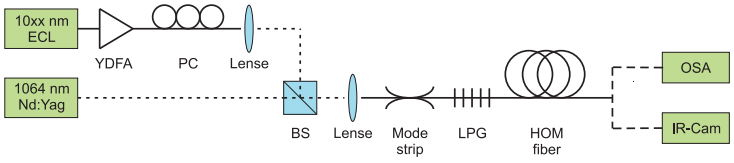

Figure 6.1: Sketch of the HOM FWM setup.

signal external cavity laser (ECL) is a continuous wave (CW) tunable laser kit from Thorlabs (TLK-L1050M). It has a tunable wavelength range from 1010 to 1080 nm and a maximum output power of 7-8 mW. Following the ECL is a dual stage ytterbium doped fiber amplifier (YDFA), which amplifies the power to 20-25 mW. A fiber based polarization controller (PC) is placed

before the signal is coupled into free space. The pump laser is a high powered Q-switched Nd:YAG laser from Continuum (Minilite ML-II). The wavelength is fixed at $\lambda_p = 1064$ nm, the pulse width is specified to 5-7 ns, and the repetition rate is 15 Hz. The maximum pulse energy is specified to 50 mJ, and therefore the maximum peak power is approximately 8 MW. The two wavelengths are combined using a 50/50 beam splitter (BS) and subsequently coupled into the custom designed fiber with an outer diameter (OD) of 130 μm. In the fiber, a mode strip is fabricated consisting of a tapered etched region, as described in Sec. 4.6. Afterwards, the fundamental mode is converted using the long period grating (LPG) to the LP_{06} or LP_{07} mode. Once the FWM process has occurred in the remaining part of the fiber, the result is analyzed by measuring the spectrum using either an optical spectrum analyzer (OSA) or a spectrometer. The light was coupled into the spectrometers using a multi moded (MM) pigtail, either by splicing it directly to the custom designed fiber or by collimating the beam and focusing it into the MM pigtail. Alternatively, the output is filtered before the mode is imaged using an infrared (IR)-Cam.

6.2 Characterization of the Components

This section present some of the initial considerations that prove important for the FWM experiments. It includes a discussion of the different modes of operation of the OSA, characterization of the power detectors, clarification of spurious peaks. In regard to the pump source, spectral and temporal characterizations are performed, and comments on coupling into the fiber and maximum power levels are mentioned.

6.2.1 Operation of Optical Spectrum Analyzer

The repetition rate of the pump laser is only 15 Hz, which means that the average power is too low to measure with the OSA using CW mode. Instead either the "peak hold" mode or the external trigger mode are used.

In the "peak hold" mode the OSA estimates the peak power over a user defined time window, which must be set larger than the repetition rate. The exact algorithm behind this estimation is not described in the manual of the OSA. However, as shown in Sec. 6.2.2 the detector response is not linear in the "peak hold" mode, so this mode is rarely used, hence investigating the algorithm was not pursued further. In the external trigger mode the OSA is triggered by the Q-switch signal from the pump source. The OSA waits for the trigger, once received, it measures average power over a time window. On newer versions of the OSA it is possible to set this time window between 50 μs and 200 ms. However, on the older version used for these experiments the time window is fixed. Yokogawa was not able to inform us of the size of this time window, except that it is larger than 50 μs. Furthermore, based on measurements it was realized that the OSA does not provide average power

measurements, therefore the time window must be smaller than the inverse repetition rate of 66.6 ms.

For the seeded experiments a CW signal was used, therefore it was examined how the OSA in the external trigger mode measures a CW signal. As expected, the same spectrum was obtained as when it was measured using the CW mode. The only difference is the noise floor is about 20 dB higher with the external trigger mode; the spectra showing this are included in App. E in Fig. E.1.

6.2.2 Characterization of Power Detectors

In this section, power measurements using different detectors are compared with respect to linearity. The detectors being compared are the OSA (using both the "peak hold" mode and the external trigger mode), a silicon power meter, an Avantes spectrometer, and a pyroelectric detector. A sketch of the setup is seen in Fig. 6.2. For the experiments, the pump laser is focused on

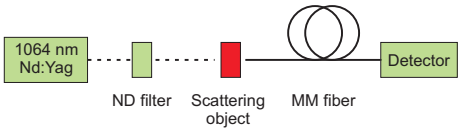

Figure 6.2: Sketch of the setup to characterize the ND filters.

a scattering object, and the reflections are picked up using a MM fiber. For the pyroelectric detector, the pump laser was sent directly into the detector. In all cases, measurements were performed at different attenuation levels using neutral density (ND) filters. The results of the measurements are summarized in Fig. 6.3. The silicon power meter, the Avantes spectrometer, and the py-

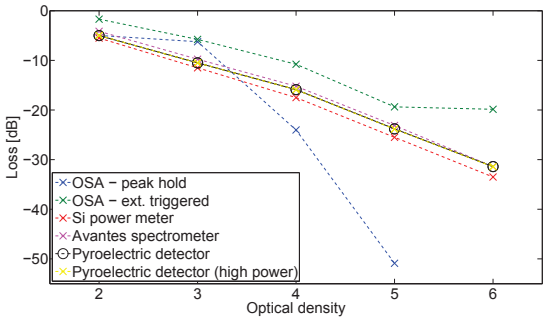

Figure 6.3: Loss measured using the pump laser as a function of optical density.

roelectric detector yielded similar results. Using the dielectric detector, it was examined whether the filter attenuation was power dependent, which turned

out not to be the case. For the black circles the pulse energy was 754 μJ, whereas in the high power case (yellow crosses) the pulse energy was 9.2 mJ. Notice that the loss does not correspond to the expected loss based on the optical density of the filters; no explanation for this was found. The OSA measurements were performed using two different settings. Using an external trigger, the loss is the same except for a constant offset. It is expected that the offset is caused by the detector being slightly saturated for the reference measurement without any filter. The data point for an optical density of 6 should be omitted since this is close to the noise floor. For the measurement using the "peak hold" mode, the behavior stands out from the other measurements, and quantitative measurements are not provided. It is expected that this is due to the pulse widths being too narrow for this mode of operation.

In the following, almost all measurements performed on the OSA use an external trigger. Unfortunately, before the above conclusions were realized, two cutback measurements were performed using "peak hold". Due to the nature of these measurements it was not possible to redo them.

6.2.3 Spurious Peaks on Optical Spectrum Analyzer

In the spectra measured with the OSA, several unexpected peaks occurred, especially a strong peak at 840 nm was observed. This was seen regardless of which fiber the pump laser was coupled into, i.e. GRIN fiber, large mode area (LMA)-fiber, the LP_{06} device, and the LP_{07} device. In order to examine the origin of these peaks further, the pump laser was free spaced coupled into the OSA; this means that the only components in the beampath are five dielectric mirrors and a beamsplitter. The spectra are presented in Fig. 6.4. First the blue line was measured, and then after repositioning the OSA, the red line was measured. Several unexpected peaks appear, most dominating are the peaks at 800 and 840 nm. Peaks also occurred at 1000, 1200, 1250, and 1600 nm. These however are dependent on the exact physical placement of the OSA, i.e. the incident angle of free space beam with respect to the OSA. For the green trace, a longpass filter with a cutoff of 1000 nm was placed in the beampath, which leads to approximately 2 dB decrease in power at all wavelengths. The black trace is unlike the previous traces measured using the peak hold function on the OSA; again strong peaks are seen around 800 and 840 nm. The spectrum was also measured for wavelengths below 1100 nm using a spectrometer and here no unexpected peaks were observed. According to Continuum there is absolutely no reason to believe that the laser is generating anything besides the 1064 nm line. Based on this and the measurements using the longpass filter, it is concluded that all peaks and the continuum background are spurious and caused by the OSA. Also it is noted that since then the same peaks were observed using a different high power 1064 nm source. The continuum background was only observed when the OSA was strongly saturated. However, in the following measurements some of the peaks are observed even when the OSA is not saturated at the pump wavelength. Finally, it is noted that the

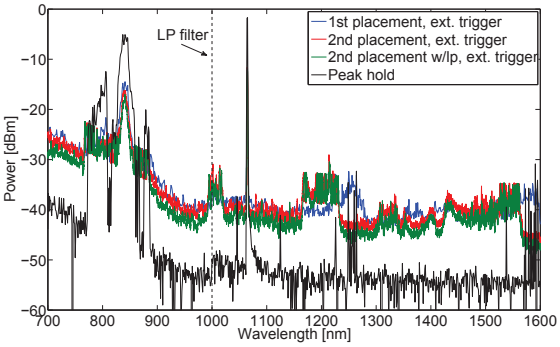

Figure 6.4: Spectra measuring the pump as it is free spaced coupled into the OSA.

OSA was performing as expected during other experiments.

6.2.4 Characterization of Pump Laser

The pump laser was measured spectrally using an OSA. For the experiments the peak power is approximately 10 kW, therefore attenuation is needed to avoid damaging the detector in the OSA. The resolution was set at $\Delta\lambda = 0.01$ nm and the spectra are seen in Fig. 6.5. The blue line is using the external

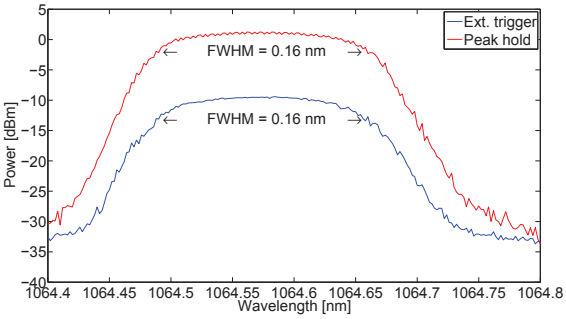

Figure 6.5: Spectra of the pump laser measured with an OSA using two different settings.

trigger mode and the red line is using the "peak hold" mode on the OSA. With both modes of operation, the full width half maximum (FWHM) is measured at 0.16 nm, the linewidth specified in the data sheet is 1 cm^{-1}, which corresponds to 0.11 nm.

The temporal width of the pump laser was measured in several ways. In Fig. 6.7(a) it is measured using a photodetector with a rise time of 1 ns and a

350 MHz scope. From this, it is found that the FWHM pulse width is 5 ns. In Fig. 6.7(b) the pulse is measured using a sampling scope with an Agilent 83485B module, which has an optical bandwidth of 30 GHz. The blue dots are using the Q-switch signal as trigger. The trace in the figure was averaged 16 times. Without averaging the recorded traces are much noisier. An example of this is presented in Fig. E.2 located in App. E. A Gaussian pulse was fitted to the data, and the FWHM of the fit was 5.2 ns. The red dots are measured using the

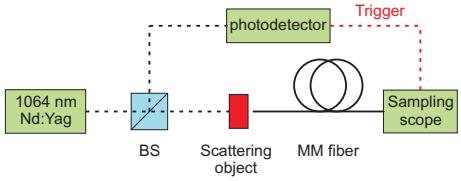

Figure 6.6: Setup used for measuring the pulse width using photodetector as trigger.

setup seen in Fig. 6.6. Here the pump was divided using a beam splitter (BS), a photodetector is placed in one of the beampaths, and the signal from the photodetector is used to trigger the sampling scope, which picks up light from a scattering object using a multi moded (MM) fiber. Once again, a Gaussian function was fitted to the data, yielding a pulse width of 4.8 ns. The difference in the pulse widths between the two different trigger methods, are attributed to timimg jitter between the Q-switch trigger signal and the actual pulses. In the data sheet the time jitter is stated as ±0.5 ns. It is expected that by triggering with the photodetector the time jitter was reduced.

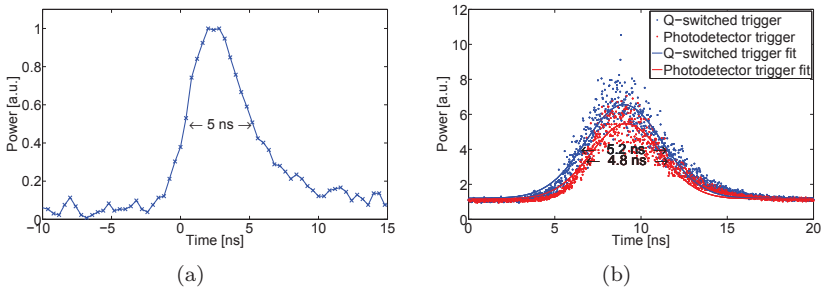

Figure 6.7: (a) Pulse width measured with photodetector and 350 MHz scope. (b) Pulse width measured using sampling scope with two different trigger mechanisms. Gaussian fits to the pulses are provided and the FWHM is stated in the plot.

It is concluded that the pulse width is about 5 ns. Given the spectral width the time-bandwidth product is found to be 706, hence the pulses are far from transform limited. Two different modes of operation were available on the

pump laser, a low and high energy mode. The above data were all measured in the high energy mode. The pulse widths were also measured in the low energy mode; it was observed that the pulse width increased to approximately 15 ns. Due to this, the laser was only operated in the high energy mode in the experiments presented in this chapter.

6.2.5 Coupling into the Fiber and Power Limitations

The Nd:YAG laser was lens coupled into the 130 μm OD custom designed fiber. The coupling efficiency was measured with the pyroelectric detector. The maximum obtainable and overall coupling efficiency was approximately 15-20 %. This includes both the in coupling loss and the attenuation through the mode strip. It is believed that the coupling efficiency is limited by the M^2-parameter of the pump source, which in two orthogonal directions were measured to be approximately 2.55 and 4.39. The beam quality was improved experimentally by spatial filtering in k-space. To illustrate the beam quality of the ND:YAG laser the mode is shown in Fig. 6.8. The images are reflections of the fiber end facet, which are then imaged through an aspheric lens. It is seen that the modes are far from Gaussian. A pyroelectric detector was used to

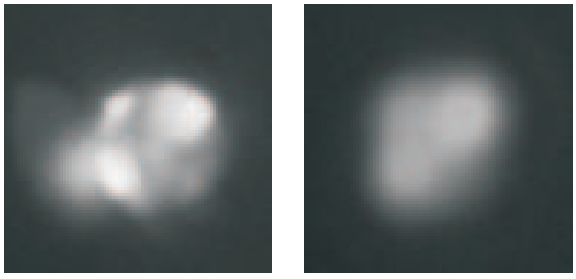

(a) (b)

Figure 6.8: Nd:YAG output mode. (a) No spacial filtering. (b) After spacial filtering.

measure the maximum peak variation over 500 pulses. Directly from the laser the variation was 20-30 %. Once coupled into the custom designed fiber the variation was as high as 50 %. The increase is attributed to dynamic changes of the beam profile, which leads to changes in the coupling efficiency.

In most experiments, the power level was pushed until the fiber end facet burned. This occurred at very different power levels, but generally it required pulse energies higher than around 50 μJ. Several times an entire piece of fiber of approximately 1-2 cm was torn off. One of these pieces was located on the optical bench. The end facet of the fiber appears intact, however approximately 1 cm from the end facet, the fiber was destroyed. Images of this are displayed in Fig. E.3 in App. E. On other occasions the fiber did not break, however a

small bend was introduced in the fiber a few centimeters from the end facet. This was accompanied by the otherwise clear coating of the fiber turning white and opaque; images of this are provided in Fig. E.4 in App. E. The exact cause of this type of upstream destruction of the fiber remains unclear. It seems unlikely that damages on the end facet are able to propagate through the fiber and cause the fiber to break upstream. It is speculated whether it is related to constructive interference between numerous cladding guided HOMs, which results in peak intensities higher than the dielectric breakdown of the fiber.

6.3 Experiments with Pump in LP_{06} Mode

The experiments where the pump is in the LP_{06} mode are presented in this section. The phase matching curve for the 130 μm OD fiber, where all fields are in the LP_{06} mode is presented in Fig. 6.9. The pump wavelength is set at

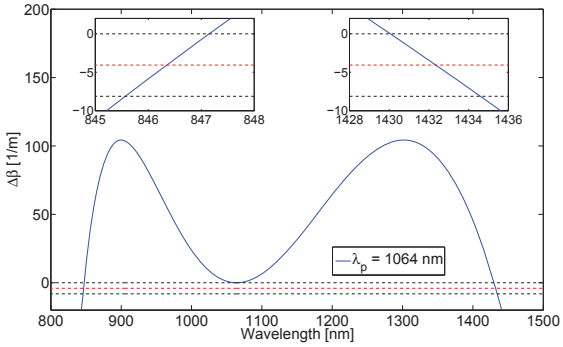

Figure 6.9: Phase matching curve when all fields are in LP_{06}.

$\lambda_p = 1064$ nm. For the analytical approximation of the gain region, the pump power was set at $P_p = 10$ kW. For the pulse width determined in Sec. 6.2.4 this corresponds to a pulse energy of approximately 50 μJ. As seen in the figure, the maximum small signal gain occurs at wavelengths of 846 and 1432 nm.

6.3.1 Different Pump Powers

The fiber device used for the experiment was the LP_{06}-A grating shown in Fig. 4.6. The transmission of the grating was measured at 9 dB, thus 87.4 % of the pump power is converted into the LP_{06} mode. The length of the fiber after the grating was 12 m. The experimental setup used was shown in Fig. 6.1, however in this specific experiment, no signal seed was used. The measured spectra for different pump powers are seen in Fig. 6.10. In Fig. 6.10(a) the spectra is measured on the OSA. There is a peak at 1115 nm, which fits with

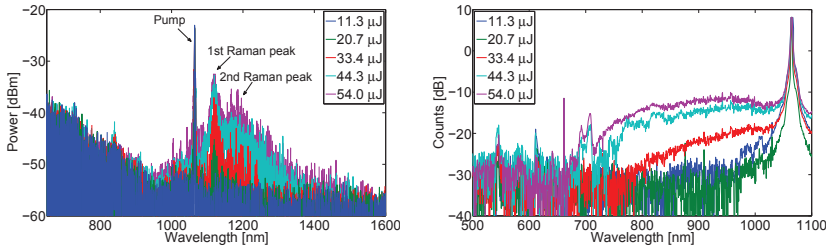

(a) (b)

Figure 6.10: Spectra measured at different power levels. (a) On the OSA. (b) On the Avantes spectrometer.

Raman scattering since it is 13 THz from the pump frequency. Furthermore, a second order cascaded Raman peak is observable. In Fig. 6.10(b) the same spectra are measured using a spectrometer. The spectrometer is uncalibrated with power. It measures "counts," which are proportional to the optical power. All spectra are plotted on a dB-scale. For higher pump powers a continuum at wavelengths shorter than the pump is generated. From the unsaturated spectra where a ND filter was used with an optical density of 2 (not shown here), the shorter wavelength continuum is 25 dB below the pump power. For the measurements on the OSA, this continuum is not observed since it is below the noise floor. It is expected that this short wavelength continuum is generated by FWM, where the Nd:YAG and the 1st order Raman gain peak acts as pumps. The phase matching curves for this process is illustrated in Fig. E.5 in App. E. No peaks are observed in either of the spectra at 846 or 1432 nm where spontaneous FWM is expected. In the spectra in Fig. 6.10(a), a peak is seen at 840 nm, however it is the spurious peak described in Sec. 6.2.3. In the spectra in Fig. 6.10(b), two peaks are seen around 700 nm. This seems too far from the theoretical value to be spontaneous FWM. In order to verify this experimentally the FWM process could be seeded by writing LPGs at either 700 nm or at the Stokes wavelength of 2216 nm. However, sources and detection equipment were not available at these wavelengths, therefore it was not pursued further. Another argument against it being spontaneous FWM is that multiple peaks occur at even shorter wavelengths. These peaks were also observed during other measurements, therefore it seems plausible that all these peaks are spurious and related to an artifact with the spectrometer. The cause of the artifact is unknown, but it could be room light or blooming in the detector. In order to observe spontaneous FWM it was attempted to suppress Raman scattering. This was done by cooling the fiber with liquid nitrogen, because this depopulates the phonon density [89–91]. These measurements are presented in Sec. 6.3.2. Another approach, which has not yet been attempted, is to write gratings on the Stokes side at different wavelengths near the expected phase matched wavelength of 1432 nm. Hereby, it would be possible to seed

the FWM process and potentially observe parametric amplification above the Raman level.

6.3.2 Cooling of Four Wave Mixing Fiber

In an attempt to suppress the Raman scattering, the fiber was cooled using liquid nitrogen [89–91]. In Fig. 6.11 the cooled spectra are plotted along with the uncooled spectrum at the highest pulse energy from Fig. 6.10. In Fig. 6.11(a) the spectra are measured using the OSA. At the first Raman gain peak at 1115 nm the power levels remain the same within 1 dB for all three measurements, and for longer wavelengths the power levels are slightly higher for the two cooled fibers. One noteworthy feature is that at the two highest pulse energies, new peaks appear at a wavelength of 1089 nm. It is expected that this is due to a FWM process where the two photons at 1064 and 1115 nm are annihilated and two photons at 1089 nm are created. Besides from obeying energy conservation, the process is also phase matched since the zero dispersion wavelength for the LP_{06} mode is at $\lambda_{ZDW} = 1081.2$ nm and thus 1089 nm is in the anomalous dispersion regime. The phase matching condition is illustrated in Fig. E.6 in App. E. In Fig. 6.11(b) the spectra measured from the spectrom-

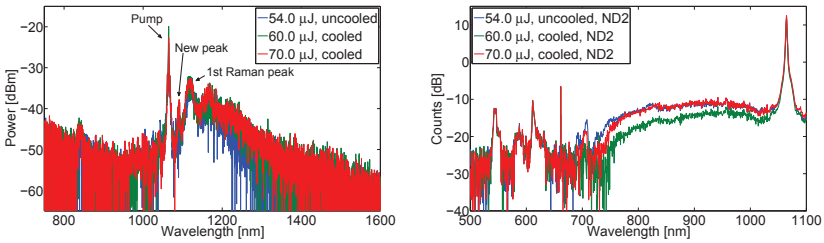

(a) (b)

Figure 6.11: Spectra measured at different power levels while the fiber was cooled with liquid nitrogen. (a) On the OSA. (b) On the Avantes spectrometer.

eter is shown. It is seen that the short wavelength continuum for the spectra of the cooled fiber is low compared to the 54 μJ uncooled spectrum. This could potentially be explained by that the short wavelength continuum is indirectly generated from the Raman scattering on the Stokes side, as described in Sec. 6.3.1. Any decrease in the Raman gain would thus lead to a decrease in the power of the short wavelength continuum. However, as in Fig. 6.11(a), there is no indication that the Raman gain has decreased as a result of the cooling. Instead it is speculated whether the coupling into the fiber was drifting during the measurement series or if cooling reduced fiber attenuation. Once again, spurious peaks occur at wavelengths of 700 nm and below. Overall the cooling of the fiber only had minor impact on Raman scattering, and as a result the spontaneous FWM was still not observed. Cooling of the fiber only impacts Ra-

man scattering within a few THz from the pump [92]. This means the impact is insignificant, after being spread out by several cascaded Raman processes to wavelengths at approximately 1432 nm. The minor changes that were observed in the spectra are also partly attributed to thermo-optic effects introduced by temperature changes of the fiber [93]. Reasons for why spontaneous FWM is not observed are discussed in further detail in Sec. 6.5.

6.3.3 Mode Images using Bandpass Filters

Several spurious peaks appeared in the previous measurements. To verify that continuum is in fact being generated for wavelengths on either side of the pump, the fiber mode was imaged using different bandpass filters, hereby confirming that the continuum is not a mere artifact of the spectrometer and the OSA, and furthermore verifying that the field is in the expected mode at all wavelengths. According to the datasheet the filters provide at least 40 dB suppression at 1064 nm. For some filters it was ensured that the transmission of the pump was too low to be detected by the camera. The different mode images are presented in Fig. 6.12. All the mode images were taken while the fiber was cooled and

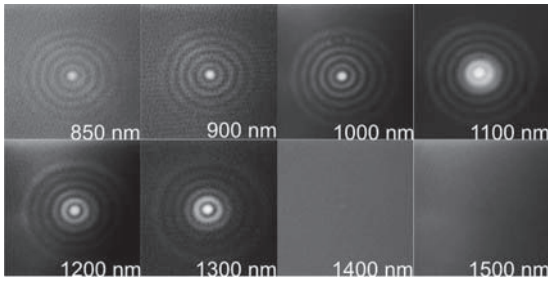

Figure 6.12: Eight mode images using different bandpass filters.

the pulse energy was at 70 μJ. The repetition rate of the laser is lower than the sampling frequency of the camera, therefore the mode images were flickering. Several pictures were taken and the clearest were selected. This means that direct comparison of the different pictures is not possible. The LP_{06} mode is observable at most of the wavelengths, however at 1400 nm only a faint center peak is seen, and at 1500 nm it is not possible to see any mode. The mode at 1100 nm appears less clear in the center. This is because the LPG only converts 87.4 % of the pump power to the higher order mode. The remaining 12.6 % of the pump power stays in the fundamental mode, and via Raman scattering this generates LP_{01} light at this wavelength, which is near the Raman gain peak. The Raman effect is also stronger in the fundamental mode, since the effective area for LP_{01} is smaller than for the HOMs. Nevertheless, it is clearly seen that a continuum over these wavelengths is being generated.

6.3.4 Cutback Measurement

The evolution of the generated spectrum is investigated using a cutback measurement. The fiber device used for this particular experiment is the LP_{06}-B grating shown in Fig. 4.6. For the experiment the pulse energy was fixed at 50 μJ. This measurement was carried out before the power calibration was performed, shown in Sec. 6.2.2. Unfortunately, the "peak hold" function on the OSA was used, so the data is not quantitative and one should be hesitant to draw conclusions based on power level comparisons. The measured spectra for the cutback measurement are shown in Fig. 6.13. It is seen that

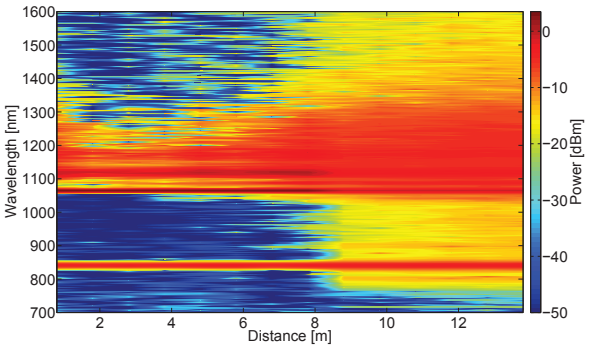

Figure 6.13: Contour plot of the spectra measured on the OSA as a function of propagation distance. The step size for the cutback measurement is 2 meters.

initially only Raman scattering from the pump is generated. After a length of approximately 8 m, the products of the FWM process between the pump and the Raman gain is noticeable above the noise floor. Approaching the end of the fiber, the pump and 1st order Raman gain peak appear depleted and the spectrum is not changing significantly as a function of length. Throughout the contour plot the spurious peak at 840 nm is seen.

6.4 Experiments with Pump in LP_{07} Mode

In this section the experiments are presented, where the pump is in the LP_{07} mode [88, 94]. The phase matching curve for the 130 μm OD fiber where all fields are in the LP_{07} mode is seen in Fig. 6.14. The pump wavelength is set at $\lambda_p = 1064$ nm. For the analytical approximation of the gain region, the pump power was set at $P_p = 10$ kW. In the figure, the maximum small signal gain occur at wavelengths of 1041 and 1088 nm.

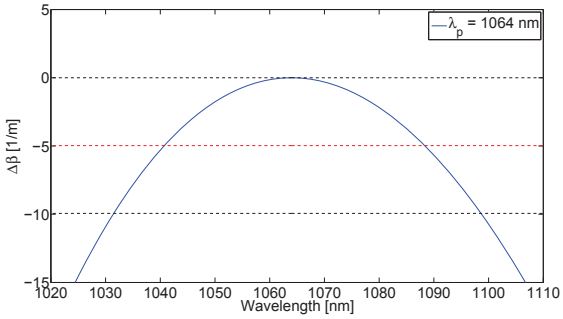

Figure 6.14: Phase matching curve when all fields are in LP_{07}.

6.4.1 Cutback Measurement

The fiber device used for this experiment is the LP_{07} grating shown in Fig. 4.6. The length of the fiber after the grating was 11 m. The experimental setup used is shown in Fig. 6.1, however in this specific experiment no signal seed was used. A cutback measurement was performed to investigate spontaneous FWM; the result is seen in Fig. 6.15. During the experiment the pump energy was fixed at 28 μJ. It is seen from the spectra that modulation instability (MI)

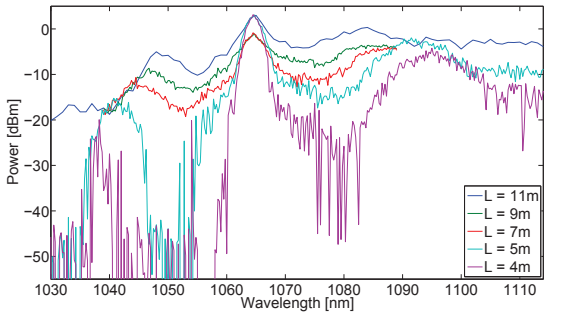

Figure 6.15: Spectra from the OSA using "peak hold" showing a cutback measurement. The length of fiber after the LPG is provided in the legend.

peaks appear on either side of the pump, which are moving apart as the fiber length is shortened. During these measurement it was at first not realized that these peaks were moving, so unfortunately the wavelength range is too narrow on the Stokes side for fiber lengths of 7 and 9 m, however on the anti Stokes side, it is clear that the peak is moving.

The MI peaks appear at 1049 and 1084 nm at 11 m, which is in fairly good agreement with the analytical approximation. However, for a length of 4 m,

the MI peaks are at 1038 and 1095 nm, hence a discrepancy with theory is introduced as the fiber is shortened. The movement of the MI peaks could be explained by the pump depleting as a function of increased fiber length, leading to a decrease in the nonlinear phase mismatch, which causes the maximum gain wavelengths to move closer together. In other words, the value of the red dashed line in Fig. 6.14 is proportional to the pump power. As the pump power is decreasing the wavelength of maximum gain moves closer to the pump wavelength. However, in the spectrum the pump is saturated, but according to unsaturated spectra in Sec. 6.4.2 the MI peaks are more than 20 dB below the pump power, hence the pump is barely depleted. Also this suggestion would indicate that the wavelength for maximum small signal gain is given by the MI peaks for a length of 4 m, which is not in agreement with the analytical approximation. Both of these arguments indicate that pump depletion is not the cause of the movement of the peaks. Another hypothesis is the shift is caused by outer diameter (OD) variations along the fiber. Simulations show that a change in OD of 7 % is required in order to shift the MI peak the required 11 nm. A change in OD of this magnitude would result in the resonance of the LP_{07} grating shift by 190 nm. This was never observed experimentally, therefore it is concluded that OD variations alone could not cause this shift in MI peaks. The simulations for this are shown in Fig. E.7 in App. E. Another cause for the shift may be that the wavelengths of the peaks are determined by a complicated interplay between several nonlinear processes. The balance between these different effects changes as a function of length, leading to the shift of the peaks. A strong indication of this is that the peaks are not occurring symmetrically around the pump frequency. For all lengths they are red shifted by 2 nm, thereby indicating that several effects are at play. The exact reason is unknown and could be a combination of the three mentioned causes. Since the exact cause of where the peaks appear is unclear, it is difficult to conclude anything from the discrepancy with the theory. In Sec. 6.4.3 the on-off gain profile is measured and this fits with the theoretical predicted wavelengths. In this context, the origin of the MI peaks is also discussed further.

6.4.2 Spontaneous Four Wave Mixing

The spontaneous FWM is measured using the OSA with an external trigger and with the Avantes spectrometer. For these experiments, the length of fiber after the grating was 4 m. As with the LP_{06} devices, it is once again attempted both when the fiber was at room temperature and when the fiber was cooled with liquid nitrogen. The difference between the two measurement series is minor, therefore the spectra for the cooled fiber are shown in Fig. 6.16, whereas the spectra for the uncooled fiber are moved to App. E in Fig. E.8. In Fig. 6.16, the MI peaks occur at 1038 and 1095 nm. A broad continuum is generated on the Stokes side of the pump. It is attributed to spontaneous cascaded Raman scattering. The continuum on the anti Stokes side is caused by FWM between the pump and the Raman continuum. This leads to the power of the MI peak on

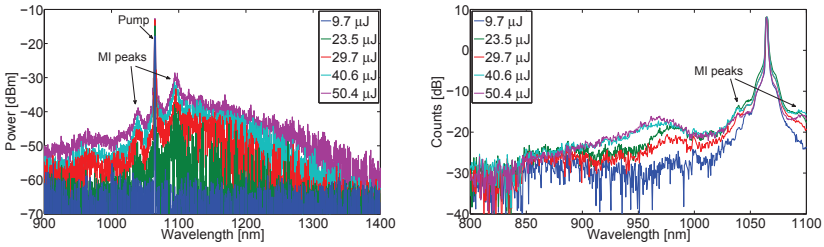

(a) (b)

Figure 6.16: Measured spectra at different pump powers with no seed signal. The fiber was cooled with liquid nitrogen. (a) On OSA. (b) On Avantes spectrometer.

the Stokes side being higher than on the anti Stokes side. For the spectrometer these peaks are very weak; this is expected to be a side effect of the strong saturation at the pump wavelength. For the uncooled fiber the peaks were clearly seen on the spectrometer, as shown in Fig. E.8(b). Furthermore, the MI peaks are not moving further apart as the pulse energy increases, as the theory predicts, due to the increased nonlinear phase mismatch. It is expected that it is related to the peaks not only being caused by spontaneous FWM, as discussed in Sec. 6.4.1.

6.4.3 Seeded Four Wave Mixing Process

In this section the experiments are presented where the FWM process is seeded on the anti Stokes side of the pump. The signal seed is converted to the LP_{07} mode via the sideband of the LPG used to convert the pump. The grating spectrum is presented in Fig. 4.6. All the seeding experiments were performed after the cutback measurement, therefore the length of the fiber is 4 m. The total signal power in both the LP_{01} and LP_{07} modes was measured at the output of the fiber; during the experiments it was between 2 and 3 mW. The measured spectra on both the OSA and the spectrometer are seen in Fig. 6.17. The spectra in Fig. 6.17(a) clearly show FWM. The pump and the seed have generated a Stokes frequency at 1091 nm. As expected, several FWM processes are taking place and generating the wavelengths of 968, 990, 1014, and 1120 nm. All these cascaded terms are observed to increase at the same rate as a function of pump power. Also since the FWM process is now being seeded, the spontaneous MI peaks are gone since the pump power is instead converted via the stimulated processes. It was attempted to maximize and minimize the gain by altering the state of polarization of the signal seed. This turned out to have an insignificant impact on the gain, which was a general tendency noticed in several of the seeded experiments; example spectra illustrating this are shown in Fig. E.9 in App. E. In Fig. 6.17(b) it is difficult to see most of the cascaded FWM wavelengths. This is because the spectrometer measures

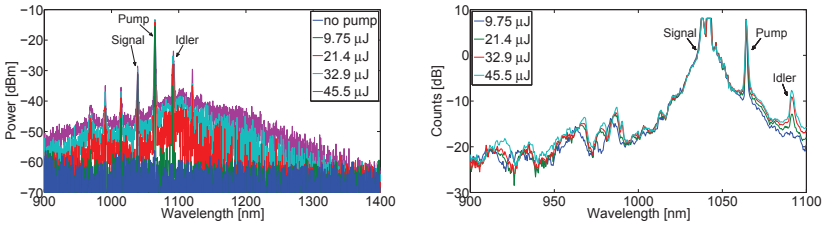

(a) (b)

Figure 6.17: Measured spectra at different pump power with a signal seed at 1038 nm. (a) On OSA. (b) On Avantes spectrometer using a ND 5 filter ($\approx$ 23 dB of attenuation).

the average power, and the average power of the signal is significantly larger than the average power of the pump. Most of the power close to the signal wavelength is caused by amplified spontaneous emission (ASE) from the dual stage Ytterbium pre-amplifier in the signal path. Therefore, the measurements on the spectrometer are omitted for the remaining seeded experiments.

6.4.4 Seeded Four Wave Mixing Process - Tunning Wavelength

For the seeded experiments, it is examined how the FWM process depends on the wavelength of the seed. For all measurements the pump pulse energy was fixed within the range of 43 to 45 μJ. The power of the signal seed was between 1.3 and 1.9 mW. The wavelength of the signal seed was tuned in the range from 1028 to 1048 nm in 5 nm steps. The measured spectra for only the seed signal, pump, and both the signal and pump are shown for different signal wavelengths in Fig. 6.18 (a)-(e). There are no cascaded terms in the spectra for the signal wavelengths of 1028 and 1033 nm; this is because these wavelength are furthest from the pump, and therefore closest to the outer boundary of the gain region, also the mode conversion of the LPG decreases for wavelengths further away from the grating resonance. It is also noticed by comparing the red and blue lines that for these two wavelengths, the MI peaks are not depleted. However, for the signal wavelengths of 1038 and 1043 nm the MI peaks are depleted. This could be an indication of excellent phase matching, and thereby a strong FWM process is required in order to deplete the spontaneous process. For a signal wavelength of 1048 nm, it appears that the MI peak on the anti Stokes side is depleted, whereas the MI peak on the Stokes side is not. This is a strong indication that the two peaks are not purely caused by MI of the FWM process. This was also discussed in Sec. 6.4.1, where it was noticed that the peaks were not symmetric in frequency on either side of the pump and that the peaks were shifting during the cutback measurement.

In Fig. 6.18(f) the on-off "gain" is calculated, which is the difference in

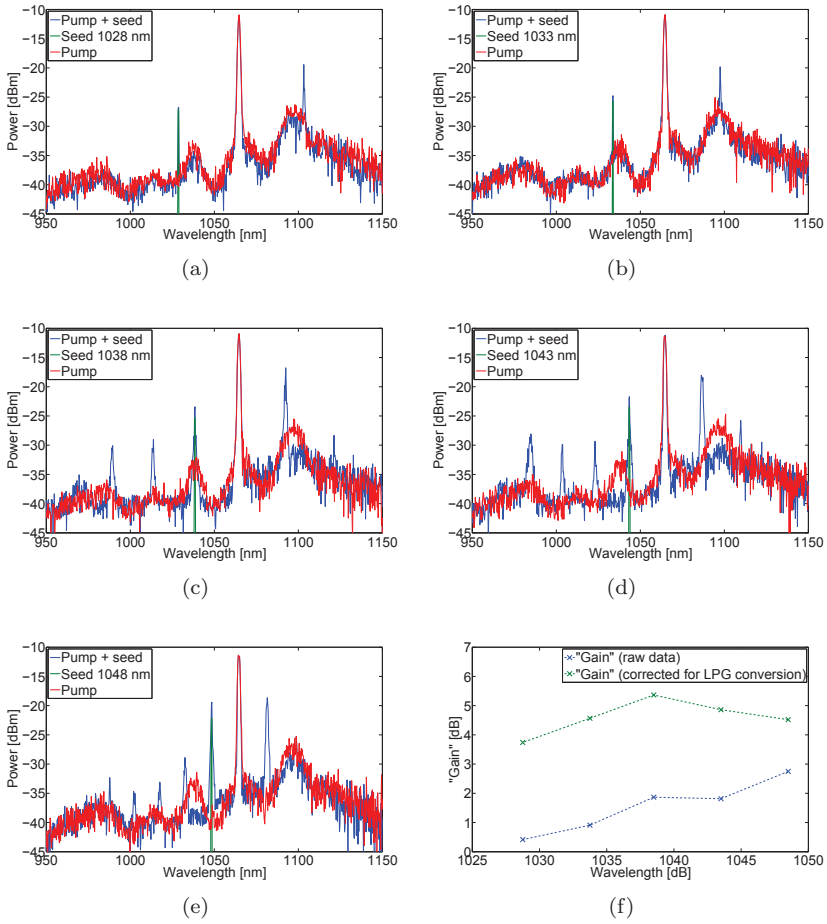

Figure 6.18: The five first plots (a)-(e) are the spectra for the five different wavelengths. The last plot (f) shows the on-off "gain" as a function of wavelength. (a) Signal wavelength 1028 nm. (b) Signal wavelength 1033 nm. (c) Signal wavelength 1038 nm. (d) Signal wavelength 1043 nm. (e) For a signal wavelength 1048 nm. (f) On-off "gain". The blue line is the difference between the blue and green line for the other five plots. For the green line, the different mode conversation ratios of the grating are taken into account.

signal power when the pump is on versus off. The quotations are used because the gain is calculated as the difference between two temporally different kinds of signals, i.e. CW and pulsed. As discussed in Sec. 6.2.1, the OSA in external trigger mode is calculating the average power over some time window. This means that the value of the gain depends on the width of this time window. The seed signal is CW, whereas when both the pump and signal is on, an approximate 5 ns pulse is generated on top of the existing CW background.

Ideally, if a 5 ns time window was used that contained the entire pulse, the gain would be an accurate measure of the gain of the pulse energy. Nonetheless, even though the value for the gain is arbitrary, it is still possible to compare gain values obtained at different wavelengths relative to each other. The green line in Fig. 6.18(f) takes into account that the LPG has different conversion ratios for the different wavelengths. For these measurements, the maximum gain is obtained at a wavelength of 1038 nm. This is fairly close to the theoretical predicted wavelength of maximum small signal gain which was found at 1041 nm.

After the former experiments, the pump pulse energy was increased to 105 μJ. The measured spectra for a signal wavelength of 1038 nm are included in Fig. E.10 in App. E. In this case, the corrected gain was found at 10.9 dB.

6.4.5 Mode Images using Bandpass Filters

In this section the mode is imaged at different wavelengths using bandpass filters. For the measurements it was achieved to couple a pump pulse energy of 105 μJ into the fiber without damaging it. This was substantially higher than the previous record of approximately 70 μJ. The generated broad continuum spectrum is presented in Fig. 6.19. It appears that the power for wavelengths

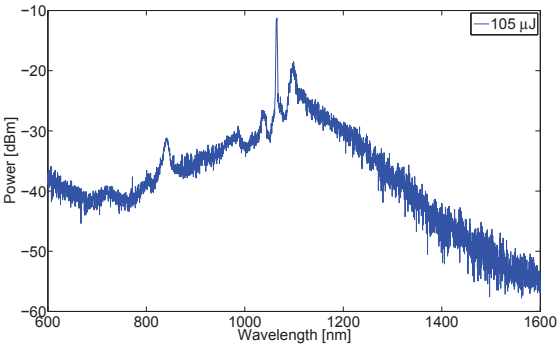

Figure 6.19: Measured spectrum for a pump pulses energy of 105 μJ.

below 680 nm is increasing, however this is the noise floor of the OSA in external trigger mode.

The fiber modes were imaged using different bandpass filters. Hereby confirming that the continuum is not a mere artifact of the OSA, while also verifying that the field is in the expected LP_{07} mode at all wavelengths. The different mode images are displayed in Fig. 6.20. Once again direct comparison of the different images is not possible. It is noticed that the LP_{07} mode is observed at all wavelengths except at 600 nm, where only the center peak and

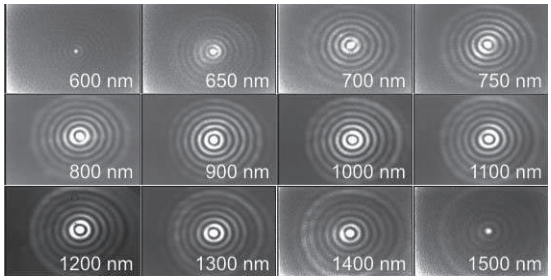

Figure 6.20: Twelve mode images using different bandpass filters.

inner ring are faintly seen. For the LP_{06} modes shown in Fig. 6.19, it was seen that the LP_{01} mode was present on the Stokes side. However, this grating is converting 99.5 % of the pump power to the LP_{07} mode, therefore barely any Raman scattering from the fundamental mode is present. Thus the modes are clear even on the Stoke side.

Though this is not directly relevant for this project, it still demonstrates the path towards more than an octave spanning continuum, which is entirely in a HOM. Due to the free space divergence resistant properties of Bessel-like modes [17], this could find relevant applications, for instance for optical coherence tomography, where broad spectrum fiber based sources could prove useful [95, 96].

6.5 Discussion of Experiments

In the experiments, spontaneous FWM was never observed when pumping in the LP_{06} mode, but only when pumping in the LP_{07} mode. However, as seen from the spectra, FWM was weak compared to the amount of generated spontaneous Raman scattering. Also when the FWM process was seeded, the spontaneous FWM decreased, whereas the Raman background remained unchanged. If the processes were equally strong, it would be expected that the seeded FWM process would deplete the pump and consequently cause a decrease in Raman scattering. An important difference between the two nonlinear processes is that FWM requires phase matching, whereas the Raman process relies on inelastic scattering. This means that a reason for Raman scattering being stronger than FWM could be OD variations along the fiber. In Sec. 5.4 the magnitude of the OD variations was estimated at ± 0.7 % based on the spread in LPG resonances for a given grating pitch. The pieces of fiber used for the gratings were taken from different sections from over hundreds of meters of fiber. Therefore, it was expected that the OD variations were significantly smaller over the few meters required for the FWM experiment. However, if the magnitude of the OD variations are ± 0.7 %, then simulations showed that this reduces the small

signal gain from 22 dB/m to a few dB/m. Therefore, it is expected that this could be the reason for the failure of the LP_{06} experiments. The hypothesis of OD variations is also in agreement with spontaneous FWM only being observed when pumping in the LP_{07} mode, since OD variations have less impact on the FWM process, when the gain region is closer to the wavelength of the pump [81]. Another contributing reason could be that the pump is far from being transform limited, i.e. the pump has a lot of phase noise, which leads to a linewidth of the pump of 0.16 nm. The gain region on the idler side is 2 nm wide, and a shift in pump wavelength of 0.16 nm leads to a shift in this gain region of 1 nm. Therefore, the linewidth of the pump leads to broadening of the FWM gain region, whereas it barely impacts the Raman process.

It is noted that even though spontaneous FWM was not observed when pumping in the LP_{06} mode, it would still be interesting to investigate if seeded FWM is possible. This is discussed further in Chap. 8. Furthermore, due to the dominating role of spontaneous Raman scattering, which is expected to be caused by OD variations and a non transform limited pump, it is speculated whether the simulations for the monomode case would agree with a seeded LP_{06} experiment. In this regard, important additions to the simulations are discussed further in Chap. 8.

6.6 Summary

The experimental setup was presented and different components were characterized. This include a temporal and spectral analysis of the Nd:YAG pump laser, different measuring modes on the OSA, and power calibration of the different detectors.

In the HOM FWM experiment when the pump was in the LP_{06} mode, it was expected that spontaneous FWM should occur at 846 and 1432 nm. This was investigated both at room temperature and when cooling the fiber with liquid nitrogen. Also a cutback measurement was performed to examine how the spectral components depend on the fiber length. Nevertheless, spontaneous FWM was never observed. It is speculated that the two main causes for this is OD variations along the fiber and phase noise of the pump source.

For the experiments where the pump was in the LP_{07} mode, spontaneous FWM was generated in the form of MI peaks on either side of the pump. These MI peaks did not occur symmetrically around the pump frequency, and a wavelength shift was noticed as a function of fiber lengths. The physical reason for these effects were never fully understood, however three contributing causes were discussed. The most plausible cause is that the peaks were not purely generated by FWM, but instead resulted from interplay between several effects. Finally, multiple FWM signal and idler lines were demonstrated in the 1 μm wavelength regime using the LP_{07} mode.

7

Conclusion

The overall aim of this PhD project is to utilize higher order modes (HOMs) in a controlled manner to obtain momentum conservation in four-wave mixing (FWM) processes, thus demonstrating a new platform for nonlinear mixing processes.

In this process a double cladding fiber was designed, which for a specific selection of modes enabled phase matching between a pump in the ytterbium gain band and a broad wavelength range in the telecommunication band, hereby realizing a fiber laser tunable over 25 nm around 800 nm. This was achieved by selecting the idler and half of the pump power in the LP_{04} mode, while the other half of the pump power and the signal was selected in the LP_{05} mode. Upon arrival of the fiber from the manufacture, Nufern, it was experimentally demonstrated that 99.8 % power conversion from the fundamental mode to a desirable LP_{0X} mode was possible using long period gratings (LPGs). Furthermore, it was demonstrated that the HOMs could propagate over at least 14 m without significant mode coupling.

Pulse propagation simulations were presented for generating wavelength conversion to approximately 800 nm. This was done for two different mode combination schemes: the monomode case and the above mentioned intermodal case. Through these simulations the impact of pulse shape, overlap integrals, and self phase modulation (SPM) in the fundamental mode before the grating were investigated. Furthermore, the impact on the gain spectrum of outer diameter (OD) variations along the fiber was examined. Here it was found that worst-case scenario OD variations estimated by the spread in LPG resonances could significantly deteriorate the gain spectrum. Finally, it was demonstrated that using the new HOM platform energy scalability is possible. By increasing the fiber dimensions and choosing the modes accordingly, it is possible to obtain similar phase matching curves (PMCs) for modes with lower peak intensities, thus allowing for an increase in power before the onset of dielectric breakdown in the fiber.

Experimentally modulation instability and multiple FWM signal and idler

lines were demonstrated in the 1 μm wavelength range in a large mode area fiber. This was enabled by operating in the LP_{07} mode, which has anomalous dispersion despite having a mode area of 618 μm^2 at 1064 nm. In the experiments the maximum employed pump pulse energy was 105 μJ, only limited by the available laser since the fiber is capable of propagating pulse energies of 540 μJ before the onset of dielectric breakdown. This represents a 12-times increase compared to photonic crystal fibers (PCFs) with similar anomalous dispersion characteristic. Finally, a peripheral result was obtained in the unseeded experiment, where a continuum from 680 to 1600 nm, entirely in the LP_{07} mode was generated.

It was not possible to attempt the experiment involving wavelength conversion to 800 nm within the time frame of this project. However, it is concluded that this ambition is still possible, provided that a tunable pump source is available, along with a fiber with OD variations less than ± 0.1 %.

8

Outlook

This chapter presents aspects that could be interesting for continuation of the project. In the first section, it is discussed how spontaneous Raman scattering and the noise of the pump is included in the simulations. The following section focuses on continuation of the experiments. The final section gives a general discussion of new directions that could be taken, which are related to this PhD project.

8.1 Simulations

In order to improve the agreement between the simulations and the experiments, it is recommended that outer diameter (OD) variations along the fiber and phase noise of the pump are included. In the regime where these effects occur, spontaneous Raman scattering becomes even more significant and should, therefore, also be included. In the simulations presented in this thesis, the nonlinear Schrödinger equation is decoupled into three or four coupled equations, given by Eq. (2.1.16) and Eq. (2.1.7). This is advantageous if only certain narrow frequency bands are considered. However, since this is no longer the case, a single nonlinear Schrödinger equation must be solved where the initial input is the pump and signal frequency components, along with one photon per mode, which represent the vacuum fluctuations initializing the spontaneous process. As seen from the experiments, the wavelength range of interest is from 600 to 1600 nm, and yet the frequency resolution must be sufficient to resolve nanosecond pulses. The spectral width of a transform limited 3 ns pulse is approximately 150 MHz. With a frequency resolution of 50 MHz this yields 2^{23} data points, which would require tremendous computational time. One could investigate if useful insight is obtained by using picosecond pulses instead. Since this is still considered the quasi-continuous wave (CW) regime, only a limited overestimation of dispersion effects is introduced. However, the required frequency resolution and, thereby, the computational time are reduced.

The second challenge is how to model a pump that is far from being transform limited. In order to avoid this being a tremendous unknown simulation parameter, it is expected that further examination of the dynamic noise behavior of the pump is needed.

The experiments were carried out toward the end of this PhD project, so it was not possible to include the above mentioned simulations. Furthermore, the pump laser was only a temporary solution, and it is expected that four-wave mixing (FWM) is observable, using a signal seed and the described master oscillator power amplifier (MOPA).

8.2 Experiments

In the continuation of the experimental work, one of the first tasks is to complete the MOPA build. Currently, the peak power of the system has reached 0.5 kW. The limitation at this point is stimulated Brillouin scattering (SBS), therefore phase modulation of the external cavity laser (ECL) seed is needed before the peak power is able to exceed the target of 10 kW. The benefits with the MOPA compared to the Nd:YAG laser system is an increase in repetition rate, which leads to measurable average power levels. Furthermore, since the MOPA is fiber based it is possible to splice the output directly to the custom designed fiber, hereby avoiding cumbersome alignment and frequent burning of the fiber devices.

For the higher order mode (HOM) FWM experiment where the pump is in the LP_{06} mode, seeding of the FWM process is suggested. Originally, it was expected that spontaneous FWM would reveal the phase matched wavelengths, and thereby indicate the wavelength where long period gratings (LPGs) should be written in order to convert the signal to the LP_{06} mode. Since this was not observed, numerous LPGs should be written over tens of nanometers on either side of the theoretical predicted phase matched wavelength. This allows for potential seeding of the process over a broad wavelength region with a signal in the LP_{06} mode.

Once the MOPA build is completed and a wavelength tunable source has been obtained, the intermodal scheme should be attempted using the custom designed fiber with an OD of 125 μm. Simulations show that this yields the desirable phase matching curves (PMCs) at a pump wavelength of 1045.9 nm, which is in the middle of the tunable wavelength range of the MOPA. Consequently, the LPGs for the pump conversion should be written as chirped gratings, such that the bandwidth of the grating accommodates the entire wavelength range of the MOPA.

If the HOM FWM experiments show indications of reduced strength of the FWM process, further analyses of the OD variations are recommended. This could be done by writing numerous gratings with few centimeters of spacing over several meters of fiber and observe the change in resonance wavelength of these gratings. If it is concluded that the OD variations is an issue for

the considered fiber, the only solution is to acquire a new fiber with reduced OD variation, which are closer to commercial available fibers since simulations showed that this was acceptable.

8.3 Other New Directions

Another continuation of the project is to look into different fiber designs. The motivation could be to obtain phase matching over an even broader wavelength range than what was demonstrated in this PhD project. Alternatively, the goal could be to create high powered fiber lasers at different wavelengths, for instance for wavelengths longer than 2 μm. Yet another direction is to demonstrate HOM FWM using modes with ultra large effective areas of thousands of squared micrometers, and thereby facilitate ultra high powered fiber lasers. To realize some of these suggestions, it might be necessary to use more complicated fiber designs, which provide additional degrees of freedom. One possibility is to use several index layers, unlike the two layers of the double cladding fiber used for this project. Another direction is to demonstrate HOM FWM in air cladding or other microstructured fibers.

In this PhD project the focus was on FWM. An alternative nonlinear mixing process worth investigating is third harmonic generation. The advantage is that different wavelength ranges could be obtained, and the process is energy efficient since there is no side product of the process, as in FWM where both a signal and idler are created. The disadvantage is that the wavelengths are fixed once the pump is chosen, hence there is no freedom in choosing the interacting wavelengths as with FWM processes.

Finally, instead of focusing on developing narrow band fiber lasers, it is also possible to use this new platform for developing ultra high powered super continuum sources or frequency comb sources.

Appendix A

Pump Laser

The custom build pump laser is based on a master oscillator power amplifier (MOPA) design [97, 98]. The basic schematic is shown in Fig. A.1 The seed

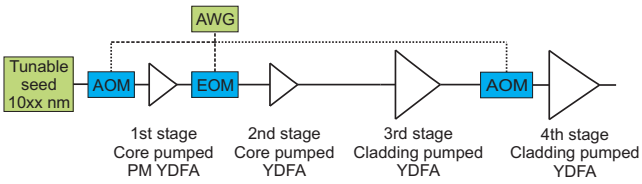

Figure A.1: Basic design of the MOPA pump source.

laser is a continuous wave (CW) tunable laser source and the wavelength range is between 1010 and 1080 nm. The first acousto optical modulator (AOM) acts as a pulse carver; this creates 3 ns pulses at a repetition rate of 200 kHz. After the first stage ytterbium doped fiber amplifier (YDFA) an electro optical modulator (EOM) defines the pulse shape. The arbitrary waveform generator (AWG) has a sampling rate of 8 GSa/s. The pulse shape out of the EOM is chosen such that, after the distortion caused by amplification saturation in the remaining amplifier stages, the output from the MOPA is a flat top pulse shape, which is desirable for nonlinear pulse conversion. Hereafter, there is another pre amplifier followed by the third stage, which is a cladding pumped YDFA. Following, is a second AOM which acts as a time-gate removing amplified spontaneous emission (ASE) between the pulses. Finally, the pulses arrive at the 4th stage, which is the main power amplifier. The target specifications for the MOPA are summarized in Table A.1.

A more detailed description and schematics of the MOPA are given in Fig. A.2. The schematics of the all fiber based pump source is displayed as Fig. A.2. All component before the electro optical modulator (EOM) are polarization maintaining (PM). The tunable CW seed is carved into pulses using

Pulse shape	Capable of almost square pulses
Peak power	10-20 kW
Pulse width	3 ns
Repetition rate	200 kHz
Wavelength range	At least 1035 to 1055 nm

Table A.1: Specifications for the MOPA.

the acousto optical modulator (AOM). After the isolator, a wavelength division multiplexing (WDM) is used to multiplex the 975 nm pump with the seed. After all pump diodes, a 975/1030 WDM is placed (not shown in the sketch), which serve as pump protection by preventing backward traveling ASE to damage the diodes. The first Ytterbium gain fiber is approximately 3 m; after this an EOM modulates the signal to give the required pulse shape. The next preamplifier section is identical to the first, except it is not PM. After this a pump combiner is used to coupled the seed and the two multi moded (MM) pump diodes into approximately 3 m of cladding pumped Ytterbium doped fiber. The second AOM is used as a time gate to remove unwanted ASE between the pulses. The final stage is the power amplifier, where six 10 W pump diodes are coupled into the Ytterbium doped cladding pumped gain fiber.

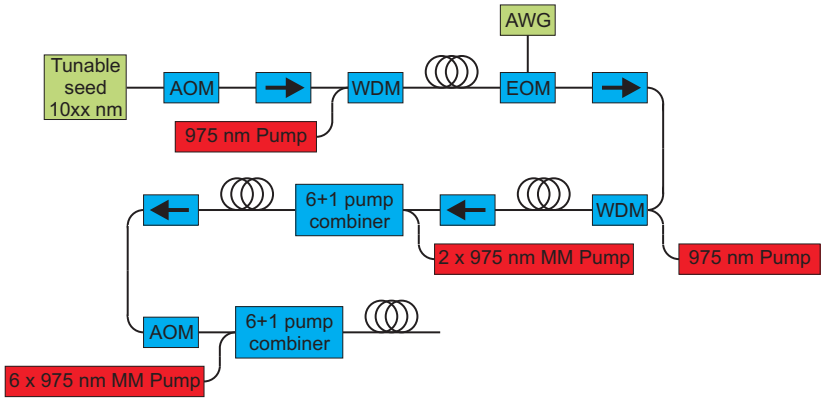

Figure A.2: Pump laser design

Appendix B

Modesolver

The matrix of the eigenvalue problem is denoted by $\mathbf{M}$, the central diagonal and two off-diagonals are given by [57]

$$\mathbf{M}(i,i) = n(i)^2k^2 - \frac{2}{\Delta r^2} - \frac{L^2}{r(i)^2} \tag{B.0.1a}$$

$$\mathbf{M}(i,i-1) = \frac{1}{\Delta r^2} - \frac{1}{2r(i)\Delta r} \tag{B.0.1b}$$

$$\mathbf{M}(i,i+1) = \frac{1}{\Delta r^2} + \frac{1}{2r(i)\Delta r}, \tag{B.0.1c}$$

where i is the discretization index, and N is the total number of points. The index profile is denoted n and the radius vector is given by r. The wavenumber is given by, $k = 2\pi/\lambda$, and Δr is the radial discretization step size.
The inner boundary condition, $i = 1$, depends on the specific mode $\mathrm{LP_{LX}}$. If L is even, the boundary conditions yields

$$\mathbf{M}(1,1) = n(1)^2k^2 - \frac{1}{\Delta r^2} - \frac{1}{2r(1)\Delta r} - \frac{L^2}{r(1)^2} \tag{B.0.2a}$$

$$\mathbf{M}(1,2) = \frac{1}{\Delta r^2} + \frac{1}{2r(1)\Delta r}. \tag{B.0.2b}$$

For the modes where L is odd, the boundary conditions are given by

$$\mathbf{M}(1,1) = n(1)^2k^2 - \frac{3}{\Delta r^2} + \frac{1}{2r(1)\Delta r} - \frac{L^2}{r(1)^2} \tag{B.0.3a}$$

$$\mathbf{M}(1,2) = \frac{1}{\Delta r^2} + \frac{1}{2r(1)\Delta r}. \tag{B.0.3b}$$

At the outer boundary, $i = N$, the boundary conditions are, regardless of the mode, given by

$$\mathbf{M}(N, N) = n(N)^2 k^2 - \frac{2}{\Delta r^2} - \frac{L^2}{r(N)^2} + \frac{1}{2r(N)\Delta r} \tag{B.0.4a}$$

$$\mathbf{M}(N, N-1) = \frac{1}{\Delta r^2} + \frac{1}{2r(N)\Delta r}. \tag{B.0.4b}$$

Appendix C

Airclad Fiber

The fiber is a double cladding fiber with a Germanium doped core that guides the fundamental mode, and a silica inner cladding region where the higher order modes (HOMs) are guided. The outer cladding region consists of a ring of air holes. A picture of the endfacet of the fiber is seen in Fig. C.1(a); this fiber was cleaved with 160 g of tension. The measured index profile of the fiber is seen in Fig. C.1(b). This measurement was performed using a commercial interferometric index profiler, IFA-100 Fiber analyzer. The system is only capable of measuring index differences less than 0.02. Consequently, the air holes were filled with index matching oil using capillary forces. Therefore, there is index matching oil in the region from 25 to 35 μm. Also the fiber is submersed in the same index matching oil, leading to the ambient index for radii larger than 62.5 μm. The blue line in Fig. C.1(b) is the measurement of

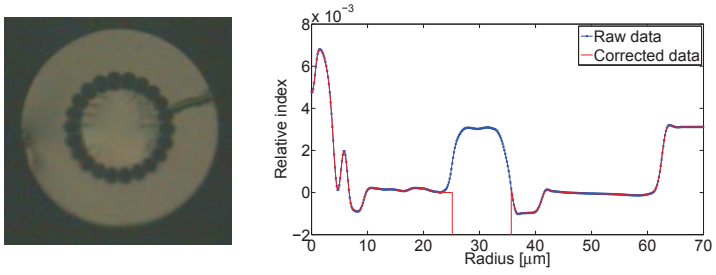

(a) (b)

Figure C.1: (a) Endfacet of OFS air cladding fiber. (b) Index profile relative to pure silica of the OFS air cladding fiber.

the relative index profile. The red line is the corrected data; here it is taken into account that the oil is filled in the holes. The boundary of the airholes is defined as the mid-point of the slope, which was found to be 25.1 μm. The index from 23.0 μm to the mid-point, was set to the average value of the

index of the silica region from 10.0 to 23.0 μm. The absolute index of the profile and the wavelength dependence was defined so the silica region was offset according to the Sellmeier coefficients [48]. With the corrected index profile, good agreement was obtained between simulated and experimentally measured long period grating (LPG) phase matching curves (PMCs) as seen below.

C.1 Long Period Grating Phase Matching Curves

In order to write LPGs in the air cladding fiber, the PMCs were simulated. This was done using both a scalar modesolver, described in Sec. 2.2.1, and finite element method (FEM) simulations using COMSOL. For the scalar modesolver simulations, the corrected relative index profile shown in Fig. C.1(b) was utilized. For the FEM simulations in COMSOL, the core of the fiber profile was used from the core region of the corrected index profile, shown in Fig. C.1(b). The air holes of the structure were defined according to the image shown in Fig. C.1(a). In Fig. C.2 the LPG PMCs are shown for coupling from LP_{01} to the LP_{0X} mode, given by Eq. (2.3.4). It is seen that the scalar modesolver and the FEM simulations are in fairly good agreement with each other. Each

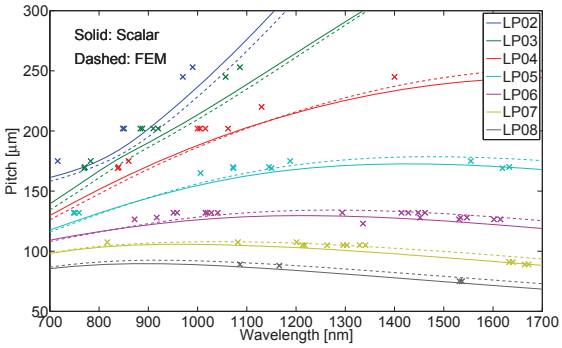

Figure C.2: Phase matching curves for the OFS air cladding fiber showing the pitch required to couple from LP_{01} to LP_{0x}. The solid lines are found using a scalar modesolver and the dashed lines are found using FEM simulations in COMSOL. Each cross represents an experimentally written LPG.

cross on the figure indicates an experimentally written LPG. The color of the crosses relate to the mode of the given resonant coupling, which was verified by imaging the modes at wavelengths where sources were available. The experimental data is in excellent agreement with the simulations especially for the LP_{05}, LP_{06}, and LP_{07} modes, which are the modes of interest for a four-wave

mixing (FWM) experiment. The gratings are written with different exposure time, hence they experience different DC shifts. This means that the same pitch could yield different resonance wavelengths. Furthermore, in the fabrication process a crucial alignment parameter is to observe the diffraction pattern from the fiber. The airholes in the fiber complicate this procedure, since the holes scatter the light and causes the diffraction pattern to appear as a speckle pattern. This means that reproducibility for air cladding fibers are lower than for conventional step index fibers. The scalar modesolver is expected to breakdown for large index steps in the profile. However, since the agreement between scalar modesolver and experimental data is acceptable, at least sufficient for a qualified initial guess for the pitch of the LPG, the scalar modesolver has primarily been utilized in this project.

C.2 Stability of Modes in Air Cladding Fiber

Stable propagation of the modes in the fiber was examined by writing a LPG that converts from the fundamental mode to the LP_{05} mode. After the grating is a 5 m piece of fiber on which a cutback measurement was performed. At each length of fiber, the mode at the end facet is imaged. These images are seen in Fig. C.3. From Fig. C.3(a), it is clear that the mode is primarily in LP_{05},

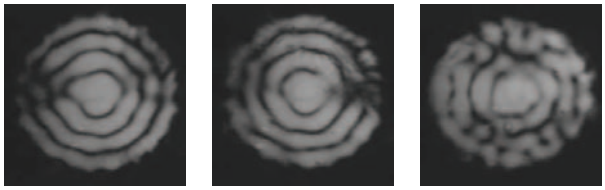

(a) 0 m. (b) 0.1 m. (c) 0.5 m.

(d) 1.8 m. (e) 3.6 m. (f) 5.0 m.

Figure C.3: Images of the LP_{05} mode at different propagation lengths after the grating.

however 1 % of the light is still in LP_{01}. The fundamental mode is only guided in the core region of the fiber. Therefore, it is not possible to see the dark ring between the center peak and the first ring of the LP_{05} mode due to the presence of LP_{01}. In most of the mode images in Fig. C.3 it is observed that the mode is blurred along a line across the mode image. In Figs. C.3(a) and C.3(b) this line

is horizontal and through the center of the mode, whereas in Fig. C.3(e) this line goes from the top left to the bottom right corner. This is a consequence of the cleave and is examined further later in this section. However, the tendency is clear, the mode becomes increasingly distorted as a function of propagation length, and after approximately 0.5 m, it is almost impossible to identify the mode. In the experiments it was noticed that the mode image was sensitive towards even slight bends of the fiber, a clear indication of mode coupling. It is expected that this is a fundamental issue in this specific fiber, presumably caused by rotation of the air holes along the fiber. Successful HOM propagation in airclad fibers have been demonstrated in the past [10].

As mentioned, it was suspected that the line distortions in the modes were related to ripples across the surface of the fiber, which arise as the cleave is spreading across an air cladding fiber. In order to examine the impact of the cleave quality on the distortion of the modes further, the holes in the fiber were collapsed using a fusion splicer, see Fig. C.4(a). Subsequently, the fiber was cleaved in the collapsed hole region, leaving about 40 μm of collapsed hole region; the end facet of the cleave is shown in Fig. C.4(b). This ensures a smoother end facet since the cleave is able to spread through the solid fiber without creating any ripples across the end facet. Fig. C.4(c) shows the image after 5 m of propagation, and as before, the line of distortion is noticed. Fig. C.4(d) shows the image of the collapsed fiber, it is seen that the line distortion is gone. However, the mode is still heavily distorted, and the similarities with the LP_{05} are almost non existent. Since the cleave quality of the fiber is not causing the distortion of the mode images, it is with certainty concluded that stable propagation is not possible in the airclad fiber.

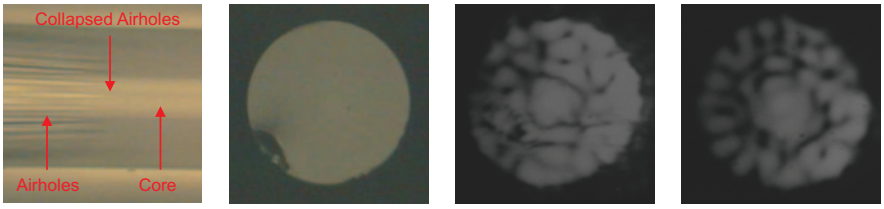

Figure C.4: (a) Side view of the collapsed air holes. (b) End facet view of the cleave through collapsed air hole region. (c) Mode image when the fiber was cleaved through the air holes. (d) Mode image when the fiber was cleaved in the collapsed air hole region.

A FWM experiment in the specific fiber over a length of less than 0.5 m would require tens of kW of peak power. For this reason, it was decided not to pursue a FWM air cladding experiment and instead all attention was focused on the custom designed fiber.

Appendix D

Mode Identification

Using the setup shown in Fig. 4.2, the long period gratings (LPGs) were characterized. Examples of two spectra are seen in Fig. D.1. However, for these measurements the fibers were not spliced together, their end facets were merely physically coupled. There is a significant coupling loss and multi path interfer-

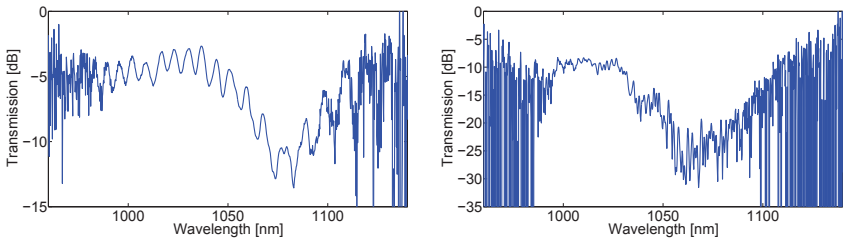

Figure D.1: Grating transmission spectra (a) LPG for the LP_{05} mode, the pitch is $\Lambda = 312.5$ μm, grating length $L = 1$ cm, and the exposure time was $t_e = 150$ s. (b) LPG for the LP_{06} mode, the pitch is $\Lambda = 215$ μm, grating length $L = 1$ cm, and the exposure time was $t_e = 750$ s.

ence (MPI) for these measurements. However, the main purpose is merely to characterize the LPG phase matching curves. For this, it is possible to determine that the resonance wavelengths are approximately 1080 nm and 1065 nm, respectively. The noticeable noise at either side of the spectra appear since output power from the light emitting diode (LED) approaches the noise floor of the optical spectrum analyzer (OSA).

In order to verify the modes of the resonances, the modes are imaged, which is shown in Fig. D.2. In the mode in Fig. D.2(a) the grating resonance is weak, approximately 5-6 dB, and MPI is noticed, indicating other modes are clearly present. However, it is still identifiable that the most prominent mode is LP_{05}. In Fig. D.2(b) the resonance is much stronger, approximately 15 dB, and it is

seen that the mode is clearer. The alternations in the thickness of the rings are a clear indication that other modes are present. In both cases, it was noticed that the mode propagation was stable since movement of the fiber did not significantly change the mode image.

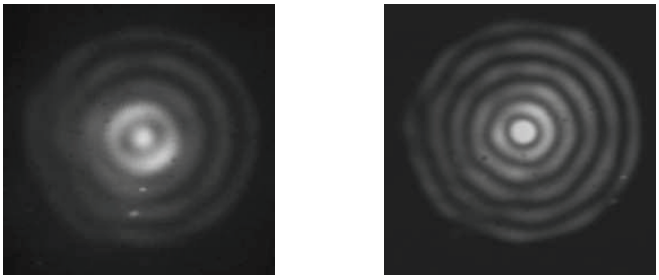

(a) (b)

Figure D.2: End facet image of the modes from the resonances shown Fig. D.1. (a) This mode is LP_{05}. (b) This mode is LP_{06}.

Appendix E

Additional Experimental Data

E.1 Characterization

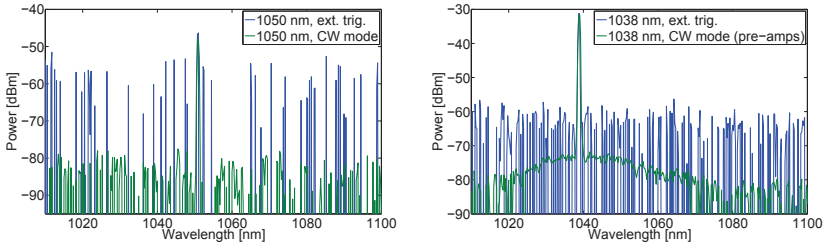

(a) (b)

Figure E.1: The CW signal is measured on the OSA, both in CW mode and using the external trigger mode. In both figures the measurements are identical, except for the level of the noise floor. (a) Seed at 1050 nm straight from the ECL. (b) Seed at 1038 nm from the ECL going through a dual stage YDFA.

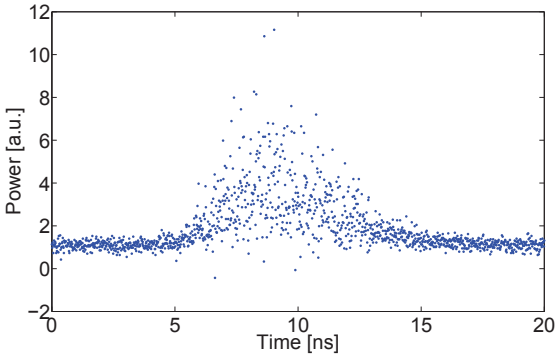

Figure E.2: Pump pulse measured with sampling scope using the signal from the photodetector as a trigger. No averaging was used when measuring this trace.

(a) (b) (c)

Figure E.3: Images of a 1 cm piece of fiber which broke off. (a) The cleaved end of the fiber. (b) The broken end. (c) The broken end from a different angle.

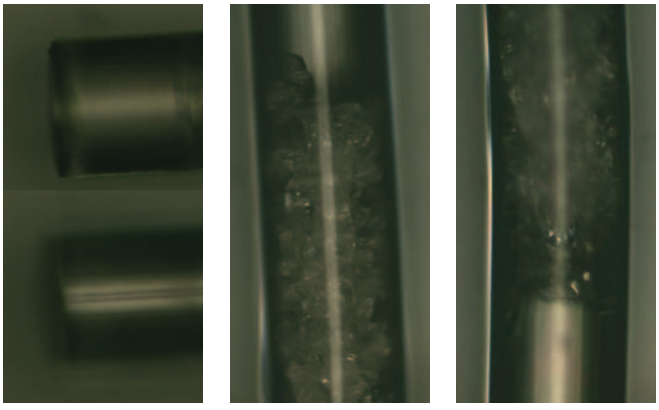

(a) (b) (c)

Figure E.4: (a) The cleaved end of the fiber. (b) The otherwise clear coating of the fiber turned white and opaque a few centimeters from the end. (c) Another section of the damaged coating.

E.2 LP_{06} Device

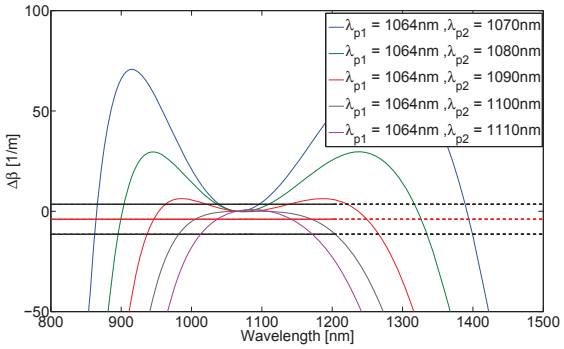

Figure E.5: Phase matching curves when all fields are in the LP_{06} mode. One of the wavelength is fixed at $\lambda_{p1} = 1064$ nm, since this is the pump wavelength. The other wavelength, λ_{p2}, is varied over the wavelength range of the 1st Raman gain peak. Notice how this phase matches with the short wavelength continuum observed in Fig. 6.10(b).

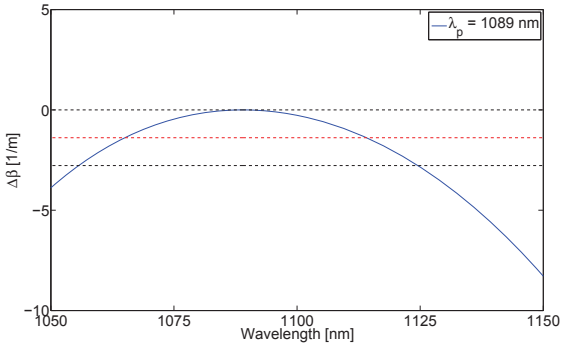

Figure E.6: Phase matching curves for the degenerate case where all fields are in LP_{06}. The pump is at $\lambda_p = 1089$ nm. It is seen that phase matching occurs with 1064 and 1115 nm. Consequently, the reverse process is also phase matched. This is where two photons at 1064 and 1115 nm are annihilated and create two photons at 1089 nm. This may explain the peak observed in Fig. 6.11(a).

E.3 LP_{07} Device

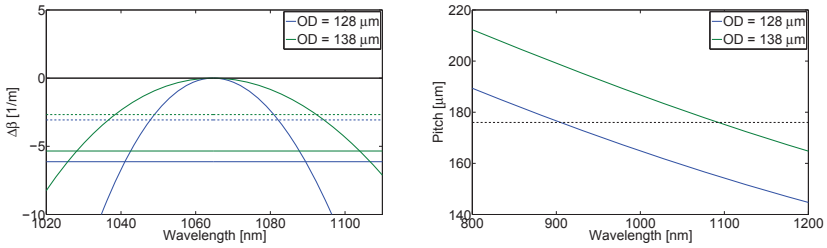

(a) (b)

Figure E.7: (a) FWM phase matching curves for two different fiber ODs. The pump power was set at 6 kW, corresponding to a pulse energy of 30 μJ. Notice that a 7 % change in OD leads to an 11 nm shift in the wavelength of maximum small signal gain (the intersection with the dotted line). (b) LPG phase matching curves for the LP_{07} mode for the two different fiber ODs. It is seen that the grating resonance shifts by 190 nm.

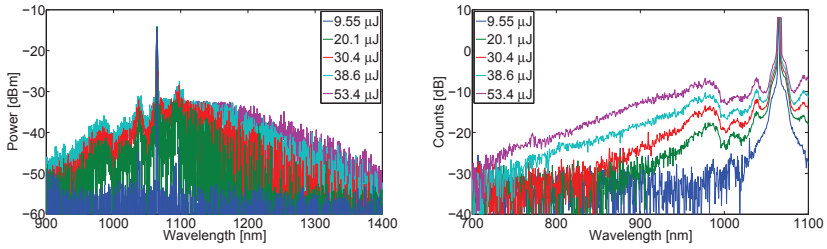

(a) (b)

Figure E.8: Measured spectra at different pump powers with no seed signal and when the fiber is at room temperature. In both figures the spectra are saturated at the wavelength of the pump. (a) On OSA. (b) On Avantes spectrometer.

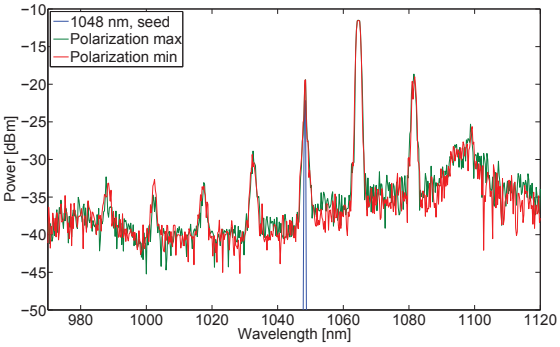

Figure E.9: By using the polarization controller in the signal path, it was attempted to minimize and maximize the gain. As seen from the spectra, this only had a minor effect on the gain.

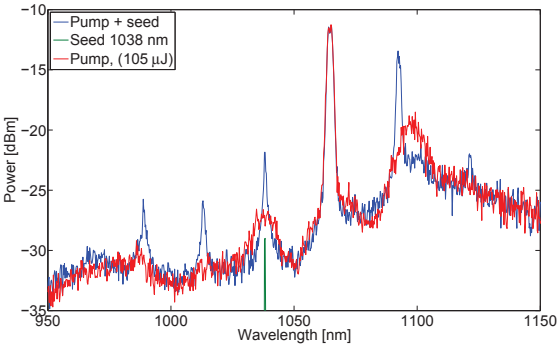

Figure E.10: The measured spectra for a signal wavelength of 1038 nm and a pump pulse energy of 105 μJ is shown. The corrected gain was found at 10.9 dB. Compared with the measurement shown in Fig. 6.18(c) where the pump pulse energy was 44 μJ, it is seen that the background is increased and the same cascaded terms are present.

Appendix F

List of Acronyms

AOM acousto optical modulator

ASE amplified spontaneous emission

AWG arbitrary waveform generator

BS beam splitter

CW continuous wave

ECL external cavity laser

EDFA erbium doped fiber amplifier

EOM electro optical modulator

FEM finite element method

FWHM full width half maximum

FWM four-wave mixing

GVD group velocity dispersion

HF hydrofluoric

HNLF highly nonlinear dispersion shifted fiber

HOM higher order mode

IR infrared

LED light emitting diode

LMA large mode area

LPG long period grating

MI modulation instability

MM multi moded

MOPA master oscillator power amplifier

MPI multi path interference

NA numerical aperture

ND neutral density

OD outer diameter

OSA optical spectrum analyzer

PC polarization controller

PCF photonic crystal fiber

PM polarization maintaining

PMC phase matching curve

SBS stimulated Brillouin scattering

SMF single-mode fiber

SPM self phase modulation

SRS stimulated Raman scattering

SVEA slowly varying envelope approximation

TAP turn around point

THG third harmonic generation

UV ultraviolet

WDM wavelength division multiplexing

XPM cross phase modulation

YDFA ytterbium doped fiber amplifier

ZDW zero dispersion wavelength

Appendix G

Bibliography

[1] T. H. Maiman, "Stimulated optical radiation in ruby," *Nature*, vol. 187, no. 4736, pp. 493–494, 1960.

[2] A. Javan, W. R. Bennett, and D. R. Herriott, "Population inversion and continuous optical maser oscillation in a gas discharge containing a he-ne mixture," *Phys. Rev. Lett.*, vol. 6, pp. 106–110, Feb 1961.

[3] R. N. Hall, G. E. Fenner, J. D. Kingsley, T. J. Soltys, and R. O. Carlson, "Coherent light emission from gaas junctions," *Phys. Rev. Lett.*, vol. 9, pp. 366–368, Nov 1962.

[4] E. Snitzer, "Optical maser action of nd^{+3} in a barium crown glass," *Phys. Rev. Lett.*, vol. 7, pp. 444–446, Dec 1961.

[5] C. J. Koester and E. Snitzer, "Amplification in a fiber laser," *Appl. Opt.*, vol. 3, pp. 1182–1186, Oct 1964.

[6] J. Nilsson, W. Clarkson, R. Selvas, J. Sahu, P. Turner, S.-U. Alam, and A. Grudinin, "High-power wavelength-tunable cladding-pumped rare-earth-doped silica fiber lasers," *Optical Fiber Technology*, vol. 10, no. 1, pp. 5 – 30, 2004.

[7] G. Agrawal, *Nonlinear Fiber Optics*. Academic Press, 4th ed., 2007.

[8] D. Nodop, C. Jauregui, D. Schimpf, J. Limpert, and A. Tünnermann, "Efficient high-power generation of visible and mid-infrared light by degenerate four-wave-mixing in a large-mode-area photonic-crystal fiber," *Opt. Lett.*, vol. 34, pp. 3499–3501, Nov 2009.

[9] J. M. Fini and S. Ramachandran, "Natural bend-distortion immunity of higher-order-mode large-mode-area fibers," *Opt. Lett.*, vol. 32, pp. 748–750, Apr 2007.

[10] S. Ramachandran, J. Fini, M. Mermelstein, J. Nicholson, S. Ghalmi, and M. Yan, "Ultra-large effective-area, higher-order mode fibers: a new strategy for high-power lasers," *Laser & Photonics Reviews*, vol. 2, no. 6, pp. 429–448, 2008.

[11] R. Stolen, "Phase-matched-stimulated four-photon mixing in silica-fiber waveguides," *Quantum Electronics, IEEE Journal of*, vol. 11, pp. 100 – 103, mar 1975.

[12] R. H. Stolen and W. N. Leibolt, "Optical fiber modes using stimulated four photon mixing," *Appl. Opt.*, vol. 15, pp. 239–243, Jan 1976.

[13] R. Stolen and J. Bjorkholm, "Parametric amplification and frequency conversion in optical fibers," *Quantum Electronics, IEEE Journal of*, vol. 18, pp. 1062 – 1072, jul 1982.

[14] T. Morioka, Y. Awaji, R. Ryf, P. Winzer, D. Richardson, and F. Poletti, "Enhancing optical communications with brand new fibers," *Communications Magazine, IEEE*, vol. 50, pp. s31 –s42, february 2012.

[15] N. Bozinovic, P. Kristensen, and S. Ramachandran, "Long-range fiber-transmission of photons with orbital angular momentum," in *CLEO:2011 - Laser Applications to Photonic Applications*, p. CTuB1, Optical Society of America, 2011.

[16] S. Randel, R. Ryf, A. Sierra, P. J. Winzer, A. H. Gnauck, C. A. Bolle, R.-J. Essiambre, D. W. Peckham, A. McCurdy, and R. Lingle, "6x56-gb/s mode-division multiplexed transmission over 33-km few-mode fiber enabled by 6x6 mimo equalization," *Opt. Express*, vol. 19, pp. 16697–16707, Aug 2011.

[17] P. Steinvurzel, K. Tantiwanichapan, M. Goto, and S. Ramachandran, "Fiber-based bessel beams with controllable diffraction-resistant distance," *Opt. Lett.*, vol. 36, pp. 4671–4673, Dec 2011.

[18] L. Rishøj and K. Rottwitt, "Excitation and characterization of higher order modes in optical fibers," *3rd Annual Workshop on Photonic Technologies and Applications: 2nd Danish-Californian Photonics Workshop*, Berkeley, California, 2012.

[19] Y. Chen, L. Yan, L. Rishøj, P. Steinvurzel, and S. Ramachandran, "Dynamically tunable optical bottles from an optical fiber," *Opt. Lett.*, vol. 37, pp. 3327–3329, Aug 2012.

[20] D. Milam, "Review and assessment of measured values of the nonlinear refractive-index coefficient of fused silica," *Appl. Opt.*, vol. 37, pp. 546–550, Jan 1998.

[21] J. W. Nicholson, S. Ramachandran, S. Ghalmi, M. F. Yan, P. Wisk, E. Monberg, and F. V. Dimarcello, "Propagation of femtosecond pulses in large-mode-area, higher-order-mode fiber," *Opt. Lett.*, vol. 31, pp. 3191–3193, Nov 2006.

[22] E. L. Buckland and R. W. Boyd, "Electrostrictive contribution to the intensity-dependent refractive index of optical fibers," *Opt. Lett.*, vol. 21, pp. 1117–1119, Aug 1996.

[23] G. Cappellini and S. Trillo, "Third-order three-wave mixing in single-mode fibers: exact solutions and spatial instability effects," *Journal of the Optical Society of America B (Optical Physics)*, vol. 8, no. 4, pp. 824–838, 1991.

[24] J. Hansryd, P. Andrekson, M. Westlund, J. Li, and P.-O. Hedekvist, "Fiber-based optical parametric amplifiers and their applications," *IEEE Journal of Selected Topics in Quantum Electronics*, vol. 8, no. 3, pp. 506–520, 2002.

[25] H. Steffensen, J. R. Ott, K. Rottwitt, and C. J. McKinstrie, "Full and semi-analytic analyses of two-pump parametric amplification with pump depletion," *Opt. Express*, vol. 19, pp. 6648–6656, Mar 2011.

[26] M. E. Marhic, Y. Park, F. S. Yang, and L. G. Kazovsky, "Widely tunable spectrum translation and wavelength exchange by four-wave mixing in optical fibers," *Opt. Lett.*, vol. 21, pp. 1906–1908, Dec 1996.

[27] J. Hansryd and P. Andrekson, "Broad-band continuous-wave-pumped fiber optical parametric amplifier with 49-db gain and wavelength-conversion efficiency," *Photonics Technology Letters, IEEE*, vol. 13, pp. 194 –196, mar 2001.

[28] J. M. C. Boggio, J. R. Windmiller, M. Knutzen, R. Jiang, C. Bres, N. Alic, B. Stossel, K. Rottwitt, and S. Radic, "730-nm optical parametric conversion from near- to short-wave infrared band," *Opt. Express*, vol. 16, pp. 5435–5443, Apr 2008.

[29] W. Wadsworth, N. Joly, J. Knight, T. Birks, F. Biancalana, and P. Russell, "Supercontinuum and four-wave mixing with q-switched pulses in endlessly single-mode photonic crystal fibres," *Opt. Express*, vol. 12, pp. 299–309, Jan 2004.

[30] J. Leong, P. Petropoulos, J. Price, H. Ebendorff-Heidepriem, S. Asimakis, R. Moore, K. Frampton, V. Finazzi, X. Feng, T. Monro, and D. Richardson, "High-nonlinearity dispersion-shifted lead-silicate holey fibers for efficient 1- mu;m pumped supercontinuum generation," *Lightwave Technology, Journal of*, vol. 24, pp. 183 – 190, jan. 2006.

[31] S. Ramachandran, "Dispersion-tailored few-mode fibers: A versatile platform for in-fiber photonic devices," *J. Lightwave Technol.*, vol. 23, p. 3426, Nov 2005.

[32] L. Grüner-Nielsen, M. Wandel, P. Kristensen, C. Jorgensen, L. V. Jorgensen, B. Edvold, B. Pálsdóttir, and D. Jakobsen, "Dispersion-compensating fibers," *J. Lightwave Technol.*, vol. 23, p. 3566, Nov 2005.

[33] S. Ramachandran, S. Ghalmi, J. W. Nicholson, M. F. Yan, P. Wisk, E. Monberg, and F. V. Dimarcello, "Anomalous dispersion in a solid, silica-based fiber," *Opt. Lett.*, vol. 31, pp. 2532–2534, Sep 2006.

[34] A. Yariv and P. Yeh, *Photonics - Optical Electronics in Modern Communication*. Oxford, 6th ed., 2007.

[35] K. Okamoto, *Fundamentals of Optical Waveguides*. Academics Press, 2nd ed., 2006.

[36] A. W. Snyder and J. D. Love, *Optical Waveguide Theory*. Chapman and Hall, 6th ed., 1983.

[37] J. Durnin, "Exact solutions for nondiffracting beams. i. the scalar theory," *J. Opt. Soc. Am. A*, vol. 4, pp. 651–654, Apr 1987.

[38] J. Durnin, J. J. Miceli, and J. H. Eberly, "Diffraction-free beams," *Phys. Rev. Lett.*, vol. 58, pp. 1499–1501, Apr 1987.

[39] S. Ramachandran and S. Ghalmi, ""diffraction-free," self-healing bessel beams from fibers," in *Conference on Lasers and Electro-Optics/Quantum Electronics and Laser Science Conference and Photonic Applications Systems Technologies*, p. CPDB5, Optical Society of America, 2008.

[40] V. Garces-Chavez, D. McGloin, H. Melville, W. Sibbett, and K. Dholakia, "Simultaneous micromanipulation in multiple planes using a self-reconstructing light beam," *Nature*, vol. 419, Sep 2002.

[41] D. McGloin, V. Garcés-Chávez, and K. Dholakia, "Interfering bessel beams for optical micromanipulation," *Opt. Lett.*, vol. 28, pp. 657–659, Apr 2003.

[42] D. Marcuse, "Influence of curvature on the losses of doubly clad fibers," *Appl. Opt.*, vol. 21, pp. 4208–4213, Dec 1982.

[43] J. W. Nicholson, J. M. Fini, A. D. Yablon, P. S. Westbrook, K. Feder, and C. Headley, "Demonstration of bend-induced nonlinearities in large-mode-area fibers," *Opt. Lett.*, vol. 32, pp. 2562–2564, Sep 2007.

[44] W. Wong, X. Peng, J. McLaughlin, and L. Dong, "Breaking the limit of maximum effective area for robust single-mode propagation in optical fibers," *Opt. Lett.*, vol. 30, pp. 2855–2857, Nov 2005.

[45] J. W. Nicholson, J. M. Fini, J. Phillips, A. DeSantolo, X. Liu, K. Feder, V. R. Supradeepa, P. S. Westbrook, E. Monberg, F. DiMarcello, C. Headley, and D. J. DiGiovanni, "Nanosecond pulse amplification in a 6000 μm2 effective area higher-order mode erbium-doped fiber amplifier," in *CLEO: QELS-Fundamental Science*, p. JTh1I.2, Optical Society of America, 2012.

[46] M. E. V. Pedersen, P. Kristensen, L. Grüner-Nielsen, and K. Rottwitt, "Impact of the scalar approximation on the prediction of the group velocity dispersion," *J. Lightwave Technol.*, vol. 29, pp. 3129–3134, Nov 2011.

[47] S. Ramachandran, P. Kristensen, and M. F. Yan, "Generation and propagation of radially polarized beams in optical fibers," *Opt. Lett.*, vol. 34, pp. 2525–2527, Aug 2009.

[48] G. Ghosh, M. Endo, and T. Iwasaki, "Temperature-dependent sellmeier coefficients and chromatic dispersions for some optical fiber glasses," *Lightwave Technology, Journal of*, vol. 12, pp. 1338 –1342, aug 1994.

[49] A. Yariv, "Coupled-mode theory for guided-wave optics," *Quantum Electronics, IEEE Journal of*, vol. 9, pp. 919 – 933, sep 1973.

[50] T. Erdogan, "Cladding-mode resonances in short- and long-period fiber grating filters," *J. Opt. Soc. Am. A*, vol. 14, pp. 1760–1773, Aug 1997.

[51] S. Ramachandran and M. F. Yan, "Static and tunable dispersion management with higher order mode fibers," in *Fiber Based Dispersion Compensation*, vol. 5 of *Optical and Fiber Communications Reports*, pp. 187–248, Springer New York, 2007.

[52] T. Erdogan, "Fiber grating spectra," *Lightwave Technology, Journal of*, vol. 15, pp. 1277 –1294, aug 1997.

[53] C. Poole, C. Townsend, and K. Nelson, "Helical-grating two-mode fiber spatial-mode coupler," *Lightwave Technology, Journal of*, vol. 9, pp. 598 –604, may 1991.

[54] S. Ramachandran, Z. Wang, and M. Yan, "Bandwidth control of long-period grating-based mode converters in few-mode fibers," *Opt. Lett.*, vol. 27, pp. 698–700, May 2002.

[55] T. Erdogan and D. Stegall, "Impact of dispersion on the bandwidth of long-period fiber-grating filters," in *Optical Fiber Communication Conference and Exhibit, 1998. OFC '98., Technical Digest*, pp. 280 –282, feb 1998.

[56] L. Rishøj, Y. Chen, P. Steinvurzel, K. Rottwitt, and S. Ramachandran, "High-energy fiber lasers at non-traditional colours, via intermodal nonlinearities," in *CLEO: Science and Innovations*, p. CTu3M.6, Optical Society of America, 2012.

[57] S. Ramachandran, "Lecture notes: Ec-568 optical fibers and waveguides," *Boston University*.

[58] A. Vengsarkar, P. Lemaire, J. Judkins, V. Bhatia, T. Erdogan, and J. Sipe, "Long-period fiber gratings as band-rejection filters," *Lightwave Technology, Journal of*, vol. 14, pp. 58 –65, jan 1996.

[59] V. Bhatia and A. M. Vengsarkar, "Optical fiber long-period grating sensors," *Opt. Lett.*, vol. 21, pp. 692–694, May 1996.

[60] S. Ramachandran, M. Das, Z. Wang, J. Fleming, and M. Yan, "High extinction, broadband polarisers using long-period fibre gratings in few-mode fibres," *Electronics Letters*, vol. 38, pp. 1327 – 1328, oct 2002.

[61] Q. Li, A. Au, C.-H. Lin, E. Lyons, and H. Lee, "An efficient all-fiber variable optical attenuator via acoustooptic mode coupling," *Photonics Technology Letters, IEEE*, vol. 14, pp. 1563 –1565, nov. 2002.

[62] I. K. Hwang, S. H. Yun, and B. Y. Kim, "Long-period fiber gratings based on periodic microbends," *Opt. Lett.*, vol. 24, pp. 1263–1265, Sep 1999.

[63] S. Savin, M. F. Digonnet, G. S. Kino, and H. J. Shaw, "Tunable mechanically induced long-period fiber gratings," *Opt. Lett.*, vol. 25, pp. 710–712, May 2000.

[64] D. Davis, T. Gaylord, E. Glytsis, S. Kosinski, S. Mettler, and A. Vengsarkar, "Long-period fibre grating fabrication with focused co2 laser pulses," *Electronics Letters*, vol. 34, pp. 302 –303, feb 1998.

[65] Y.-J. Rao, Y.-P. Wang, Z.-L. Ran, and T. Zhu, "Novel fiber-optic sensors based on long-period fiber gratings written by high-frequency co2 laser pulses," *Lightwave Technology, Journal of*, vol. 21, pp. 1320 – 1327, may 2003.

[66] G. Kakarantzas, T. A. Birks, and P. S. J. Russell, "Structural long-period gratings in photonic crystal fibers," *Opt. Lett.*, vol. 27, pp. 1013–1015, Jun 2002.

[67] C. Smelser, S. Mihailov, and D. Grobnic, "Formation of type i-ir and type ii-ir gratings with an ultrafast ir laser and a phase mask," *Opt. Express*, vol. 13, pp. 5377–5386, Jul 2005.

[68] L. Sudrie, M. Franco, B. Prade, and A. Mysyrowicz, "Study of damage in fused silica induced by ultra-short ir laser pulses," *Optics Communications*, vol. 191, no. 3–6, pp. 333–339, 2001.

[69] Y. Kondo, K. Nouchi, T. Mitsuyu, M. Watanabe, P. G. Kazansky, and K. Hirao, "Fabrication of long-period fiber gratings by focused irradiation of infrared femtosecond laser pulses," *Opt. Lett.*, vol. 24, pp. 646–648, May 1999.

[70] K. O. Hill, Y. Fujii, D. C. Johnson, and B. S. Kawasaki, "Photosensitivity in optical fiber waveguides: Application to reflection filter fabrication," *Applied Physics Letters*, vol. 32, pp. 647 –649, may 1978.

[71] P. Lemaire, R. Atkins, V. Mizrahi, and W. Reed, "High pressure h2 loading as a technique for achieving ultrahigh uv photosensitivity and thermal sensitivity in geo2 doped optical fibres," *Electronics Letters*, vol. 29, pp. 1191 –1193, june 1993.

[72] F. Bilodeau, K. Hill, B. Malo, D. Johnson, and I. Skinner, "Efficient, narrowband lp01 implies/implied by lp02 mode convertors fabricated in photosensitive fibre: spectral response," *Electronics Letters*, vol. 27, pp. 682 –684, april 1991.

[73] T. Erdogan, V. Mizrahi, P. J. Lemaire, and D. Monroe, "Decay of ultraviolet-induced fiber bragg gratings," *Journal of Applied Physics*, vol. 76, pp. 73 –80, jul 1994.

[74] V. Dangui, M. J. F. Digonnet, and G. S. Kino, "Ultrabroadband single-mode long-period fiber gratings using high-order cladding modes," *Journal of Applied Physics*, vol. 96, pp. 5987 –5991, dec 2004.

[75] Q. Zhang and M. I. Hayee, "Symmetrized split-step fourier scheme to control global simulation accuracy in fiber-optic communication systems," *J. Lightwave Technol.*, vol. 26, pp. 302–316, Jan 2008.

[76] J. Cheng, M. Pedersen, K. Charan, C. Xu, L. Grüner-Nielsen, and D. Jacobsen, "High-efficiency intermodal four-wave mixing in a higher-order-mode fiber," in *CLEO: Science and Innovations*, p. CTh3G.6, Optical Society of America, 2012.

[77] M. Karlsson, "Four-wave mixing in fibers with randomly varying zero-dispersion wavelength," *J. Opt. Soc. Am. B*, vol. 15, pp. 2269–2275, Aug 1998.

[78] M. Farahmand and M. de Sterke, "Parametric amplification in presence of dispersion fluctuations," *Opt. Express*, vol. 12, pp. 136–142, Jan 2004.

[79] F. Yaman, Q. Lin, S. Radic, and G. Agrawal, "Impact of dispersion fluctuations on dual-pump fiber-optic parametric amplifiers," *Photonics Technology Letters, IEEE*, vol. 16, pp. 1292 –1294, may 2004.

[80] M. Marhic, K.-Y. Wong, and L. Kazovsky, "Wide-band tuning of the gain spectra of one-pump fiber optical parametric amplifiers," *Selected Topics in Quantum Electronics, IEEE Journal of*, vol. 10, pp. 1133 – 1141, sept.-oct. 2004.

[81] L. S. Rishøj and K. Rottwitt, "Influence of variations of the gvd on wavelength conversion at second gain region of a parametric process," in *Nonlinear Photonics*, p. NTuC11, Optical Society of America, 2010.

[82] N. Kuwaki and M. Ohashi, "Evaluation of longitudinal chromatic dispersion," *Lightwave Technology, Journal of*, vol. 8, pp. 1476 –1481, oct 1990.

[83] P. Velanas, A. Bogris, and D. Syvridis, "Impact of dispersion fluctuations on the noise properties of fiber optic parametric amplifiers," *J. Lightwave Technol.*, vol. 24, p. 2171, May 2006.

[84] M. Hirano, T. Nakanishi, T. Okuno, and M. Onishi, "Silica-based highly nonlinear fibers and their application," *Selected Topics in Quantum Electronics, IEEE Journal of*, vol. 15, pp. 103 –113, jan. 2009.

[85] B. P.-P. Kuo, J. M. Fini, L. Grüner-Nielsen, and S. Radic, "Dispersion-stabilized highly-nonlinear fiber for wideband parametric mixer synthesis," *Opt. Express*, vol. 20, pp. 18611–18619, Aug 2012.

[86] J. M. Stone and J. C. Knight, "Visibly "white" light generation in uniformphotonic crystal fiber using a microchip laser," *Opt. Express*, vol. 16, pp. 2670–2675, Feb 2008.

[87] B. C. Stuart, M. D. Feit, A. M. Rubenchik, B. W. Shore, and M. D. Perry, "Laser-induced damage in dielectrics with nanosecond to subpicosecond pulses," *Phys. Rev. Lett.*, vol. 74, pp. 2248–2251, Mar 1995.

[88] L. Rishøj, P. Steinvurzel, Y. Chen, L. Yan, J. Demas, M. Grogan, T. Ellenbogen, K. Crozier, K. Rottwitt, and S. Ramachandran, "High-energy four-wave mixing, with large-mode-area higher-order modes in optical fibres," in *ECOC 2012*, p. Tu.3.F.2, Optical Society of America, 2012.

[89] K. F. Lee, J. Chen, C. Liang, X. Li, P. L. Voss, and P. Kumar, "Generation of high-purity telecom-band entangled photon pairs in dispersion-shifted fiber," *Opt. Lett.*, vol. 31, pp. 1905–1907, Jun 2006.

[90] H. Takesue and K. Inoue, "1.5-μm band quantum-correlated photon pair generation in dispersion-shifted fiber: suppression of noise photons by cooling fiber," *Opt. Express*, vol. 13, pp. 7832–7839, Oct 2005.

[91] X. Li, J. Chen, P. Voss, J. Sharping, and P. Kumar, "All-fiber photon-pair source for quantum communications: Improved generation of correlated photons," *Opt. Express*, vol. 12, pp. 3737–3744, Aug 2004.

[92] K. Rottwitt, J. Bromage, A. J. Stentz, L. Leng, M. E. Lines, and H. Smith, "Scaling of the raman gain coefficient: Applications to germanosilicate fibers," *J. Lightwave Technol.*, vol. 21, p. 1652, Jul 2003.

[93] G. Ghosh, "Sellmeier coefficients and dispersion of thermo-optic coefficients for some optical glasses," *Appl. Opt.*, vol. 36, pp. 1540–1546, Mar 1997.

[94] P. Steinvurzel, L. Rishøj, Y. Chen, L. Yan, J. Demas, M. Grogan, T. Ellenbogen, K. Crozier, K. Rottwitt, and S. Ramachandran, "High energy parametric amplification at 1 μm with record large mode area optical fibers," in *Photonics West 2012*, SPIE, 2012.

[95] Z. Ding, H. Ren, Y. Zhao, J. S. Nelson, and Z. Chen, "High-resolution optical coherence tomography over a large depth range with an axicon lens," *Opt. Lett.*, vol. 27, pp. 243–245, Feb 2002.

[96] K.-S. Lee and J. P. Rolland, "Bessel beam spectral-domain high-resolution optical coherence tomography with micro-optic axicon providing extended focusing range," *Opt. Lett.*, vol. 33, pp. 1696–1698, Aug 2008.

[97] A. Malinowski, K. T. Vu, K. K. Chen, J. Nilsson, Y. Jeong, S. Alam, D. Lin, and D. J. Richardson, "High power pulsed fiber mopa system incorporating electro-optic modulator based adaptive pulse shaping," *Opt. Express*, vol. 17, pp. 20927–20937, Nov 2009.

[98] K. K. Chen, J. H. V. Price, S. ul Alam, J. R. Hayes, D. Lin, A. Malinowski, and D. J. Richardson, "Polarisation maintaining 100w yb-fiber mopa producing μj pulses tunable in duration from 1 to 21 ps," *Opt. Express*, vol. 18, pp. 14385–14394, Jul 2010.

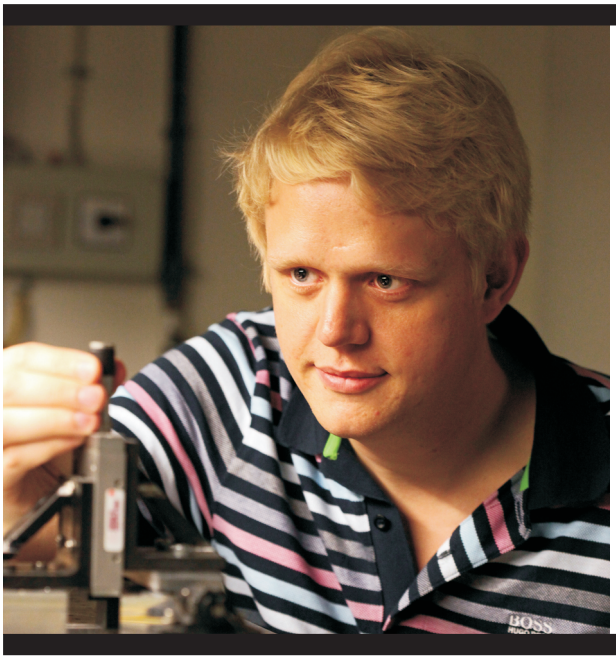

Copyright: Lars Søgaard Rishøj
and DTU Fotonik
All rights reserved
ISBN: 87-92062-93-8

Published by:
DTU Fotonik
Department of Photonics Engineering
Technical University of Denmark
Ørsteds Plads, building 343
DK-2800 Kgs. Lyngby

Lars Søgaard Rishøj was born in Janderup Vestj. Denmark in 1982. In 2003 he started his studies in Applied Physics at the Technical University of Denmark (DTU). In 2009 he received his M.Sc. degree from DTU, which included an external stay at the Royal Melbourne Institute of Technology in 2007. Subsequently, he joined the group "Fiber optics, Devices & Nonlinear Effects" at DTU Fotonik as a Ph.D. student. The aim of his project was to develop a fiber laser using intermodal nonlinearities. The work was primarily carried out at DTU, but included an external stay at Boston University.